**Multiscale Simulations of the Aortic Heart Valve:**
**Applications in Disease and Surgery**

by

Eli J. Weinberg

B.S., Mechanical Engineering, M.I.T. (2002)
M.S., Mechanical Engineering, M.I.T. (2005)

SUBMITTED TO THE DEPARTMENT OF MECHANICAL ENGINEERING IN PARTIAL FULFILLMENT OF THE REQUIREMENTS FOR THE DEGREE OF

DOCTOR OF PHILOSOPHY
AT THE
MASSACHUSETTS INSTITUTE OF TECHNOLOGY

JUNE 2008



Signature of Author _____
Department of Mechanical Engineering
May 22, 2008

Certified by _____
Mohammad Kaazempur Mofrad
Associate Professor of Bioengineering, University of California Berkeley
Thesis Supervisor

Certified by _____
Jeffrey Borenstein
Director of Biomedical Engineering Center, Draper Laboratory
Thesis Supervisor

Certified by _____
Roger Kamm
Professor of Mechanical Engineering and Biological Engineering

Accepted by _____
Lallit Anand
Professor of Mechanical Engineering
Chairman, Departmental Committee on Graduate Studies

**Multiscale Simulations of the Human Aortic Heart Valve: Applications in Disease and Surgery**

by

Eli J. Weinberg

Submitted to the Department of Mechanical Engineering on May 22 2008, in partial fulfillment of the requirements for the degree of Doctor of Philosophy in Mechanical Engineering

## Abstract

This thesis presents mathematical models describing the mechanical behavior of the human aortic heart valve over a range of length and time scales. In the human heart, the valves perform the vital function of controlling the direction of blood flow. Each valve is an intricate mechanical structure, with distinct features and functions at multiple scales. This effort first develops a framework of reference configurations that enables communication between simulations of the different length scales. Three simulations are created within that framework. At the cell scale, the interaction between a single valvular interstitial cell and its surrounding matrix is described. At the tissue scale, a model is created for the valve cusp tissue mechanical behavior, including the multilayered, nonuniform geometry and nonlinear, anisotropic material properties. At the organ scale, a dynamic, three-dimensional model with fluid-structure interaction predicts the motion of the valve, blood, and surrounding tissue. Each simulation is verified against a number of experimental measures. These three simulations together constitute a model for the dynamic, three-dimensional, multiscale mechanical behavior of the healthy human aortic heart valve throughout the cardiac cycle.

The model is employed to perform multiscale investigation into the mechanisms of the disease calcific aortic stenosis in three ways. First, the model of the healthy valve is extended to describe disease progression on the decade time scale. Calcification is introduced at the tissue level and the effects on valve function are monitored at the organ level. Second, the role of mechanical deformations in the disease process is examined by comparing multiscale deformations between the normal valve case and a known disease-prone case. Finally, a combined computational and experimental study investigates the role of fluid shear in calcific disease. Shears computed in the organ-scale simulation are applied to endothelial cells *in vitro*. The cells express disease-related genes in a manner consistent with the region-specific nature of calcific disease, providing evidence for a role of shear in the disease process. The multiscale model presented in this thesis has further utility in investigating function, disease, and therapy of the human aortic valve.

Thesis Supervisor: Mohammad Kaazempur Mofrad
Title: Associate Professor of Bioengineering, University of California Berkeley

Thesis Supervisor: Jeffrey Borenstein
Title: Director of Biomedical Engineering Center, Draper Laboratory

**Acknowledgements**

This research has been supported by a Draper Fellowship.

Composing a doctoral thesis is a difficult task, but coming up with words adequate to express my gratitude to those who have supported me during my journey has posed an even greater challenge. Just as a heart valve is more than a set of equations and figures, my gratitude towards you is more than this text can begin to express.

I first must recognize and thank my advisor who has also been a great friend, Mohammad Kaazempur Mofrad. I have worked with Mohammad nearly as long as I have worked at all, and would not have wanted it any other way. While providing structure and guidance, Mohammad has also given me the freedom and flexibility to craft a thesis topic of my own design. His patience is unmatched, as his ability to motivate and inspire. I know few advisors who would sacrifice their own sleep, rising at 4 a.m. Pacific Time to give a student notes before a morning presentation on the East Coast. I look forward to continued collaboration with Mohammad.

This thesis would not exist if not for a fortuitous meeting with Fred Schoen, where he articulated the two pillars of this thesis, multiscale simulation of the aortic valve and the use of such methods to investigate calcific valve disease. His knowledge of the heart valves is unparalleled, and his supply of creative and innovative ideas on how to approach valve research is endless. In addition to providing the initial brainstorm, Fred has provided invaluable insight and clinical feedback that have shaped the development of this thesis. I hope in the future we can pursue more of his innovative ideas.

I would also like to extend my gratitude to Jeff Borenstein. He started me in the field of bioengineering before many recognized the field existed. Since then, he and Draper Laboratory have supported my graduate work, providing me the opportunity to work on this thesis as well as a number of other remarkable projects.

Since my time was an undergraduate, my best source for informed advice at MIT both on engineering and navigating graduate school has been Roger Kamm. He has patiently spent hours with me on both topics, and I am grateful for his guidance. Roger is the consummate lifelong student, the most astute listener to whom I have ever presented. His probing questions have strengthened my work and his example has taught me how to approach difficult problems

The investigation into the role of shear in calcific aortic stenosis would not have been possible without the experiments performed in Guillermo García-Cardeña's laboratory by Pete Mack. Guillermo welcomed me into his lab without hesitation and provided materials, facilities, and expert insight. Pete graciously took this detour from his own work and performed the experiments with a level of technical skill that I could not possibly match. Pete and Guillermo notably tolerated my personal inability to correctly merge documents. I am also indebted to Louie Villareal for sharing his mouse data.

The computational "heavy lifting" involved in this thesis was performed by commercial mathematical modeling software packages. I am thankful to those who developed ADINA, LS-DYNA, and Altair and particularly to the supports staffs at each company.

I owe my knowledge of the fundamentals that underly this thesis and of many other topics to my many fine professors at MIT. Among them: Rohan Abeyaratne, Lallit Anand, Kamran

Badizadegan, Klaus-Jürgen Bathe, Mary Boyce, Wai Cheng, Jung-Hoon Chun, Ernest Cravalho, Woodie Flowers, David Gossard, Alan Grodzinsky, Doug Hart, Roger Kamm, Gareth McKinley, Fred Schoen, Alex Slocumb, Ain Sonin, David Wallace, and Jacob White.

Like fine wine, a doctoral thesis is nothing if it can't be shared with friends. An alphabetical list of people who have made these years a pleasure is: Charles Antin, Jeff Augustyn, Chris Berejik, Megan Blaskowitz, Marjory Bravard, David Asher Cantor, Kerry Coyne, Ryan Cunningham, Katie Ekstrom, Greg Erman, Lilla Fekete, Tom Fisk, Doug Gauthier, the Goldman family, Tim Hare, Brain Hong, Mohammad Kaazempur Mofrad, Kaitlyn Kenny, Mo Khalil, Kieran Kieckhefer, Jeanyoung Kim, Allan Mabardy, Pete Mack, Alan Maginn, Sarah Neal, Chris Ng, Anish Parikh, Linus Park, Erica Peters, Tom Ptak, Mike Sarno, Greg Townsend, and Liam Walsh. Those I have forgotten will remember and excuse my absent-minded nature.

My parents, Judy and Marc, have tirelessly supported me in all my pursuits, but especially my pursuit of a doctoral degree since we first agreed to this path, when I was in second grade. I dedicate two thirds of this thesis to my parents. The remainder to Stephanie. Her encouragement of my work has been unwavering, but does not compare to her impact on my life away from academia. Final thanks to the rest of my family, which has grown since I started this work, for providing both support and welcome distraction: Hannah, Mike, Connor, and Zanya, Florence and Matt.

22 May, 2008

This thesis was prepared at the Charles Stark Draper Laboratory, Inc., under Independent Research and Development Project Number 21793

Publication of this thesis does not constitute approval by Draper Laboratory of the findings or conclusions contained therein. It is published for the exchange and stimulation of ideas.

_____

(Author's signature)

## Table of Contents

## List of Figures

## List of Tables

# Chapter 1. Introduction to the Mathematical Modeling of Human Heart Valves

## Multiscale Mechanics of Human Heart Valves

The human heart is a pump system consisting of four chambers and four valves. As the chambers contract to eject blood, the valves open and close in sequence to control the direction of flow. The locations of these valves and flow paths through the heart are illustrated in Figure 1.1.

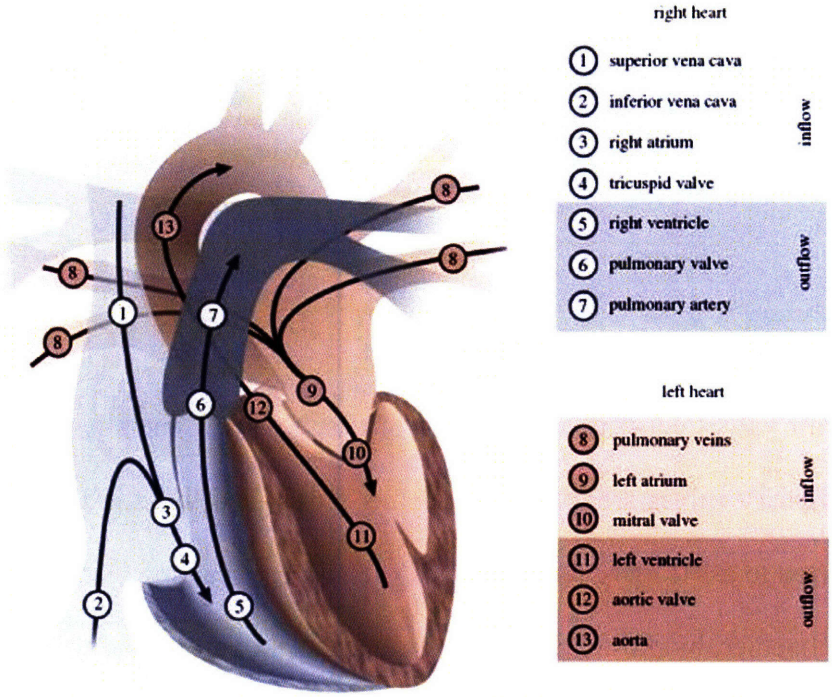


**Figure 1.1.** Valves of the human heart and flow directions[198].

Mechanical behavior of the valves can be examined at the molecular, cellular, tissue, and whole organ length scales (Figure 1.2). Here, we briefly describe the valve mechanical behavior at each scale.

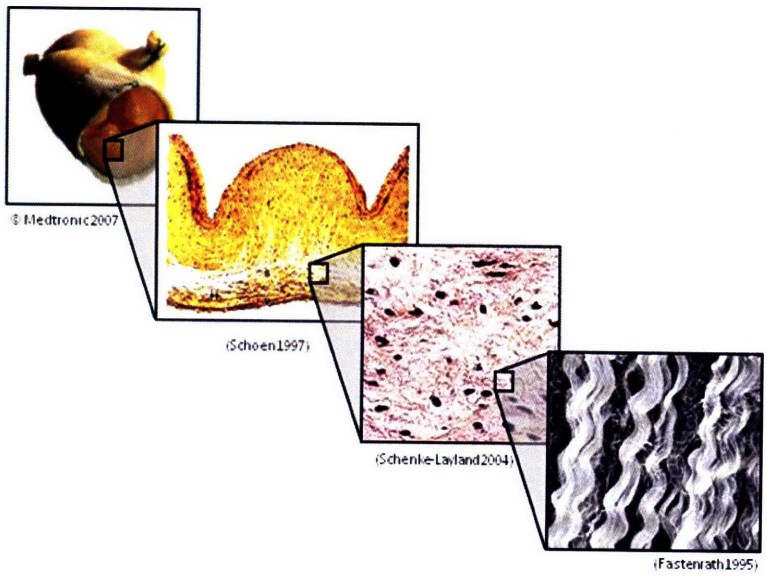


**Figure 1.2.** Representation of the multiscale nature of heart valve mechanics: organ, tissue, cell, and molecule scale features

*Organ Scale*

Each of the heart valves consists of a number of tissue flaps. Generally the tissue flaps of the aortic and pulmonary valves are referred to as the 'cusps' and those in the mitral and tricuspid valves are referred to as 'leaflets'. In this thesis, we will use the term leaflet when discussing the natural valves together, bioprosthetic valves, or mechanical valves, and use the term cusps only when specifically addressing the natural aortic or pulmonary valve. The aortic, pulmonary, and tricuspid valve each normally have three leaflets and the mitral valve has two. Leaflets themselves are passive, opening and closing when forced by the blood. Healthy heart valves

open widely, providing an unobstructed flow path, and seal closed. Photos of an aortic valve (AV) in its open and closed position are shown in Figure 1.3. The valves move quickly between their open and closed positions and require little force to do so.

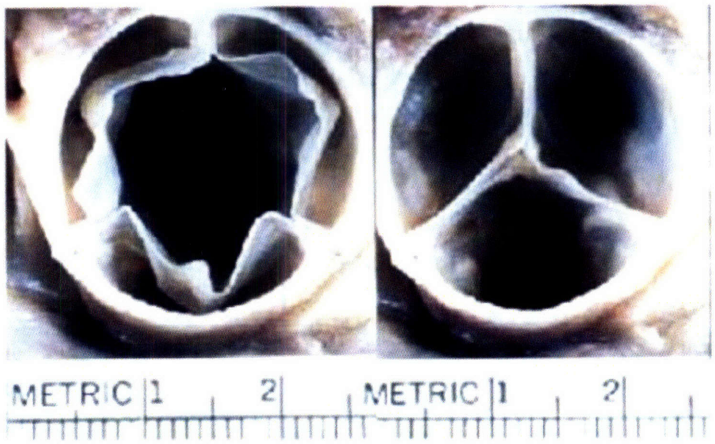


**Figure 1.3.** Valve open and closed[121]

As the heart grows over the human lifetime, the valves must also grow proportionally to adapt to the increased pressure and flow configurations. Moreover, the valves change shape as the heart moves and contracts during the cardiac cycle. Additionally, the mitral and tricuspid valves include chordae tendinae, chord-like structures that connect the cusps to muscles on the ventricle wall and that help the valves maintain their closed shape and open rapidly.

*Tissue Scale*

Valve leaflet tissues have a number of unique features as illustrated in Figure 1.4, a micrograph cross-section of AV leaflet. These thin tissues (0.2-2.0mm)[80] are composed of three layers. The

ventricularis is below the inflow surface. This is the thinnest layer, and consists mostly of collagen with some elastin. Below the outflow surface, the thicker fibrosa is composed of aligned collagen[165]. The fibrosa is crimped when the tissue is unstressed, and these crimps flatten when the tissue is tensed due to pressurization of the valve[158]. Between the two fibrous layers exists the gel-like spongiosa[165].

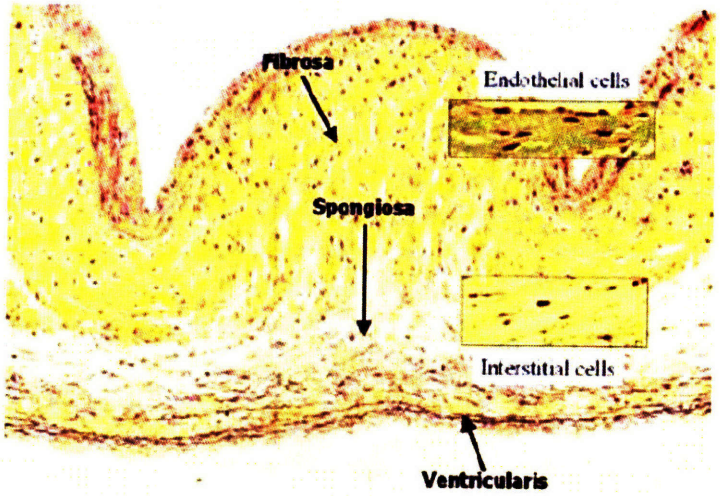


**Figure 1.4.** Micrograph cross-section of AV leaflet showing tissue layers and cells[121]

*Cell Scale*

Two types of cells are found within the valve leaflets, both shown in Figure 1.4. The valvular interstitial cells (ICs) are distributed throughout the extracellular matrix (ECM), and the valvular endothelial cells (ECs) coat all of the blood-facing surfaces. ICs are responsible for maintaining the extracellular matrix and modulating disease pathology[117]. In the valve, ICs display a number of different phenotypes at different locations, and share some characteristics with fibroblasts and some with skeletal, cardiac, and smooth muscle cells[37, 122, 152, 177]. ICs are known to remodel over the human lifetime[143], respond to physical deformations[83], and engage in signaling with other ICs

and the ECM[37]. Similarly, the ECs have spatially varying phenotypes[167], respond to mechanical stimuli[189], regulate valve pathologies[26], and engage in signaling[26].

*Molecular Scale*

Heart valve leaflets are composed of fibrous matrices, in which a sponge-like matrix of elastin surrounds bundles of collagen fiber[177]. The fibers are aligned in the plane of the leaflet and organized into three layers, the fibrosa, spongiosa, and ventricularis. The collagen and elastin exist in a hydrated gel-like ground substance, composed of proteoglycans and glycosaminoglycans[178]. Collagen and elastin are kinked fibers that can straighten under small loads, allowing large extension of the tissue at low stresses. Micrographs of the matrix structure are shown in Figure 1.5.

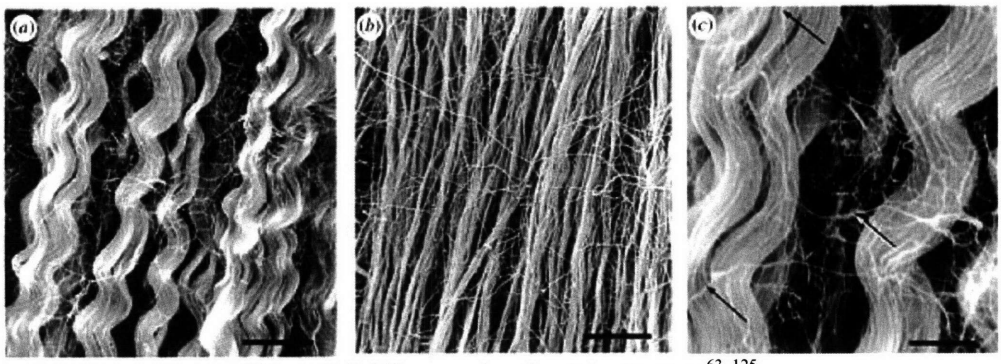


**Figure 1.5.** Micrographs of matrix structure[63, 125]

*Multiscale*

In the heart valves, distinct mechanical behaviors can be observed at the molecule, cell, tissue, and organ length scales. Additionally, there is mechanical communication between the scales, where behavior at one scale impacts behavior at another scale. This communication can proceed either from a smaller to a larger scale or the opposite. The main mechanical communication from the smaller scale up determines the overall function of the valve: the extensibilities and geometric organization of the fibrous molecules determines the tissue stiffness and anisotropy[13, 14] which, along with the tissue-scale geometry, determines the organ-scale motion of the cusps[193]. There is active communication from the cell scale to the tissue scale, where contraction of the ICs significantly affects tissue stiffness[123]. Mechanical communication from the larger scales downwards affects active biochemical processes. In the fluid, organ-scale fluid motion applies shears to the ECs. In the solid, organ-scale motion deforms the tissue, which in turn deforms the ICs. Mechanical signals control gene expression in normal and diseased states of the ECs[26, 189] and ICs[117, 152, 177].

**Heart Valve Dysfunction**

Healthy heart valves operate efficiently, easily moving between an unobstructed open configuration and a fully sealed closed configuration. A variety of disorders can prevent a valve from opening fully (stenosis), keep the valve from sealing closed (regurgitation), or cause other dysfunction. Here, we briefly review the pathologies of common heart valve disorders and current courses of treatment.

*Disorders*

Aortic stenosis (AS) is the most common valve disease, occurring in 2% to 4% of adults over 65 years in age[70]. In calcific aortic stenosis, calcified nodes, shown in Figure 1.6, develop on the AV cusps. These nodes make the cusps stiff, preventing the valve from opening fully and thus obstructing flow[135, 179]. AS may be caused either by age-related wear on the valve or by rheumatic disease[115]. Stenosis of the tricuspid or pulmonary valves is known but rare. Mitral stenosis (MS) is more common and generally caused by rheumatic fever[115].

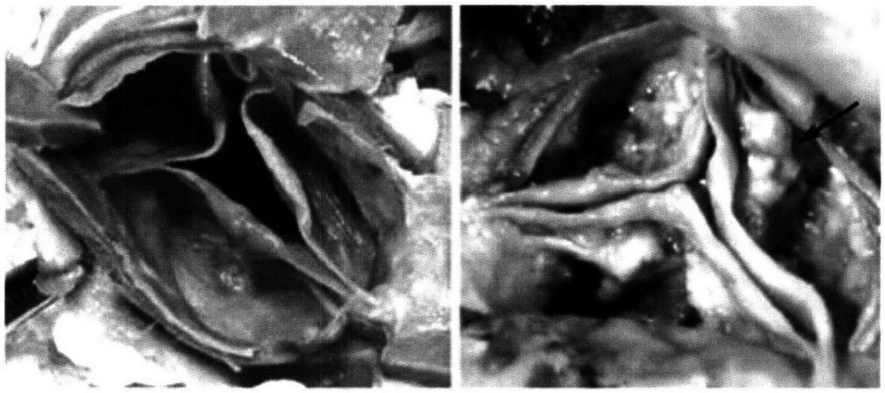

**Figure 1.6.** Photographs of (left) healthy AV and (right) severely calcified valve[70]

Regurgitation is observed most commonly in the mitral valve. Mitral regurgitation (MR) may be caused by a variety of underlying conditions. Valve degeneration, papillary muscle dysfunction, infective endocarditis, rheumatic disease, and enlargement of the left ventricle can all impair mitral valve closure[115]. Aortic regurgitation (AR) can also occur, with similar causes of either tissue disease or orifice enlargement[135]. Tricuspid and pulmonary valve regurgitation are generally functional rather than structural, meaning they develop in response to pressure overload and not due to a mechanical defect of the valve itself[115].

A few valve diseases exist that are neither stenotic nor regurgitant. Mitral valve prolapse (MVP) refers to a condition where the mitral valve bulges out significantly under pressure. In bicuspid aortic valve (BAV), occurring congenitally in 1-2% of the population[134, 179], the AV has two cusps instead of three. MVP[115], BAV[181], and other valve malformations are often precursors to regurgitation and stenosis.

*Treatments*

Each valve disorder has a different course of treatment. These therapies fall into three main categories. First, pharmaceutical drugs may be used to prevent or limit the progression of disease. No drugs exist to treat most valve diseases, but statins show promise in inhibiting calcific aortic stenosis[129, 137, 150]. A second approach to treating valve disease is to surgically repair a mechanical defect. A common example is resection of the flailing mitral valve posterior leaflet, illustrated in Figure 1.7. Surgery is possible in specific cases of stenosis and regurgitation of any of the valves[195, 196], with new methods continuously being developed[28, 44].

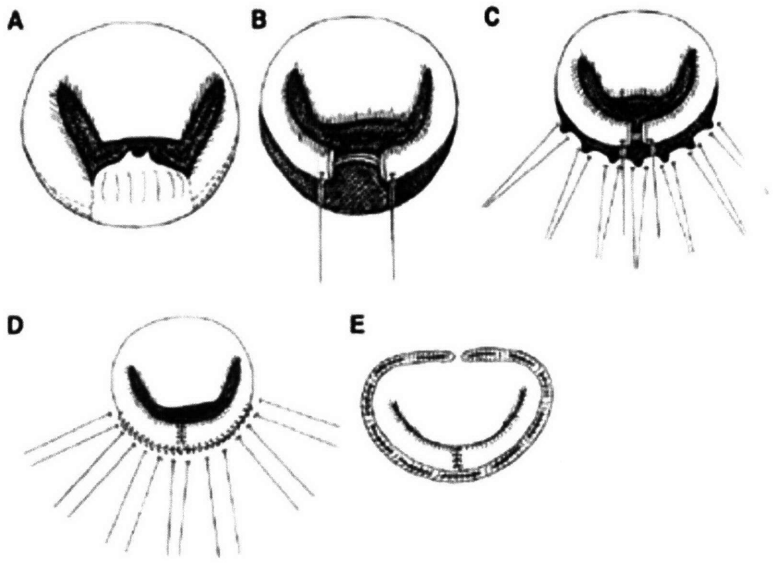


**Figure 1.7.** Illustration of quadrangular resection to correct prolapsing mitral leaflet. Excess tissue is removed, the remaining leaflet is sutured, and a ring is attached to the annulus to provide structural support[196].

In the vast majority of cases, the only current approach to correcting a failing valve is to replace the entire valve and sometimes also the surrounding tissue. Development of valve replacement methods has proceeded rapidly over the past four decades, and represents a great achievement in the field of biomedical engineering. As illustrated in Figure 1.8, valve replacement enormously increases patient survival.

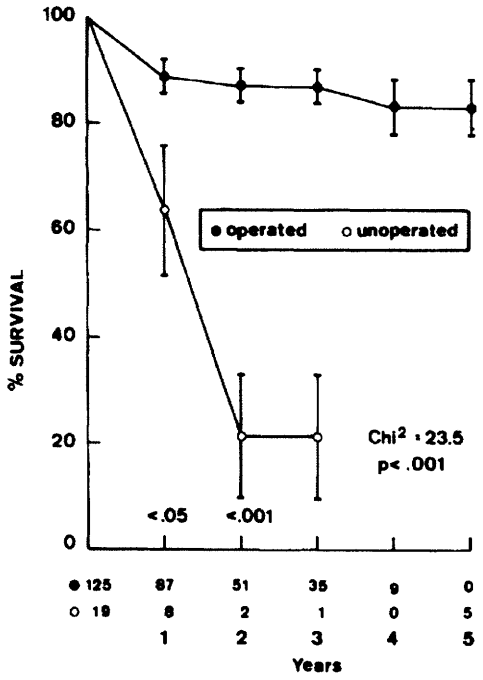


**Figure 1.8.** Survival curves for operated and unoperated patients with aortic stenosis[166]

A prototype of one of the first mechanical valves is shown in Figure 1.9.A., a ball-in-cage type. Currently, mechanical valves and bioprosthetic valves are both used for replacement of all valves. Modern mechanical valves are based on a tilting disc (Figure 1.9.B.), and modern bioprosthetic valves are constructed from glutaraldehyde-fixed porcine tissue. Current research is directed towards reducing thrombogenicity of mechanical valves[53], increasing durability of bioprosthetic valves[157], and development of tissue-engineered solutions[121]. Much research in the simulation of heart valve mechanics has focused on simulating the mechanical and bioprosthetic valves, perhaps more so than the natural valves.

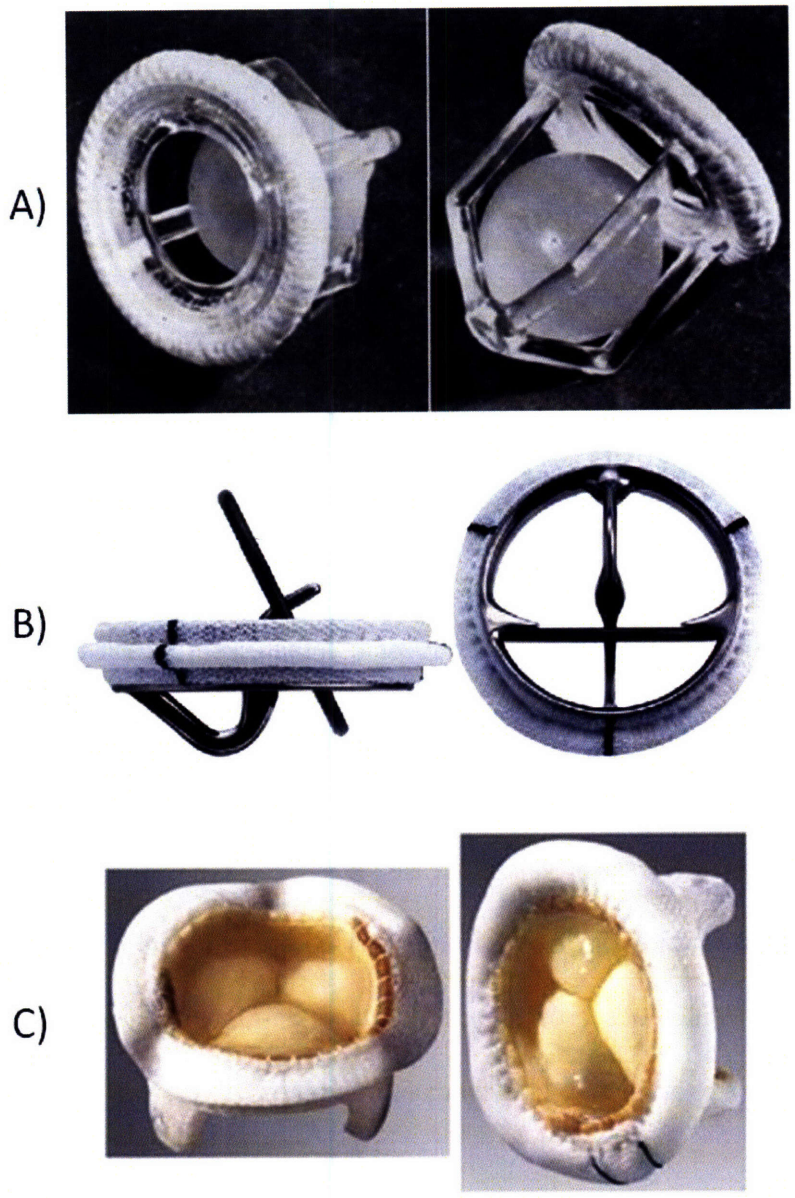


**Figure 1.9.** Various prosthetic heart valves. A) Prototype of the Starr Edwards ball-in-cage valve[169] B) Modern tilting disc prosthesis ©Medtronic 2008 C) Modern bioprosthetic valve ©Medtronic 2008

## Enabling Experimental Tools

Experimental investigation of mechanics at each length scale relies on methods from a disparate range of disciplines. We highlight some of the common and emerging technologies that have been applied specifically to heart valves.

*Organ Scale*

In the clinical setting, the health of a patient's valve may be assessed in a number of ways. The classic method of listening to heart sounds can detect and, along with other physical examination, diagnose abnormalities[21, 115]. Cardiac catheterization can be used to examine the valve for calcification or other defects[21]. Valve disease is most commonly evaluated by chest echocardiograph[87, 136], which allows measurements of fluid motion and valve geometry that can be compared to various indices for valve disease[4, 5, 17, 75, 183]. An example of typical images used for evaluation of aortic stenosis is shown in Figure 1.10. Researchers have recently demonstrated MRI[97] and CT[2, 67, 68] methods able to resolve valve motion, holding promise that modern imaging methods may be applied to clinical examination of valves.

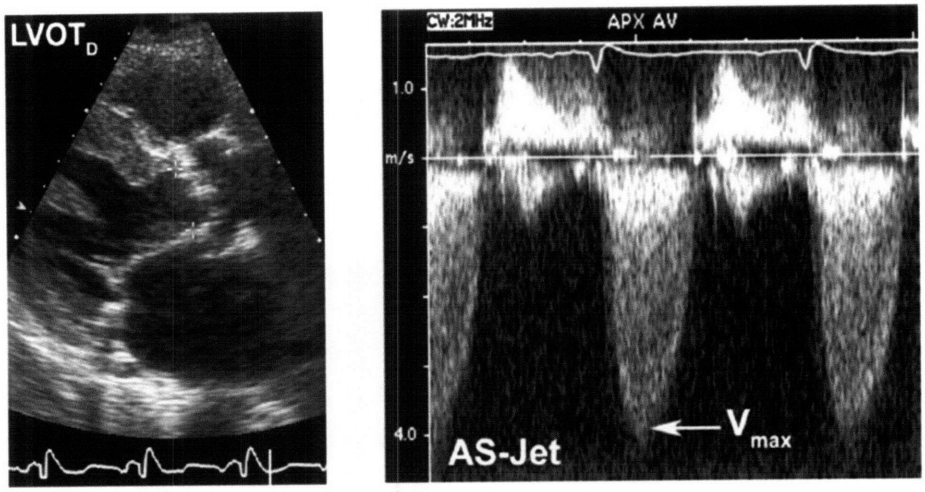


**Figure 1.10.** Standard evalulation of aortic stenosis severity by chest imaging: A) visual measurement of valve orifice diameter and B) pulsed Doppler measurement of fluid velocity[136]

A number of laboratory methods available to examine organ-scale valve motion cannot be used on patients. A pulse chamber can be used to subject physiological flows to valves, where valve deformation can be monitored by optical methods[66, 73, 88, 96, 173] and fluid motion can be measured by particle velocimetry[31]. Valve motion has been measured in large-animal models by tracking sonocrystals attached to the leaflets[179] and fluid velocity profiles have been measured in the animal models by hot-wire anemometry[62].

*Tissue Scale*

Tissue mechanical properties have historically been measured by Instron-type uniaxial tester[40, 126, 151, 163, 180, 185, 186]. The Sacks group has pioneered use of optically-measured methods that, in concert with development of theoretical tools, has enabled rigorous description of multilayer, anisotropic, nonlinear, tissue properties in both biaxial and bending deformations[159, 160].

Standard histology methods give two-dimensional pictures of tissue microstructure, like that in Figure 1.4. New imaging methods extend this capability to three dimensions. Figure 1.11 shows the three-dimensional geometry of an AV cusp rendered by high-frequency ultrasound[109].

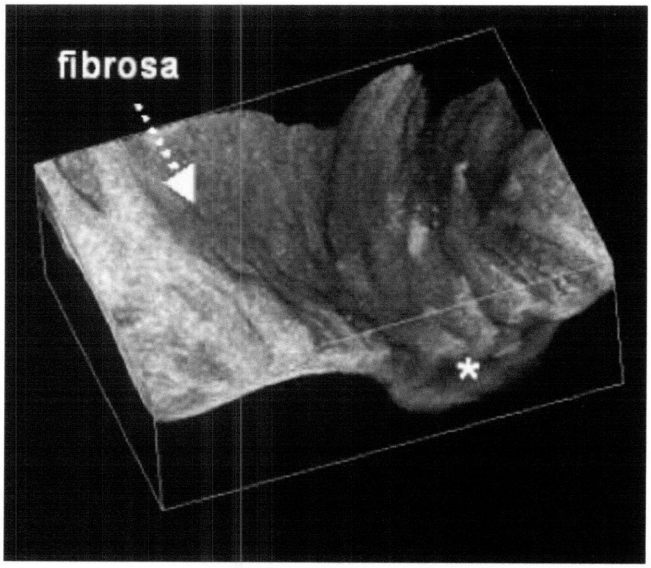


**Figure 1.11.** Image of three-dimensional AV cusp tissue structure, rendered by high-frequency ultrasound[109].

*Cell Scale*

Methods for measuring the mechanical properties of cells have been developed[116] and recently applied to ICs[123]. Figure 1.12 shows an IC being probed by micropipette aspiration. Pressure is applied to the cell via the pipette, and cell mechanical properties are deduced from the observed deformations. Cell deformations in diastole have also been quantified by pressurizing and fixing a valve, then optically observing the cell nuclei aspect ratios[94].

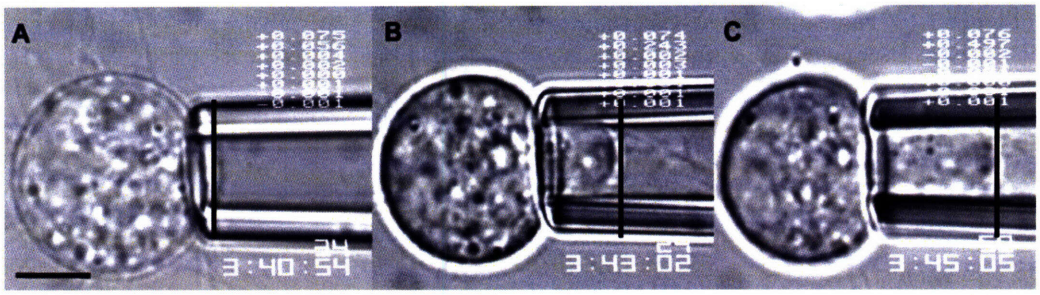


**Figure 1.12.** Micropipette aspiration of a tricuspid valve IC. Pipette pressure increases from left to right. Scale bar is 5 microns[123].

*Molecule Scale*

Like the larger scales, the tools molecular mechanics drawn from other fields have been applied or show promise for application to heart valves. Methods for single-molecule mechanics, such as laser traps demonstrated on collagen[118] are directly applicable to heart valve matrix components. Imaging capabilities have reached the molecular level and have recently been applied to examining heart valve leaflet structure. Figure 1.13 shows an image produced by femtosecond laser pulse of the three-dimensional network of collagenous and elastic fibers in the heart valve leaflet[164].

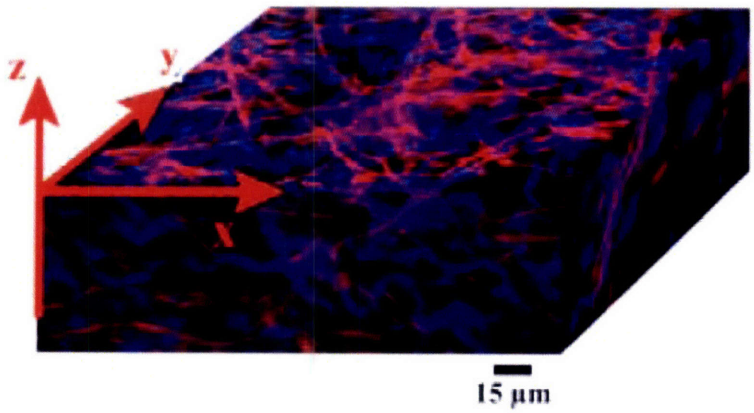

**Figure 1.13.** Three-dimensional reconstruction of ovine aortic heart valve leaflet by femtosecond laser pules. Collagenous fibers are shown in blue and elastic fibers in red[164].

*Multi-Scale*

While many tools are available to investigate the mechanical behavior at each scale, few experimental approaches have been developed that span multiple scales. Huang *et al.* measured the cell-scale deformations in response to pressures applied at the organ scale[94], Merryman *et al* measured the tissue mechanical behavior in response to cellular contraction[122], and in this thesis we will measure the cellular response to organ-scale shear[189].

## Enabling Theoretical Tools

The field of mathematical modeling of heart valve mechanics has grown from nonexistent to a broad discipline in three decades. This expansion is due both to development of mathematical approach and computational tools to describe relevant mechanical behavior and to the increased availability of computational power necessary to simulate complex biomechanical dynamics. Here, we discuss some of the advances in general numerical biomechanics that will be applied to heart valves in the following sections.

*Organ Scale*

Using finite-element analysis (FEA) to calculate the motion of heart valves is a challenging mathematical problem. Leaflets undergo large strains (up to 40%) as well as very large displacements and rotations. Simulation of these deformations has been enabled by the development of the nonlinear Updated Lagrange and Total Lagrange approaches to large-deformation solid mechanics[7]. A further difficulty is modeling the interaction between the leaflets and blood, both of which move dynamically throughout the cardiac cycle. Two primary methods have been developed and implemented for such large-displacement fluid-structure interactions (FSI). In the Arbitrary Lagrange-Eulerian (ALE) method, the solid and fluid meshes are connected, and the fluid mesh is adaptively modified around the moving solid[7]. In the operator-split method, a moving solid mesh can pass through a stationary mesh[84]. Increased computational power has enabled more complete models of heart valve organ-scale behavior. Where running a solid-only simulation with linear elastic models once required nearly a day on a supercomputer[76], only five years later a full FSI with nonlinear materials can be performed in a few hours on a personal computer[193].

*Tissue Scale*

The two main advancements in mechanical modeling at the tissue scale are the development of constitutive models for biological tissues and the tools to implement those models in the FEA setting. Constitutive modeling of tissue behavior requires the theoretical framework provided by continuum mechanics[72, 89]. The initial insight upon which the rest of the field is based was Fung's demonstration that biological tissues behave in a hyperelastic manner. That is, these

matrices of fiber and water have nonlinear, usually exponential loading curves, but follow the same curve in loading and unloading[71, 72]. Further work has shown that heart valve tissue has pseudoelastic (different loading and unloading curves)[119] and viscoelastic behavior[13, 82] in relevant regimes, but modeling the valve tissues as elastic is a currently accepted practice. With the assumption of elasticity and the additional assumption that the tissue can be represented as continuous, the material behavior can be described by an elastic strain energy density function, $W$. This function tells the strain energy in terms of the tissue deformation. Once $W$ is defined, the stresses in the tissue can be calculated by taking the derivative with respect to strain,

$$\sigma = \frac{\partial W}{\partial \varepsilon}, \qquad \text{(Eq. 1.1)}$$

where $\sigma$ is the Cauchy (true) stress tensor and $\varepsilon$ is the Green strain tensor. Researchers are now able to construct strain energy functions that can describe the complex behaviors of biological tissues: anisotropy, nonlinearity, and nonhomogeneity, all with large deformations. For implementation in FEA software, the function must additionally be numerically well-behaved. Some reasonably constructed models for biological tissue have been shown to not possess necessary behavior, namely convexity[91].

Once an appropriate W has been formulated, it is another matter to implement the model in FEA software. A great deal of effort has gone into the creation of rigorous methods for modeling three-dimensional materials in FE. Sussman created the mixed (u/p) formulation commonly used to model arbitrary incompressible materials with three-dimensional finite elements[175], and others have implemented anisotropic and biological material models[3, 153]. Valve leaflets, being quite thin, are commonly modeled with shell rather than three-dimensional elements[90, 105]. For these

elements a separate and equally significant effort has gone towards creating a theoretical framework for using shells to model large deformations in general[6, 12, 33, 54, 176, 192] and tools for handling complex materials models[105].

*Cell Scale*

Two main types of models have been proposed for cell mechanical behavior. Most follow the continuum assumption and describe the cell as some combination of fluid and solid enveloped by the cell membrane [116, 127]. Other models take a structural approach, treating the cytoskeleton as the main structural component [116, 127].

*Molecule Scale*

While mechanics at the cell, tissue, and organ scale can usually be described by continuum mechanics, the continuum assumption does not hold at the molecular level. Molecular dynamics (MD) simulations must be used to analyze molecule-scale interactions. Like in FE analysis, MD has progressed rapidly in recent years. We are not aware of MD having been applied to heart valves. See Sotomayor for a review of the field [168].

*Multi-Scale*

Once simulations are created across a distinct set of length scales, new methods may need to be created to link the scales. Researchers have performed such links in a few cases, such as linking the tissue and organ scales in a model of the arterial wall [171] and linking collagen matrix tissue-scale behavior to molecular mechanics [32, 98].

## Heart Valve Numerical Models

Enabled by the experimental and theoretical methods described above, a number of groups are actively developing and using mathematical models of heart valve mechanics. For each length scale, we give a brief history of heart valve models and describe the current state of the art.

*Organ Scale*

At the organ scale, the motion of natural valves and bioprosthetic valves is very similar. Accordingly, the simulation methods for the two are similar, and we discuss the two together. Mechanical valve motion is quite different from tissue valves. Simulation of mechanical valves is discussed here both because the impressive work in the field bears mention, and because simulation methods developed for mechanical valves may have application for tissue valves.

Over the past three decades, simulations of heart valve motion have drawn from the existing state-of-the art technologies and pushed for further advances. The simplest valve simulation is the static case of a valve closed against pressure. This situation can be examined without a fluid phase, representing the fluid simply as a pressure load against the valve leaflets. The earliest simulations were of this case, generally treating the solid as isotropic and linear[29, 30, 38, 85, 86]. Figure 1.14 shows the geometry of a leaflet in one such simulation[85]. Analysis of the static, closed-valve case has continued[10], and present models include rigorous accompanying work in material modeling and experimental verification[172].

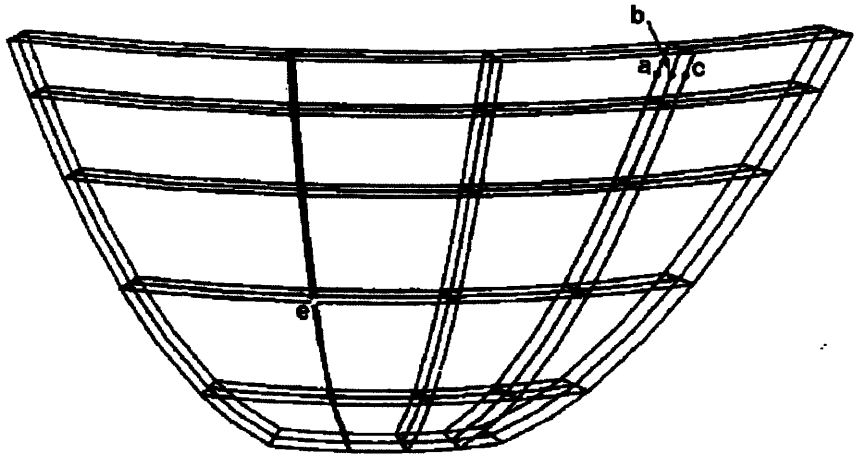


**Figure 1.14.** Mesh geometry for early static simulation of leaflet[85]

The next step in complexity of organ-scale models is to move from the static to the dynamic case. Again, the fluid can be represented simply as a pressure load applied on the surfaces of the solid, but now the leaflets move through large deformations. The first dynamic solid-phase models were developed a few years after the first static models, and thus tend to include more advanced descriptions of both geometry and material properties. Grande-Allen *et al* simulated the AV including realistic asymmetric geometry and the aortic root[79-81]. Geometry of this

simulation is shown in Figure 1.15.A. Other models added anisotropic[106] and nonlinear[16, 92] material descriptions. As with the static case, the dynamic solid-only case is presently being used with advanced material models and relevant experimental work [100, 101]. Results of this model are displayed in Figure 1.15.B.

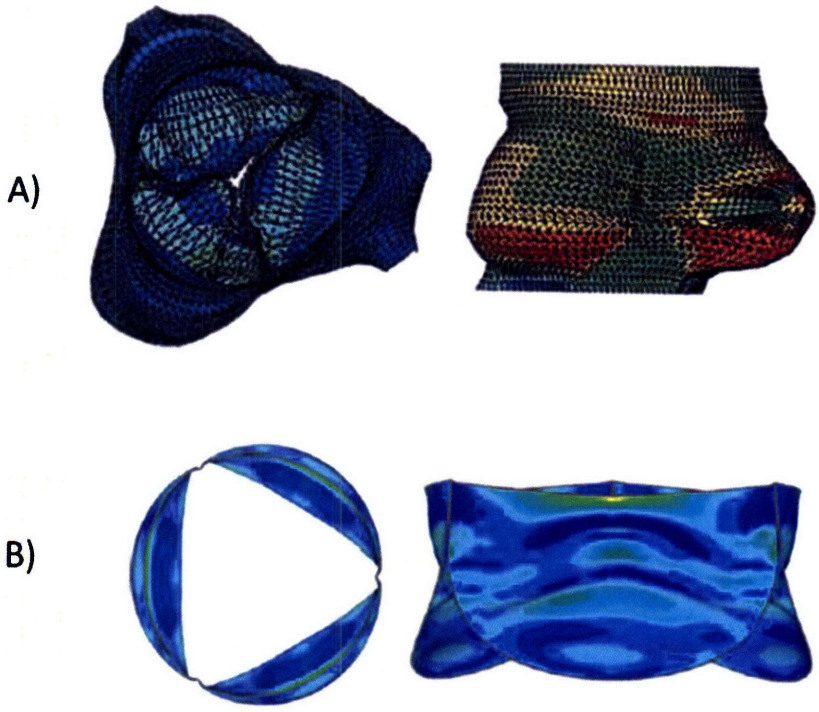


**Figure 1.15.** Results of AV dynamic, solid-only simulation with a) realistic geometry[79] and b) realistic material model[100].

An entirely new level of complexity and computational expense is added by incorporating the fluid and performing FSI analysis. These models were created after the solid-only models, and thus usually include more advanced material models in addition to the fluid. Possessing realistic geometries, well-defined fibrous material models, and the interaction of fluid and solid, these models represent the current state of the art. The de Hart group impressively has coded fictitious domain software to perform the FSI and included a fibrous material model[46-48] to model a

bioprosthetic valve. One of the results of their simulations is shown in Figure 1.16.A. Other researchers have utilized the FSI capabilities of LS-DYNA (LSTC, Livermore CA) to simulate various valves. Nicosia *et al* modeled the AV using an anisotropic elastic material model[131], followed by the work presented in this thesis of modeling the AV with a discrete fiber model[193] and Einstein modeling the mitral valve with a splayed fiber model[56-58, 107]. The last two models notably are verified against various experimental measures, and Einstein's model is able to predict heart sounds[56]. Figure 1.16.B. shows a graphic of the mitral model. The model also includes the chordae tendinae, not shown.

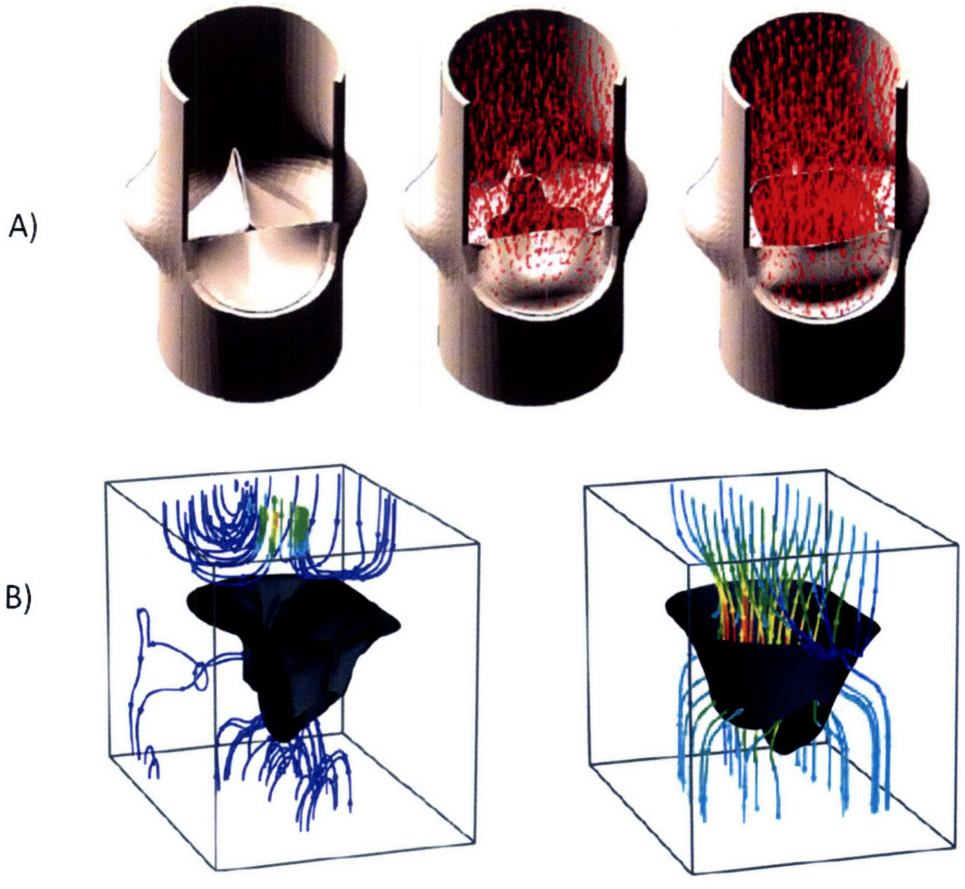


**Figure 1.16.** Results of organ-scale simulations with realistic geometries, fibrous material models, and fluid-structure interaction. A) Bioprosthetic valve simulation[47], B) mitral valve simulation[56]

Progress in simulation of mechanical heart valves has perhaps outpaced that of tissue valves. The most advanced models of mechanical heart valves include FSI and include sophisticated descriptions of blood flow. All of the FSI simulations of natural valves treat the blood as a simple Newtonian fluid. A number of models for mechanical valves have been demonstrated that incorporate realistic non-Newtonian fluid models for blood and predict thrombogenicity of the valve[18, 19, 35, 36, 61, 199]. Some results of one of these simulations[53] are shown in Figure 1.17. We expect that future tissue valve models will incorporate these advancements in blood flow modeling.

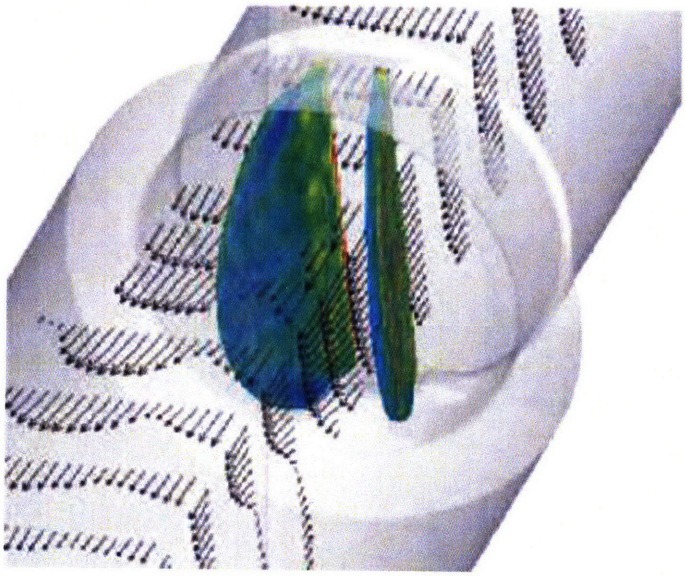

**Figure 1.17.** FSI simulation of a mechanical heart valve[53]

*Tissue Scale*

Modeling of valve tissue-scale mechanics has been recently reviewed[160, 188], and the field continues to progress rapidly. Valve tissue, even compared to other biological tissues, is particularly nonlinear, nonhomogeneous, and anisotropic. Loading curves for a sample of mitral

leaflet tissue, shown in Figure 1.18, display the anisotropy and exponential behavior typical of heart valve leaflets.

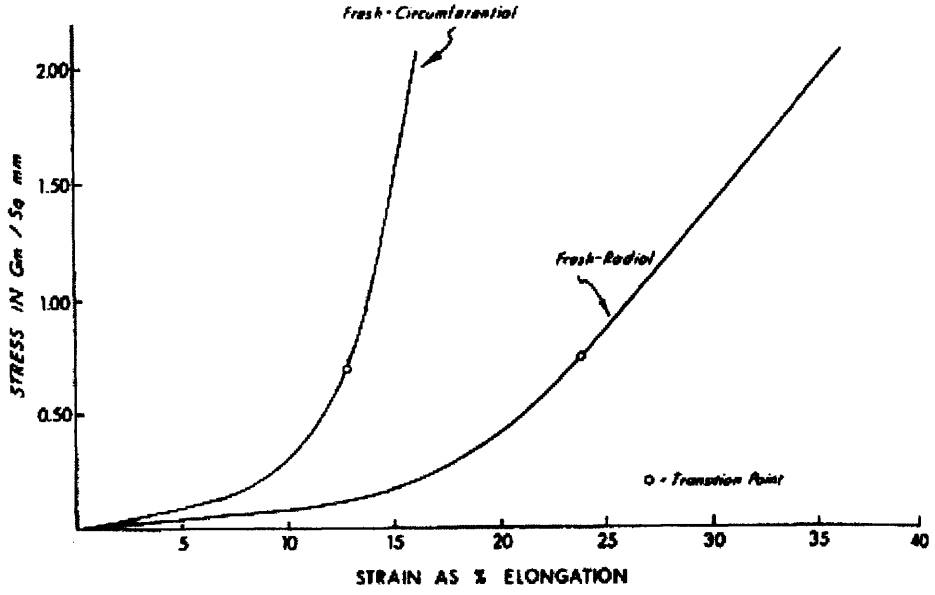


**Figure 1.18.** Loading curves for human mitral leaflet tissue[40], demonstrating anisotropic and exponential behavior

A large number of approaches exist for constructing constitutive material models, and a number have been used to describe valve leaflet tissue. One approach for defining $W$ is to construct it as the sum of simple terms expected to give the correct behavior, and then fit constants to experimental data. Li *et al* extended linear transverse isotropy to nonlinear to model AV tissue[114]. May-Newman and Yin constructed a Fung-like exponential strain energy function from the three usual strain invariants and two directional pseudo-invariants[91, 95] to model mitral valve leaflet behavior[119]. An approach used widely in modeling other hyperelastic materials and biological tissues[15] but not, to our knowledge, in heart valve mechanics, is the unit-cell approach. Unit-cell models base their strain-energy functions on the theoretical behavior of a unit cell of

entropic chains. The most advanced strain-energy functions for valve mechanics include fiber splay as well as fiber direction. Such models have been constructed and fit to experimental data for aortic[13, 14] and mitral[56] valves.

Current research in continuum models for leaflet mechanics aims to create a multi-layered model of the tissue with continuum models for each layer. As depicted in Figure 1.19, Stella *et al* have surgically dissected the AV leaflet to perform biaxial testing of each layer, and based on that data they have created a model having multiple layers with different splayed-fiber material descriptions[170].

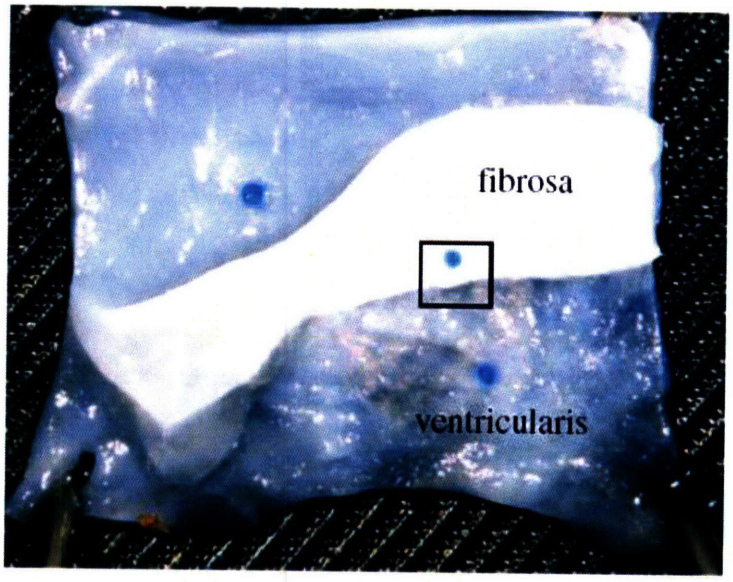


**Figure 1.19.** Surgical dissection of AV cusp layers[160]

Also drawing from that data, in this thesis we will model each layer with a continuum model and add the undulated geometry and transversely isotropic behavior for each layer[193]. The geometry of this tissue model is shown in Figure 1.20.

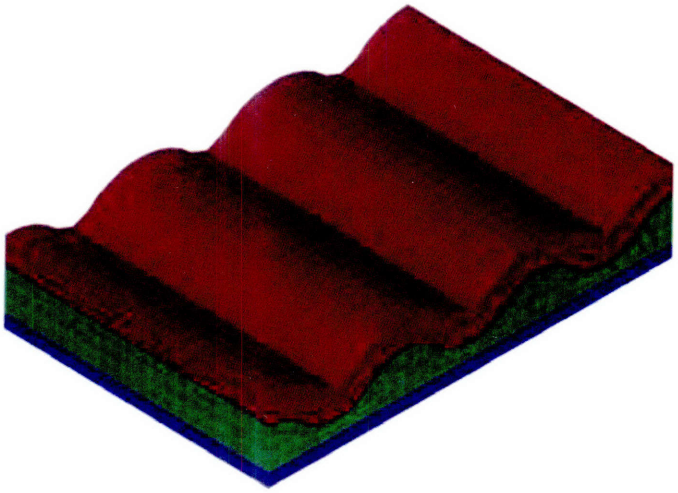

**Figure 1.20.** Geometry of multilayered, undulated tissue model[193]

A number of examples have been published where analytical models for valve tissue are implemented for use in FEA simulations. Since the valve leaflets are fairly thin, most researchers have used shell models. Bioprosthetic valves have been modeled with shells having aligned-fibers models[16, 27]. Shell models have also been implemented for mitral valve leaflet tissue[142], including the effect of changes in thickness[192]. Currently, the most widely used models incorporate a splayed fiber model into a shell. This approach has been used successfully in simulating bioprosthetic valves[172, 173] and mitral valves in healthy and diseased states[56-58].

While most existing constitutive models for AV tissue mechanics are continuum-based, in some cases other approaches may be useful. In this thesis, we will create a discrete fiber tissue model, illustrated in Figure 1.21, that is particularly computationally efficient when used in explicit finite element codes such as LS-DYNA[193].

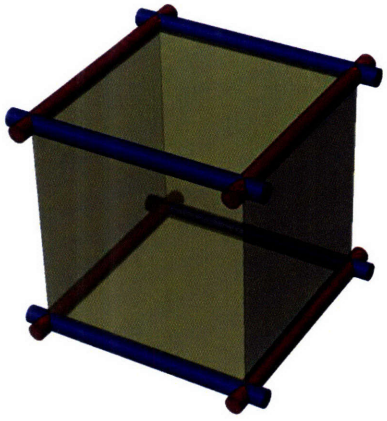

**Figure 1.21.** Single solid element of discrete-fiber model for AV tissue[193]

*Cell Scale*

While many groups have reported simulation of organ and tissue scale heart valve mechanics over the past three decades, simulation at the cell scale has only been reported recently by two groups. Huang *et al* modeled the deformation of ICs in pressurized valves and compared results

to experiment[93, 94]. Their simulation geometry is illustrated in

A)

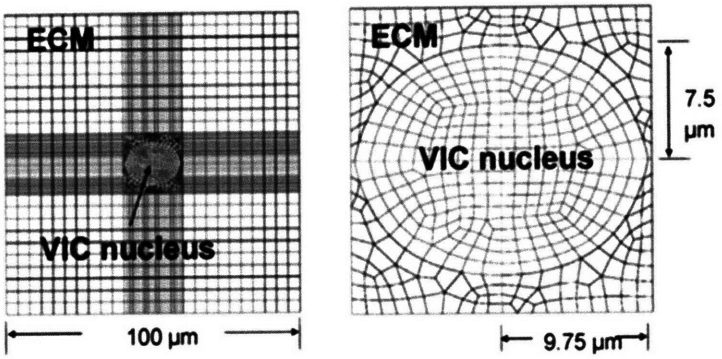


B)

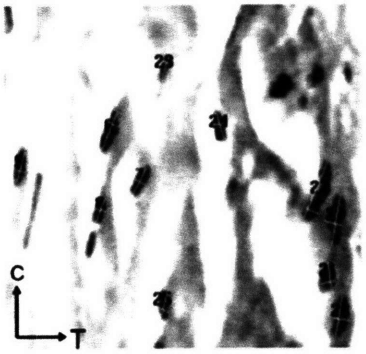


Figure **1.22**.A. In this thesis, we will extend to that work to the three-dimensional, dynamic deformations[193] and to disease[190].

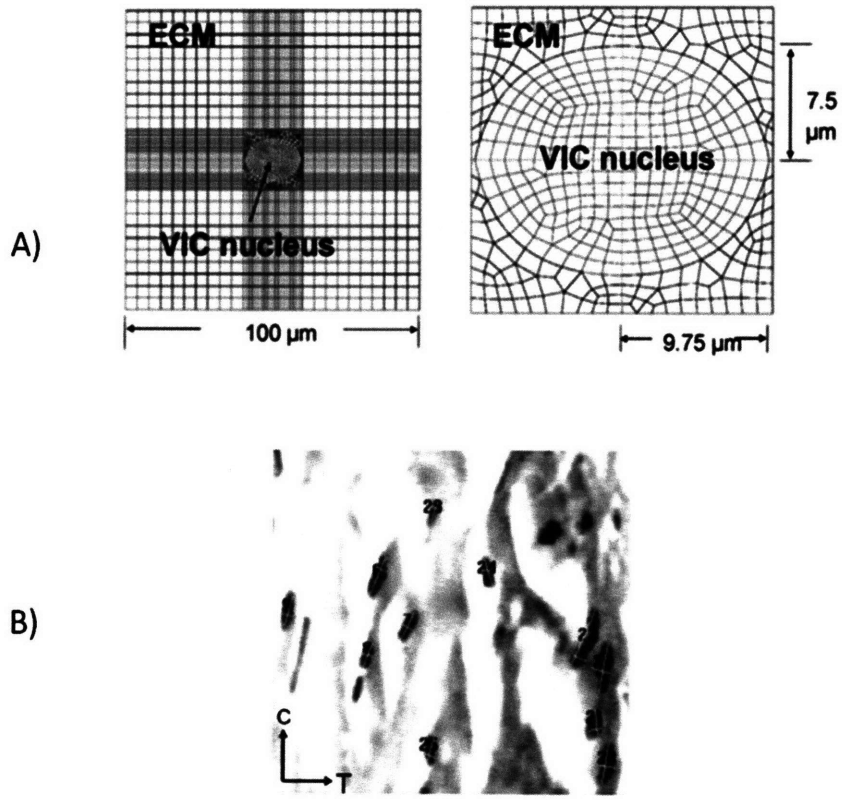


**Figure 1.22.** Theoretical and experimental investigation of IC deformation in valves under pressure by Huang *et al.* A) Simulation geometry B) Image processing measuring IC aspect ratios[94]

*Molecule Scale*

Molecular-level simulation has not yet been applied specifically to heart valve molecular mechanics. Some efforts do exist, however, that are directly applicable. In particular, current research is directed to simulating various aspects of the behavior of collagen fiber on the molecule scale [139, 144-146, 162].

*Multi-Scale*

Researchers have presently taken up the interesting task of linking simulations between various length scales. Different groups have chosen various multiscale effects. Carmody *et al.* have embedded the valve organ-scale motion to the larger organ-scale motion of the left ventricle[28]. We have previously mentioned the cell-scale simulation by Huang *et al.* They have used analytical calculations to link the cell-scale model to pressures applied at the organ-scale, and have notably compared to experimental data with good agreement[93, 94]. An image from their measurement of IC aspect ratios under pressures is shown in

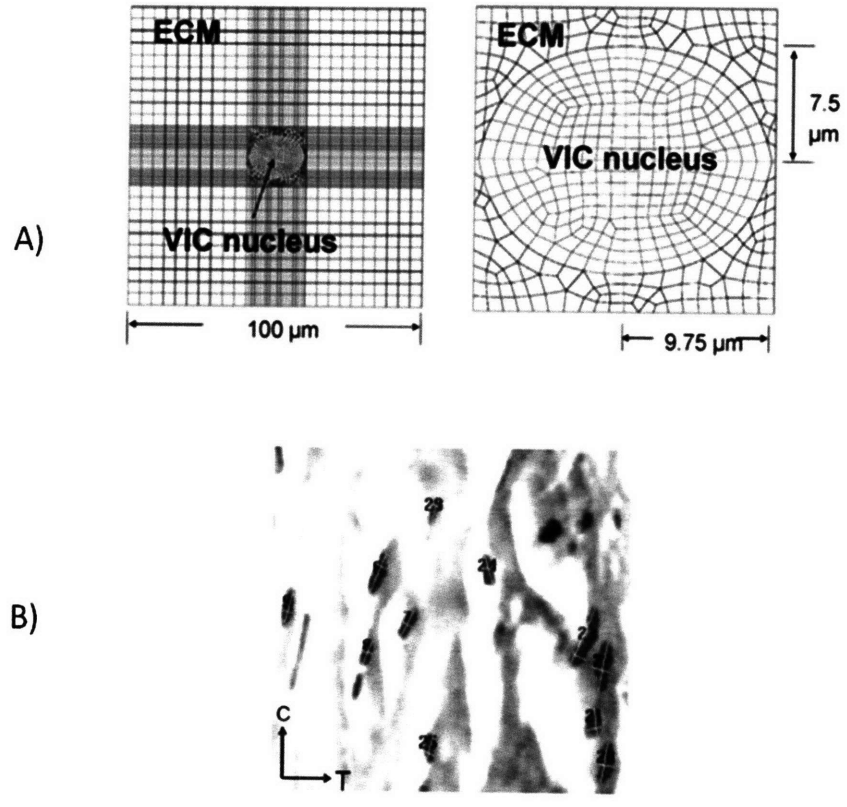


Figure 1.22.B. In this thesis we will introduce a system of reference configurations to link the length scales[193]. Within this framework, illustrated in Figure 1.23, we will compute organ scale motion, from which tissue scale deformations will be extracted, and tissue deformation will similarly be translated to the cell scale. The complete model presented in this thesis is thus a

dynamic, three-dimensional simulation of AV mechanics spanning the cell, tissue, and organ length scales.

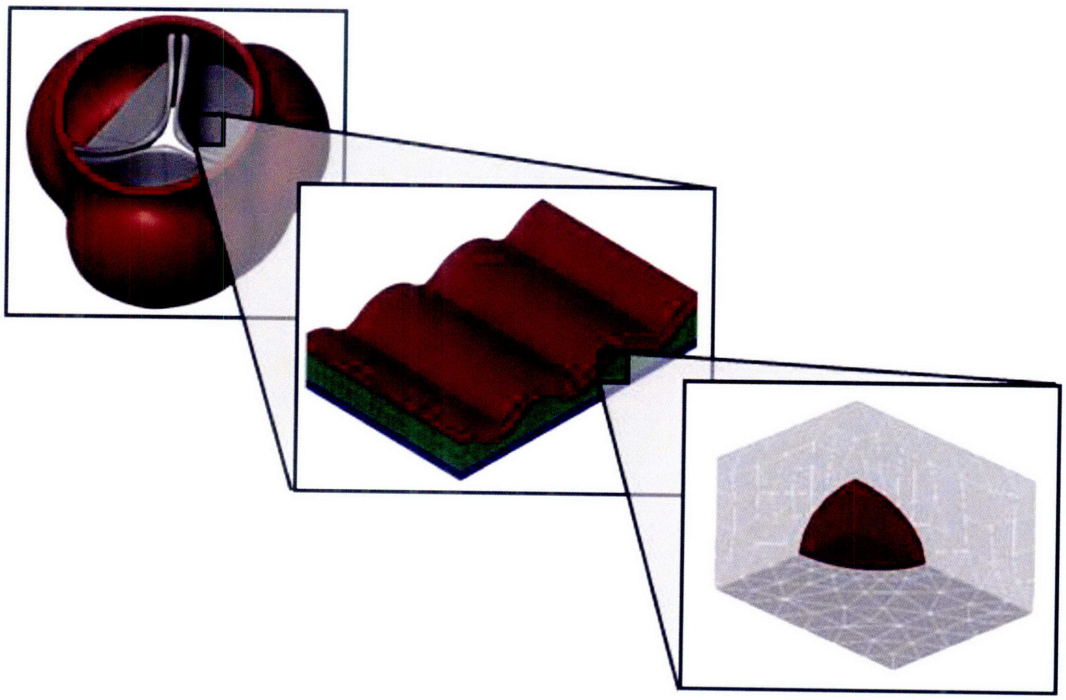

**Figure 1.23.** Linking of multiscale AV mechanical simulations from the organ scale to the tissue and cell scales[193]

## Conclusions and Future Directions

Investigating the healthy and diseased processes in heart valves is a complex, multi-scale, multi-disciplinary effort with important clinical outputs. Research in this field has already contributed enormously to patient care, most notably the development of prosthetic and bioprosthetic valve replacements. Simulation of valve mechanical behavior is a vital tool in improving valve replacement design as well as in increasing our fundamental understanding of valve behavior.

Many researchers have modeled valve mechanics at the tissue and organ scales over the past three decades. In the past five years, research has begun on mechanics at the molecule and cell scales, as well as on mechanical behaviors spanning multiple length scales. Heart valve researchers have consistently drawn on cutting edge experimental and theoretical methods and pushed for advancements where existing tools were insufficient. A number of groups are currently active in developing the next generation of experimental tools, numerical methods, and mechanical simulations of the human heart valves.

Simulation of heart valves is expected to progress in a few main directions. First, models of organ and tissue scale mechanics have gone through generations of refinement where tissue and cell scale models are currently in their first generation. Researchers will work to bring the smaller-scale simulations to the same level of sophistication as the larger-scale models. Models that link the length scales are also in their infancy, and researchers will further refine multiscale methods.

Refinement of models will surely continue, but to have significant clinical impact and to increase our fundamental understanding of the valves these simulations must be joined performed in concert with experimental efforts. Recent efforts combining multiscale modeling with experiment have elucidated the deformation of ICs in response to valve motion[94] and, as described in this thesis, the phenotypic expression of ECs in response to blood flow through the valve[189]. Further multiscale, multidisciplinary efforts will similarly increase our ability to understand valve function and treat valve disease.

## Outline of Thesis

The goals of this thesis are to create a multiscale mechanical model of the human aortic heart valve and to use that model in an examination of CAS. The following is an outline of the approach taken to create and apply the model.

In Chapter 2, we develop the model. The first step is creation of a framework of reference configurations, through which the simulations at various scales can communicate. After that, dynamic, finite-element simulations of the cell, tissue, and organ scale mechanics are formulated. The cell scale model simulates a single IC surrounded by matrix. The tissue scale model describes the valve cusp as a multilayered structure, with varying thickness and with each layer being anisotropic and nonlinear. At the organ scale, we simulate the dynamic interaction between tissue and blood in the valve. Each individual model and the overall multiscale simulation are verified against experimental data.

In Chapter 3, we extend this model to simulate the effect of aging on the valve, with and without calcification. Normal aging is described by a thickening and stiffening of the cusp tissue. Calcification is introduced at the tissue level and allowed to spread across the cusp over time. The effect of these tissue-level changes on valve function is monitored at the organ scale, and compared to clinically accepted indices for valvular function.

In Chapter 4, we apply the multiscale model to investigate one facet the role of solid deformations in CAS. CAS is much more common in the abnormal, bicuspid AV than in the normal, tricuspid valve. Since the bicuspid valve has different mechanical deformations than the tricuspid, this provides a test case for analyzing the role of such deformations in CAS. A

multiscale model of the bicuspid valve is developed, and the multiscale mechanics are compared to those of the tricuspid. We find that, while organ scale deformations are significantly different, deformations at the cell scale in the two cases are similar. This work provides evidence that supports the argument that the difference in CAS pathology between the two valves has a cause other than the difference in mechanical deformations.

In Chapter 5, we use a combination of simulation and experiment to examine the role of fluid shear in CAS. An organ scale simulation is created with high resolution on the boundaries in order to calculate the transient shears applied to the ECs. Those shears are then applied in vitro to human ECs. We show that shear waveforms measured on each side of the cusp direct the ECs to express different phenotypes. These side-specific phenotypes correlate well with those observed in vivo and with the side-specific nature of CAS. This work provides evidence for the theory that shear has an important signaling role in CAS.

# Chapter 2. Transient, three-dimensional, multiscale simulations of the human aortic valve

## Introduction

Biological processes in both the healthy and diseased aortic valve (AV) occur over a range of length scales. Cells within the valve cusps, the valvular interstitial cells (ICs), are understood to sense and respond to mechanical stimuli. The ICs are subjected to transient deformations due to the organ-scale motion of the valve opening and closing. Currently, we understand that in healthy valves the transient deformations regulate appropriate matrix-maintaining functions of the ICs[177]. In diseased states, particularly in calcified valves, it is thought that abnormal mechanical signals lead to IC dysfunction[134]. Additionally, calcification of bioprosthetic valves is believed to be a local effect of cusp deformation. As the health and repair of heart valves is of great clinical importance, significant research has been conducted to examine the mechanical behavior of the AV at each length scale.

The organ-scale motion of the AV has historically attracted significant attention from experimental and theoretical groups. Over the past three decades, many methods have been employed to monitor the motion of the AV. Its small size and rapid motion make measurements challenging, but imaging technologies have recently demonstrated the acquisition speed and resolution to discern valve motion[9, 20]. Earlier efforts have measured valve motion using

surgically attached linear transducers [23] and radio-opaque markers[49, 180, 182], stereophotogrammetry[41], and silicone casting[29, 30, 78].

A number of groups have used finite-element modeling to simulate the motion of the AV. There are two main challenges in creating a finite-element simulation of a heart valve. First, the leaflets undergo large displacements through the blood, making remeshing of a fluid domain difficult for a coupled fluid-structure interaction. While fluid-structure interactions are generally approached using the Arbitrary Lagrange-Eulerian (ALE) coupling scheme, we are not aware of any work that successfully applies this method to a 3D valve simulation. The second challenge in simulating valve motion is that the material is anisotropic and nonlinear. Kim *et al* have modeled the valve motion with a specifically derived material model, but without the fluid phase[99, 100]. De Hart *et al* have implemented a fictitious domain method for coupling the fluid and solid without remesh of the fluid domain, and they have used this method to simulate the motion of the AV cusps with a fiber-supported constitutive material model[46-48]. The finite element package LS-DYNA (LSTC, Livermore CA) includes the operator-splitting method which similarly couples solid to fluid without remeshing the fluid domain[84]. This software has been used to perform fluid-structure interactions of the AV, including the motion of the aortic root, with an anisotropic linear elastic material model[131] and to simulate the mitral valve with a user-defined fibrous material model[56, 57]. A number of groups have simulated the valve solid without fluid or under quasistatic conditions. Sun provides a full list of such efforts[172].

A large body of research also exists in the measurement and simulation of the mechanical properties of AV tissue. The planar stress-strain behavior of complete tissue[13, 41, 151] and individual layers[160, 186] have been measured as has the flexural stiffness of the tissue[154].

Merryman *et al* have measured the effect of cellular contraction on the overall tissue material properties[122]. Various appropriate constitutive models have been formulated[14, 91] and implemented in solid and shell finite elements[99, 173, 191, 192].

Modeling of cell-scale deformations in general is an active area of research[116], but investigations specific to the ICs are in the preliminary stages. Merryman *et al* have measured the stiffness of ICs[123] and Huang *et al* have computed the deformation of ICs in valves subjected to static pressure[93].

While the mechanical behavior of the AV at the various length scales is a subject of wide interest, and multiscale analysis of other systems has been performed[32, 124], as of yet no effort has been made to cohesively bring together studies of the AV over the range from cellular to organ length scales. Understanding of all these processes will be greatly enhanced by a coherent framework for examining the deformations of the AV at the various length scales. In this chapter, we introduce a system of reference configurations to link the length scales. We describe finite-element simulations of AV mechanics at the cell, tissue, and organ length scales. Each simulation considers the transient, three-dimensional case with appropriate material models and geometry. The complete set of simulations enables unprecedented analysis of the AV behavior across the range of length scales from cell to organ.

## Methods

### *Multi-scale approach*

Simulations were created to describe behaviors at the cell, tissue, and organ length scales. One challenge in describing AV mechanics is that the tissue goes through a wide range of deformations and these deformations may be referred to a range of reference configurations. Stella[160] and Billiar[14] have demonstrated the large difference in results possible when different reference configurations are assumed. In order to coherently link our simulations, we have defined a set of reference configurations. Our configuration definitions extend those of Stella[160]. These configurations are summarized in Table 2.1. In $\Omega_0$, the ventricularis and fibrosa are unattached and stress-free. The layers are connected to form the assembled tissue $\Omega_1$. In $\Omega_2$, the tissue is in position in a valve to which no pressure has been applied. When the valve is pressurized to its resting physiological state, the tissue is in $\Omega_3$. We denote the time-varying state of the tissue in the functioning valve as $\Omega_t$.

**Table 2.1.** Tissue reference configurations

| Symbol | Schematic | Description | Extensibilities |
|---|---|---|---|
| $\Omega_0$ | 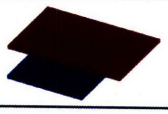 | unattached layers | fibrosa: $\lambda_C = 1.10$, $\lambda_R = 1.40$<br>ventricularis: $\lambda_C = 1.20$, $\lambda_R = 1.90$ |
| $\Omega_1$ |  | assembled tissue | fibrosa: $\lambda_C = 1.10$, $\lambda_R = 1.40$<br>ventricularis: $\lambda_C = 1.20$, $\lambda_R = 1.70$<br>tissue: $\lambda_C = 1.10$, $\lambda_R = 1.70$ |
| $\Omega_2$ | 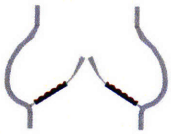 | tissue in valve with no external forces applied | tissue: $\lambda_C = 1.10$, $\lambda_R = 1.25$ |
| $\Omega_3$ |  | tissue in valve with baseline pressure applied | tissue: $\lambda_C = 1.05$, $\lambda_R = 1.20$ |
| $\Omega_t$ | 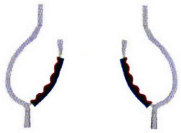 | tissue in functioning valve | tissue, mid-diastole: $\lambda_C = 1.00$, $\lambda_R = 1.00$ |

The leaflet tissue exhibits locking behavior, where the stress needed to extend the tissue increases rapidly beyond some point. We define the extensibility of the tissue to be the stretch that can be applied to the tissue before the Cauchy stress exceeds 200KPa in the direction of application. The extensibility of the leaflet tissue in each reference configuration, in both the circumferential and radial directions, can be determined from published experiments. The measured extensibilities of individual layers referred to $\Omega_0$ are listed in Table 2.1[160]. Stella's data show an increase in radial extensibility for the fibrosa from $\Omega_0$ to $\Omega_1$. This increase is most likely due to the fibrosa being compacted into a wrinkled shape. We include the wrinkling effect in our models, so we assume that the fibrosa material has the same radial extensibility $\Omega_1$ as in $\Omega_0$. The extensibilities of the assembled tissue referred to $\Omega_1$ were estimated to be 1.7 in the radial direction and 1.2 in the circumferential direction[13]. The extensibilities referred to the valve configuration $\Omega_2$ are determined by assuming that the tissue reaches its locking stretches in both directions in diastole. The stretches at diastole have been measured[29, 179] to be 1.25 in the radial direction and 1.1 in the circumferential direction. The extensibilities referred to $\Omega_3$ are not known *a priori*. For illustrative purposes, we assume that a small stretch (1.05) is applied to the tissue in both directions between $\Omega_2$ and $\Omega_3$. The magnitude of the stretch occurring between $\Omega_2$ and $\Omega_3$ will be calculated in the organ-scale simulation.

Once the extensibilities are known, we can calculate the stretches that are applied to the tissue in each configuration. With those stretches, we can begin at any configuration and calculate the stretches required to reach any other configuration. In

Figure 2.1, the stretches required to move from $\Omega_0$ to all other configurations in sequence are plotted. Note that a large stretch in the radial direction between $\Omega_1$ and $\Omega_2$ is required to reconcile the measured extensibility of completely load-free tissue[13] with the observed extensibility of tissue in a functioning valve[29, 179]. Thus, we are assuming that leaflet tissue, in an AV with no external forces applied, has tension in the radial direction. The stretch less than 1 in the radial direction for the fibrosa represents the wrinkling of this layer when the fibrosa and ventricularis are attached to each other.

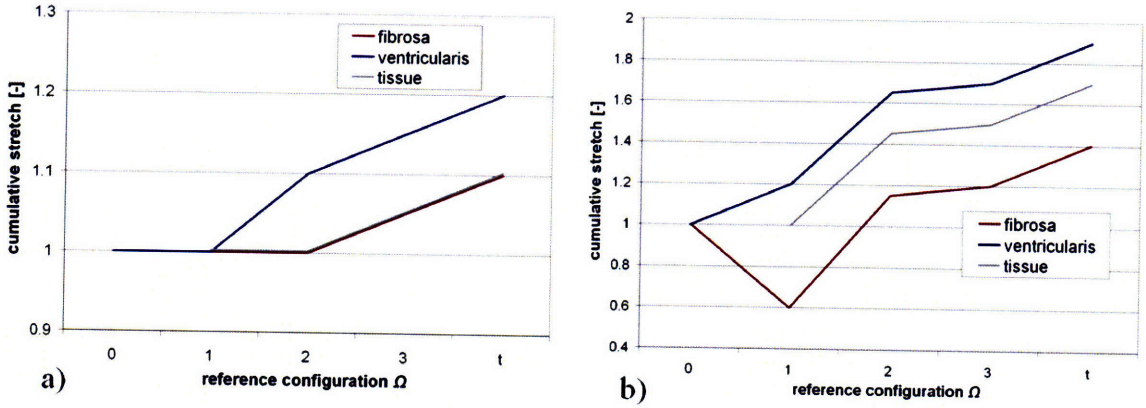


**Figure 2.1.** Cumulative stretches required to reach any configuration starting at $\Omega_0$

We create our multiscale simulations within the framework of these reference configurations. For each simulation, a reference configuration is chosen and the simulation geometry and constitutive models are referred to that configuration. The simulations are listed in Table 2.2 with their length scales, reference configurations, and the configurations that they span.

**Table 2.2.** Simulation scales and configurations

| Simulation | Feature Size Range | Reference Configuration | Configurations Simulated |
|---|---|---|---|
| Cell-scale | 2μ - 50μ | $\Omega_2$ | $\Omega_2$ - $\Omega_t$ |

| | | | |
|---|---|---|---|
| Tissue-scale | 50μ - 1mm | $\Omega_1$ | $\Omega_1 - \Omega_t$ |
| Organ-scale | 1mm - 3cm | $\Omega_2$ | $\Omega_2 - \Omega_t$ |

These simulations are interfaced by a simple one-way coupling, passing data from the largest scale to the smallest. First, the organ-level simulation is run. Element strains output from the organ-level simulation are applied as boundary conditions to the tissue-level simulation. Then strains from the tissue-level simulation are passed similarly to the cell-level simulations.

*Organ-level simulation*

The organ-level simulation was performed in LS-DYNA. This software was chosen because its operator-splitting method for fluid-structure interaction has been demonstrated to readily handle the motion of a solid through fluid typical of heart valve function[56, 131]. LS-DYNA is an explicit solver, which means it may require excessive computation times in modeling relatively low-speed physical systems such as the AV. We address this issue in our formulation of the constitutive model used to describe the cusp tissue mechanics.

To simulate the cusp mechanics, we have developed a constitutive model that describes the bulk material behavior and is particularly computationally efficient in explicit finite element codes. Like many tissue constitutive models[14, 91, 95, 173], ours treats the tissue as an isotropic solid with embedded aligned fibers. Instead of using a continuum model, though, we take a discrete approach. The solid mesh elements are modeled with an isotropic material. One-dimensional cable elements are then used to connect the nodes of the solid element. LS-DYNA allows

assignment of arbitrary stress-strain curves to the cable elements, and fiber rotations follow nodal displacements. A single element with this model is illustrated in Figure 2.2. Red cylinders represent fibers of one family and blue represent fibers of another family, perpendicular to the first.

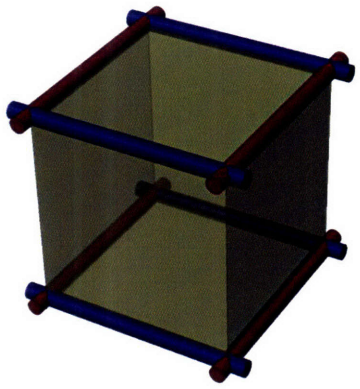

**Figure 2.2.** Single solid element with two perpendicular fiber families

Appropriate stress-strain curves and cross-sectional areas must be chosen for each fiber. It is assumed that the fibers contribute no stiffness in compression. There is some flexibility in choosing the magnitude of the stresses and the cross-sectional area of the fibers. If an element with fibers along each edge is extended in a direction parallel to those fibers, the stress contribution of the fibers to total element response is

$$\sigma_c = \frac{4\sigma_f A_f}{A_e}, \qquad \text{(Eq. 2.1)}$$

where $\sigma_f$ is the stress in each fiber, $A_f$ is the cross-sectional area of each fiber, and $A_e$ is the cross-sectional area of the solid element. Thus, $\sigma_c$ should have a value corresponding to measured tissue properties and $A_e$ is determined by the mesh density, but the ratio of $\sigma_f$ to $A_f$

can be arbitrary. This property can be utilized to enhance the computation speed when using the discrete fiber model in an explicit finite element code. In the explicit method, the maximum allowable time step is decreased as element stiffness is increased. Because in our model the greatest stiffness is found in the fibers, these will control the maximum time step. In a one-dimensional element the maximum allowable time step is

$$\Delta t_{\max} = L\sqrt{\frac{\rho}{E}}, \qquad \text{(Eq. 2.2)}$$

where $L$ is the length of the element, $\rho$ is the density of the element, and $E$ is the maximum material modulus[84]. The stiffness of a nonlinear cable element at a given strain $\varepsilon_o$

$$E = \left.\frac{\partial \sigma}{\partial \varepsilon}\right|_{\varepsilon=\varepsilon_o}. \qquad \text{(Eq. 2.3)}$$

As such, a fiber can be defined with artificially high cross-sectional areas $A_f$ and corresponding artificially low stress $\sigma_f$. The resulting element will have low stiffness $E$, and thus allow large timesteps, while still giving the correct overall element stress $\sigma_c$.

The discrete fiber model was implemented in LS-DYNA. The constitutive model was constructed referring to the tissue configuration $\Omega_2$. The isotropic solid was modeled as a single-term Mooney-Rivlin with the value $C_1$ = 2.0e4 chosen to fit bending data for the leaflet[154]. The stress-strain curves in the radial and circumferential direction measured experimentally for configuration $\Omega_2$[160] were discretized and applied to the fiber elements. Curves for $\sigma_c$ were fit to the data and curves for $\sigma_f$ were calculated using

(Eq. 2.1)

and a value of 1.0e-3 $m^2$ for $A_f$. The aortic root was assumed to be anisotropic and modeled with a single-term Mooney-Rivlin material. A value of $C_1$=1.0e5 was fit to experimental pressure-versus-dilation data for the root[110].

Geometry of the AV was created in SolidWorks (SolidWorks, Concord MA). Separate loft features were used to represent the root and cusp. Dimensions were determined from collected measurements of the gross geometry[179] and varying cusp thicknesses[79]. Cusps were positioned in an unloaded configuration that, according to observations of explanted valves made in our lab, best represents the unloaded configuration $\Omega_2$. Figure 2.3.A shows the 3D geometry of the valve, with colors representing the separate loft features. Perfect symmetry of the valve was assumed so that only one-sixth of the valve needed to be considered for simulation. Entry regions were added both to allow the root to move freely while the portions of the wall at the inlet and outlet remain fixed to the stationary fluid sources. The solid domain consisting of valve, root, and entry regions was embedded in a cylindrical fluid domain with source regions representing fluid interface with the ventricle and aorta. Figure 2.3.B shows the simulation geometry with 1/6 symmetry, entry regions, and fluid. Parametric 8-node brick meshes of both the solid and fluid domains were created in TrueGrid (XYZ Scientific Applications, Inc., Livermore CA). Figure 2.3.C shows the meshed geometry.

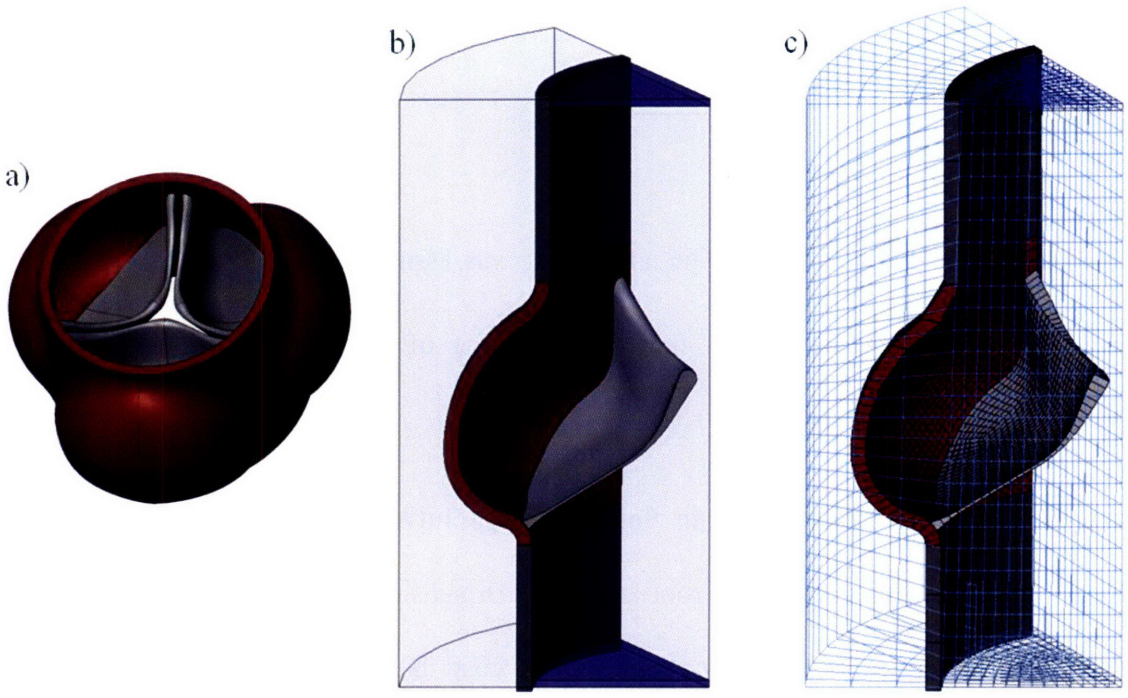


**Figure 2.3.** a) CAD geometry of whole valve b) CAD simulation geometry c) meshed geometry

Cable elements representing circumferential and radial fiber families were overlaid on the solid mesh using HyperMesh (Altair Engineering, Troy MI), following observed fiber directions[158]. The fiber families are illustrated in Figure 2.4.

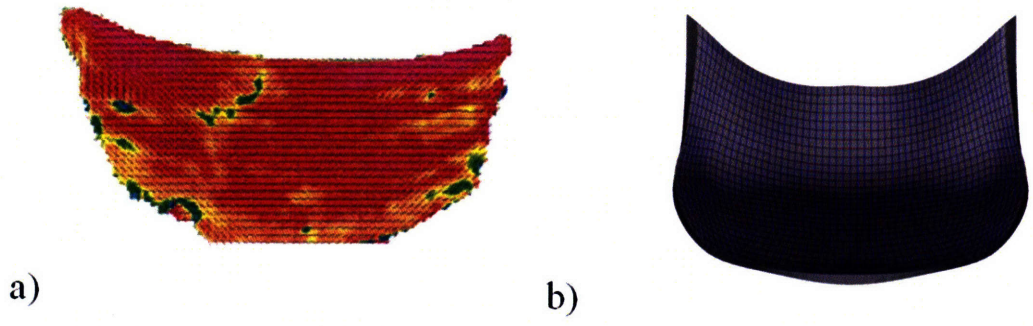


**Figure 2.4.** One cusp, with a) experimentally measured fiber orientation [158] and b) discrete fibers overlaid on the solid mesh. Red represents circumferential fibers and blue represents radial.

Fixities and boundary conditions were applied to the mesh. Mirror conditions were applied to fluid and solid nodes on the two symmetry planes. The unattached ends of the entry regions were fixed while the nodes at the junction of the entry regions and the aortic root were constrained from moving axially. Outer faces of the fluid domain were not constrained.

Two cases were run in the organ-scale simulation, a static and a fully dynamic case. In the static case, constant pressures of 0, 1, 2, 4, 60, and 90 mmHg were applied at the aortic inlet sequentially. A settling time of 0.3 seconds was allowed at each pressure level. Pressure at the ventricular inlet was kept at 0mmHg and ventricular contraction was not applied in the static case. In the dynamic case, measured time-varying pressures for the aorta and ventricle[179] were applied as boundary conditions to the fluid sources. The pressure values are plotted versus time in Figure 2.5.A. Contraction of the ventricle was represented by applying an experimentally-derived[110] time-varying radial displacement to the base of the AV. The applied dilation of the base is plotted in Figure 2.5.B. In Figure 2.5, the time from $-0.3 < t < 0$ represents the pressurization of the valve from configuration $\Omega_2$ to $\Omega_3$. Configuration $\Omega_t$ is any state where $t > 0$. Systole occurs for approximately $0 < t < 0.25$ and diastole for $0.3 < t < 1.0$. All temporal plots in this paper are referred to this timeframe.

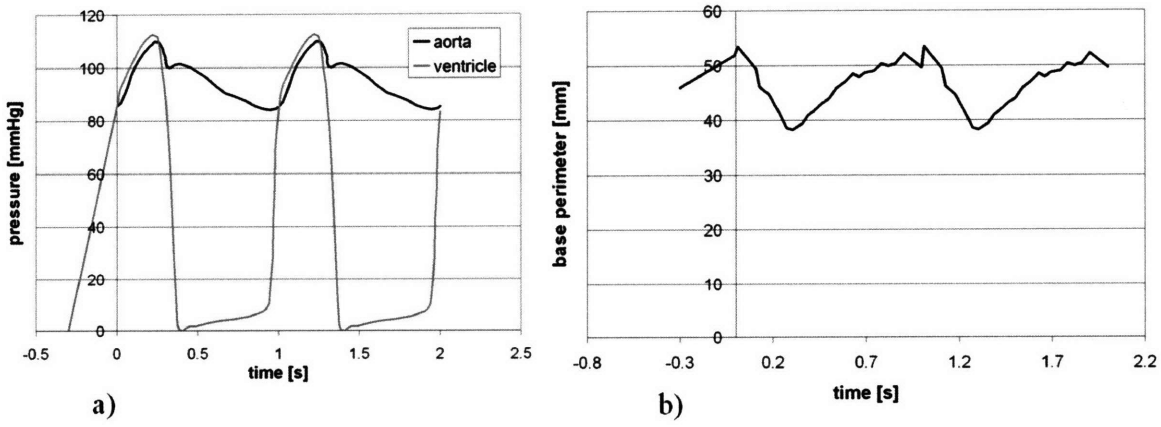

**Figure 2.5.** a) Pressure versus time curves applied as model boundary conditions b) Dilation of AV base applied as model boundary condition

Results of the organ-level simulation were processed in HyperView (Altair Engineering, Troy MI). The model was verified by comparing a number of behaviors in the solid and fluid to experimental data. Element deformations were tracked at three locations for mapping to the tissue-level simulation. These three locations are illustrated in Figure 2.6.

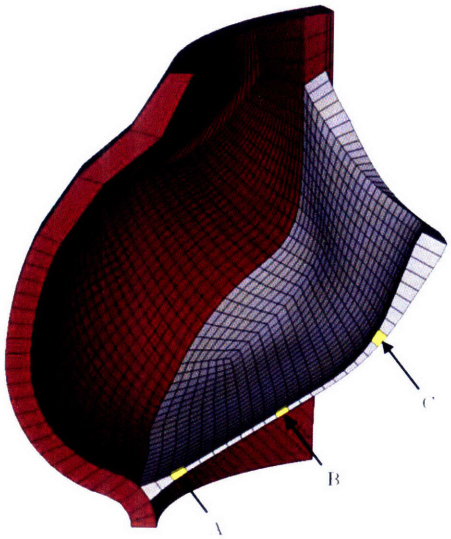


**Figure 2.6.** Locations to track deformations in the organ-scale simulation

*Tissue-level simulation*

In the organ-level simulation, we use a greatly simplified model of the cusp tissue. This simplified model gives the correct bulk behavior (bending and biaxial stiffness), but does not predict local tissue deformations. In order to predict the local deformations, we developed a tissue model that incorporates all of the major known features of the cusp tissue. These characteristics are: the cusp has three distinct layers (the ventricularis, spongiosa, and fibrosa),

the fibrosa and ventricularis have embedded families of aligned fibers, the fibrosa is highly undulated, and the spongiosa is gel-like.

We created the tissue-level model in the ADINA implicit finite-element software (ADINA R&D, Watertown MA). Computational cost is not a concern so, unlike in the organ-scale model, we can use continuum material models. We considered the fibrous layers to be composed of an isotropic exponential material with a family of embedded exponential fibers running in the circumferential tissue direction. Additionally, bending data[154] show that the tissue has an initial modulus.

We modeled the isotropic exponential material with a single-term Fung-like exponential[72]. The strain energy function for this term is

$$W_{exponential} = C_{1m}\left\{\exp\left[C_{2m}\left(I_1 - 3\right)\right] - 1\right\}, \qquad \text{(Eq. 2.4)}$$

where $C_{1m}$ and $C_{2m}$ are constants that will be calculated from experimental data and $I_1$ is the first strain invariant. We provide an initial modulus with a single-term Mooney-Rivlin, for which the strain energy function is

$$W_{initial} = C_I\left(I_1 - 3\right), \qquad \text{(Eq. 2.5)}$$

where $C_I$ is a constant that will be calculated from experimental data. The embedded fiber family is modeled using the Holzapfel model[91],

$$W_{fiber} = \frac{C_{1f}}{2C_{2f}}\left\{\exp\left[C_{2f}\left(I_4 - 3\right)^2\right] - 1\right\}, \qquad \text{(Eq. 2.6)}$$

where $C_{1f}$ and $C_{2f}$ are constants that will be calculated from experimental data. The complete strain energy function for a fibrous layer is a sum of the terms above,

$$W = C_{1m}\{\exp[C_{2m}(I_1 - 3)] - 1\} + C_I(I_{1-3}) + \frac{C_{1f}}{2C_{2f}}\{\exp[C_{2f}(I_4 - 3)^2] - 1\} \qquad \text{(Eq. 2.7)}$$

We modeled the spongiosa with a single-term Mooney-Rivlin strain energy function.

The fiber layers are described by five constants: $C_I$, $C_{1m}$, $C_{2m}$, $C_{1f}$, and $C_{2f}$. We calculate these values from experimental data. Sensitive measurements of the tissue flexural stiffness simply give the initial modulus. We assume that the initial modulus is the same in the ventricularis and fibrosa and that the stiffness of the spongiosa, which is much more compliant[186], is an order of magnitude lower.

Constants of the exponential terms were determined from biaxial stress-strain data for the individual layers[160]. Two values were extracted for both the radial and circumferential tissue directions. A locking modulus $E_L$ is defined as the Young's modulus in the direction of interest when the tissue reaches full extensibility in that direction. The extensibilities and locking moduli in the circumferential and radial directions are adequate to analytically solve for the four remaining constants, $C_{1m}$, $C_{2m}$, $C_{1f}$, and $C_{2f}$. The extensibilities, moduli, and determined constants, are listed in Table 2.3. We have calculated the constants referred both to configuration $\Omega_0$ and $\Omega_1$.

**Table 2.3.** Tissue layers and properties in configurations $\Omega_0$ and $\Omega_1$

| | | Extensibility | | Locking modulus | | | | | | |
|---|---|---|---|---|---|---|---|---|---|---|
| Layer | Configuration | circumferential | radial | circumferential | radial | $C_l$ | $C_{1m}$ | $C_{2m}$ | $C_{1f}$ | $C_{2f}$ |
| | | [-] | [-] | [Pa] | [Pa] | [Pa] | [Pa] | [-] | [Pa] | [-] |
| fibrosa | $\Omega_0$ | 1.1 | 1.4 | 2.6e7 | 1.1e7 | 2.0e4 | 0.95 | 1.4e3 | 0.04 | 24 |
| | $\Omega_1$ | 1.1 | 1.4 | 2.6e7 | 1.1e7 | 2.0e4 | 0.95 | 1.4e3 | 0.04 | 24 |
| ventricularis | $\Omega_0$ | 1.2 | 1.9 | 1.6e7 | 5.0e6 | 2.0e4 | 2.5e-5 | 1.1e2 | 0.04 | 5.4 |
| | $\Omega_1$ | 1.2 | 1.7 | 1.6e7 | 5.0e6 | 2.0e4 | 2.5e-5 | 1.1e2 | 0.05 | 5.7 |

Geometry for the model of assembled tissue, configuration $\Omega_1$, was created in SolidWorks. The dimensions are based on measurements of tissue thickness[160, 186] and observations of tissue cross-sections.

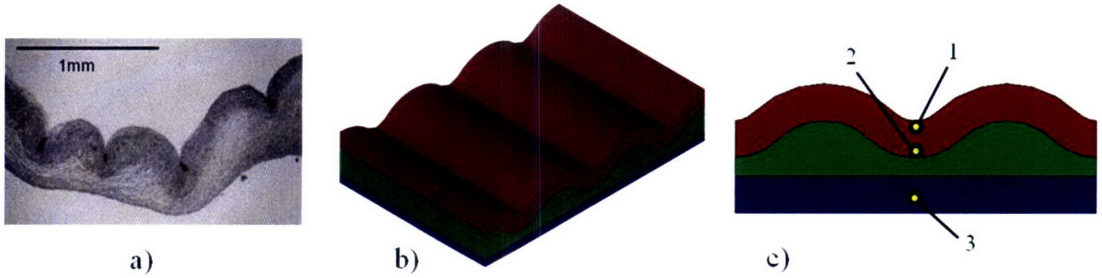


a) b) c)

Figure **2.7**.A shows a micrograph cross-section of valve cusp tissue, and

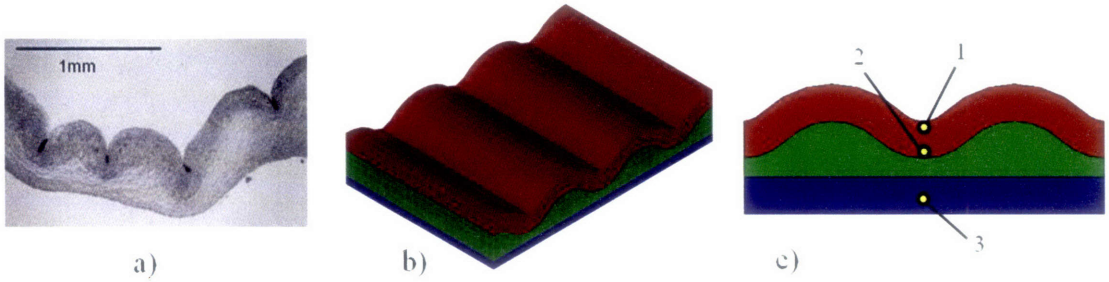


Figure **2.7**.B, the meshed CAD representation of this geometry. Material properties from Table 2.3 were assigned to the appropriate layers in configuration $\Omega_1$. Biaxial stress and bending conditions were applied to the assembled tissue, and the results were compared to experimental data[13, 154]. Each term in (Eq. 2.7) is convex over a wide range of deformations, so the complete equation was also expected to maintain convexity. We examined convexity on the ventricularis and fibrosa models by calculating the strain energy over a wide range of biaxial conditions.

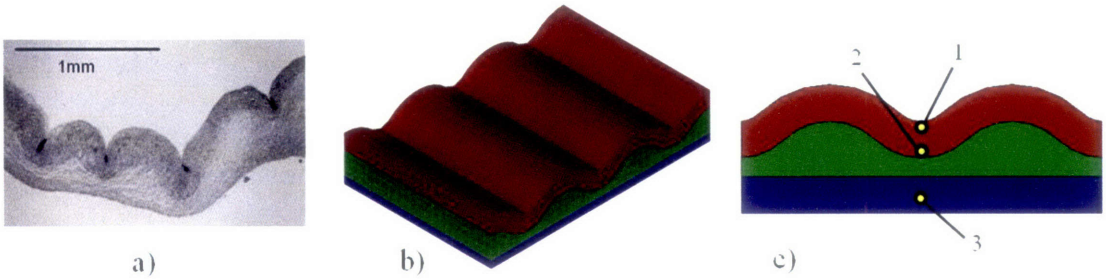


**Figure 2.7.** a) micrograph of AV leaflet cross-section[174] b) meshed model of AV leaflet c) locations for deformation tracking

We used the model of the multilayered tissue referred to configuration $\Omega_1$ to map deformations from the organ-scale model to the cell-scale model. First, a radial stretch was applied to move the tissue from configuration $\Omega_1$ to $\Omega_2$, its position in the unpressurized valve. Then element strains measured in the organ-level simulation, which covers configurations $\Omega_2$ through $\Omega_t$, were applied as time-varying displacement boundary conditions to the tissue model. Deformations at points

within the ventricularis and fibrosa, shown in

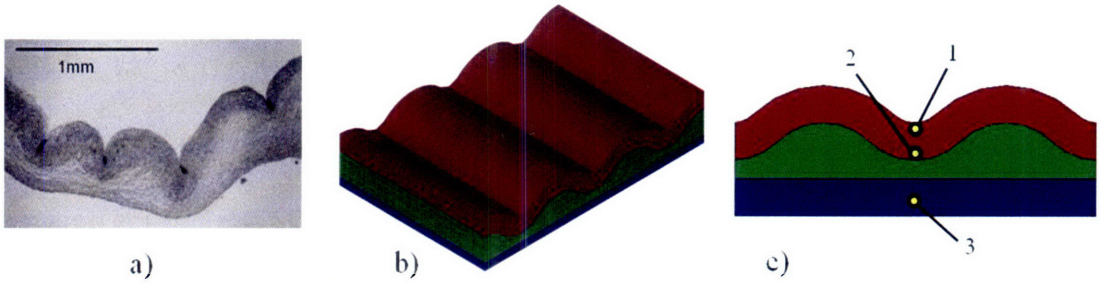


Figure **2.7**.C, were tracked and passed on to the cell-level simulation. Point 1 is in an expected high-deformation region of the fibrosa, Point 2 is in an expected low-deformation region of the fibrosa, and Point 3 is in the ventricularis. Mapping was performed for both the static and dynamic cases.

In addition to the model of the multilayered tissue, we have modeled the assembly of the tissue (transition from $\Omega_0$ to $\Omega_1$) with the observed preloading between fibrosa and ventricularis[184, 185]. A model fibrosa with mechanical properties referred to $\Omega_0$ was compressed and a fibrosa stretched using the values plotted in Table 2.3. While this model was not used in our current multiscale approach, it does allow prediction of deformations over the entire range from $\Omega_0$ to $\Omega_t$.

*Cell-level simulation*

The cell-level simulation consists of a single cell surrounded by matrix, either fibrosa or ventricularis. Constitutive models for the matrix are the same as those for the tissue-level model. The constitutive model for the cell is a single-term Mooney-Rivlin with $C_1$=400 Pa[93].

Geometry was created in ADINA. A sphere was created within cube and then scaled in the three dimensions to give the cell an ellipsoidal shape. According to experimental measurements[93], the major axes of this cell were defined to be 10μm in the circumferential direction, 7.7μm in the radial direction, and 4.3μm in the transmural direction. Three planes of symmetry were defined so that the computation domain consists of $1/8^{th}$ of the cell and matrix. The simulation geometry is shown in Figure 2.8.

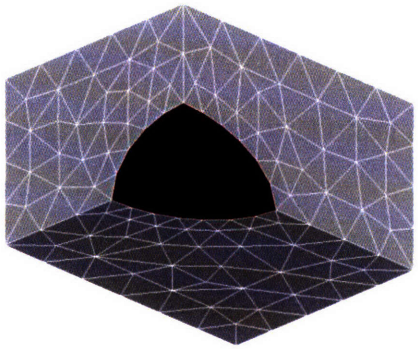

**Figure 2.8.** Meshed geometry for cell-scale simulation. Cell is colored red and matrix is gray.

Displacement boundary conditions were applied to the outer faces of the matrix. These displacements were defined to represent the element strains calculated in the tissue-level simulation. Because the relevant experiments[93] start with the valve in a zero-pressure state, we started our cell simulations in the unpressurized valve configuration $\Omega_2$. Cell aspect ratio (CAR) was output from the simulation. The model was verified by comparing results of the static case to experimental CAR measurements made under the same conditions [93]. Cell aspect ratio was also computed for the dynamic case of valve opening and closing.

**Results**

*Organ-level simulation*

The discrete fiber constitutive model was found to be adequate in predicting the bulk deformation behavior of the tissue. Figure 2.9.A shows the biaxial response of this model and Figure 2.9.B shows the bending response. Because we are not aware of any experimental data for tissue properties referred to the assembled valve configuration $\Omega_2$, we could not construct this model to match a specific case. Note, though, in Figure 2.9.A the similarity between our model predictions and the measurements made by Billiar referred to a lightly preloaded configuration[13]. This enforces the notion that the tissue exists in a lightly preloaded state in the valve.

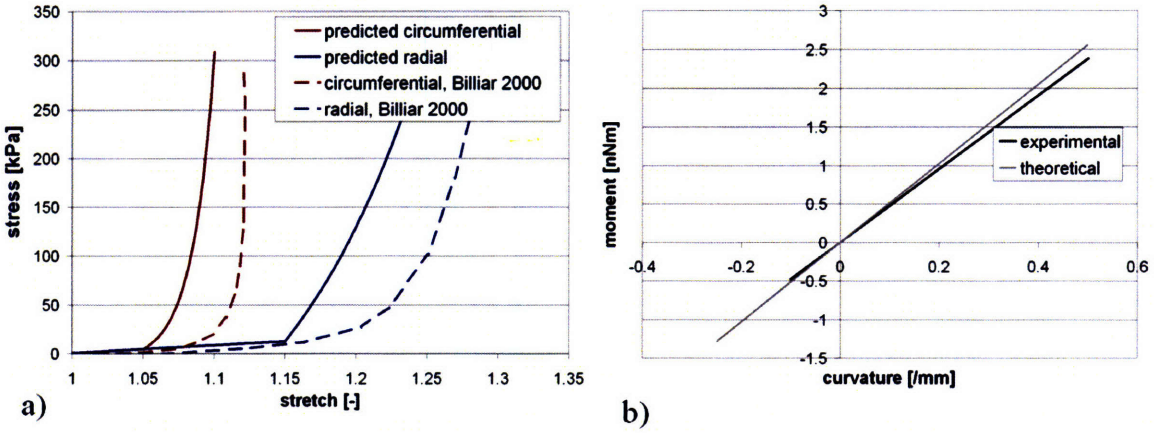


**Figure 2.9.** Discrete fiber model predictions and experimental results: a) predicted biaxial behavior and experimental data for a lightly preloaded case [13] b) predicted bending behavior and the experimental data [156] to which the model was fit

One second of physical time, representing either the full static case or one dynamic cycle of valve opening and closing, ran in approximately 3 hours of computation time on a workstation with 4 Xeon 5160 3.00 GHz processors. There was no leakage in the fluid-structure interaction, and the cusps coapted and sealed against flow. Figure 2.10.A shows the valve in various stages of the dynamic cycle.

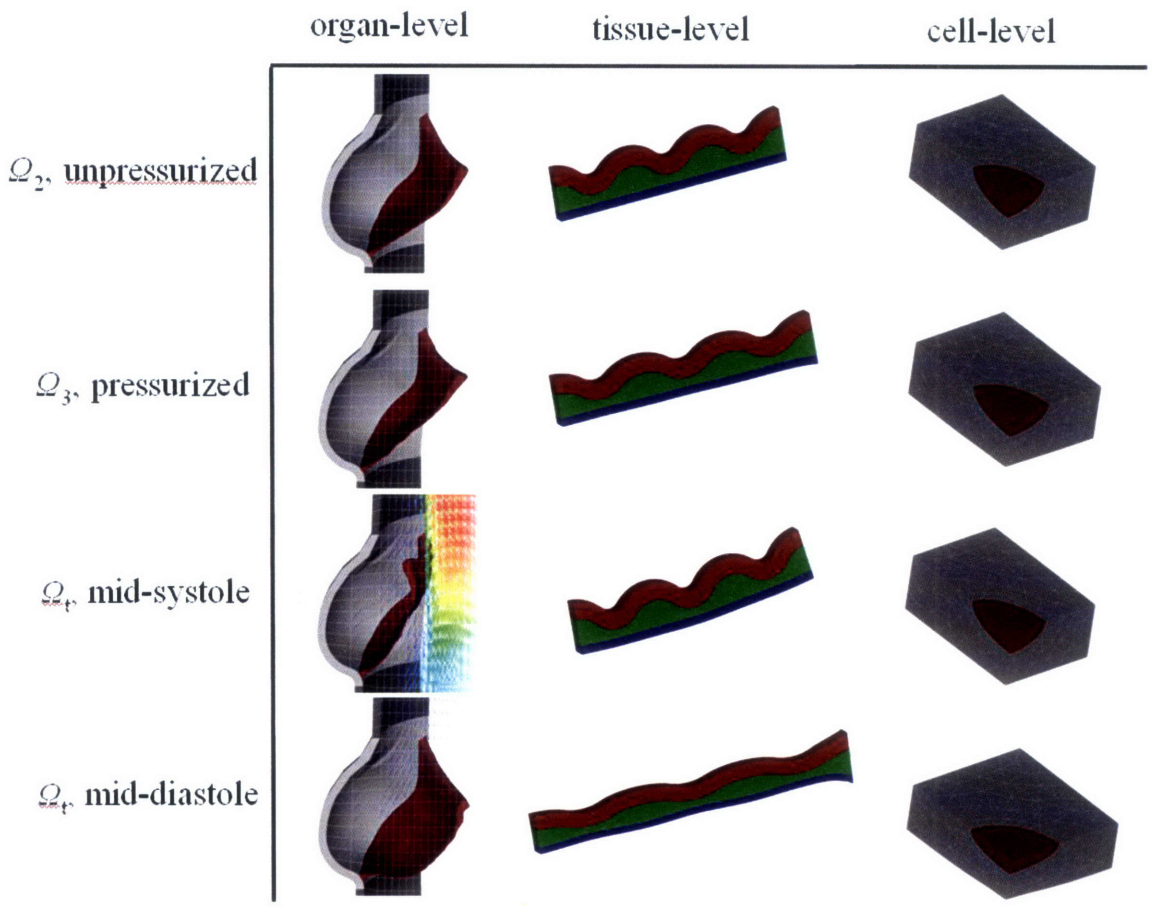


**Figure 2.10.** Selected deformed states in each dynamic simulation

For the dynamic case, theoretical predictions matched experimental data in a number of measures. In the fluid phase, the bulk flow rate through the valve closely corresponded with experimental data[130]. Velocity profiles predicted at various times across the AV outlet are compared to experimental measurements in Figure 2.11. Theoretical and measured flow rates are plotted versus time in Figure 2.12. In the solid phase, predictions were compared to experimental data for cusp edge and center displacement, circumferential strain, radial strain, and root motion[179]. These results are plotted in Figure 2.13. In the fluid and solid phase, predictions display all major trends with correct magnitudes when compared to measured data. Error

magnitudes are acceptable given patient-to-patient variation, beat-to-beat variation, and experimental errors inherent in measurement of the rapidly moving in-vivo system.

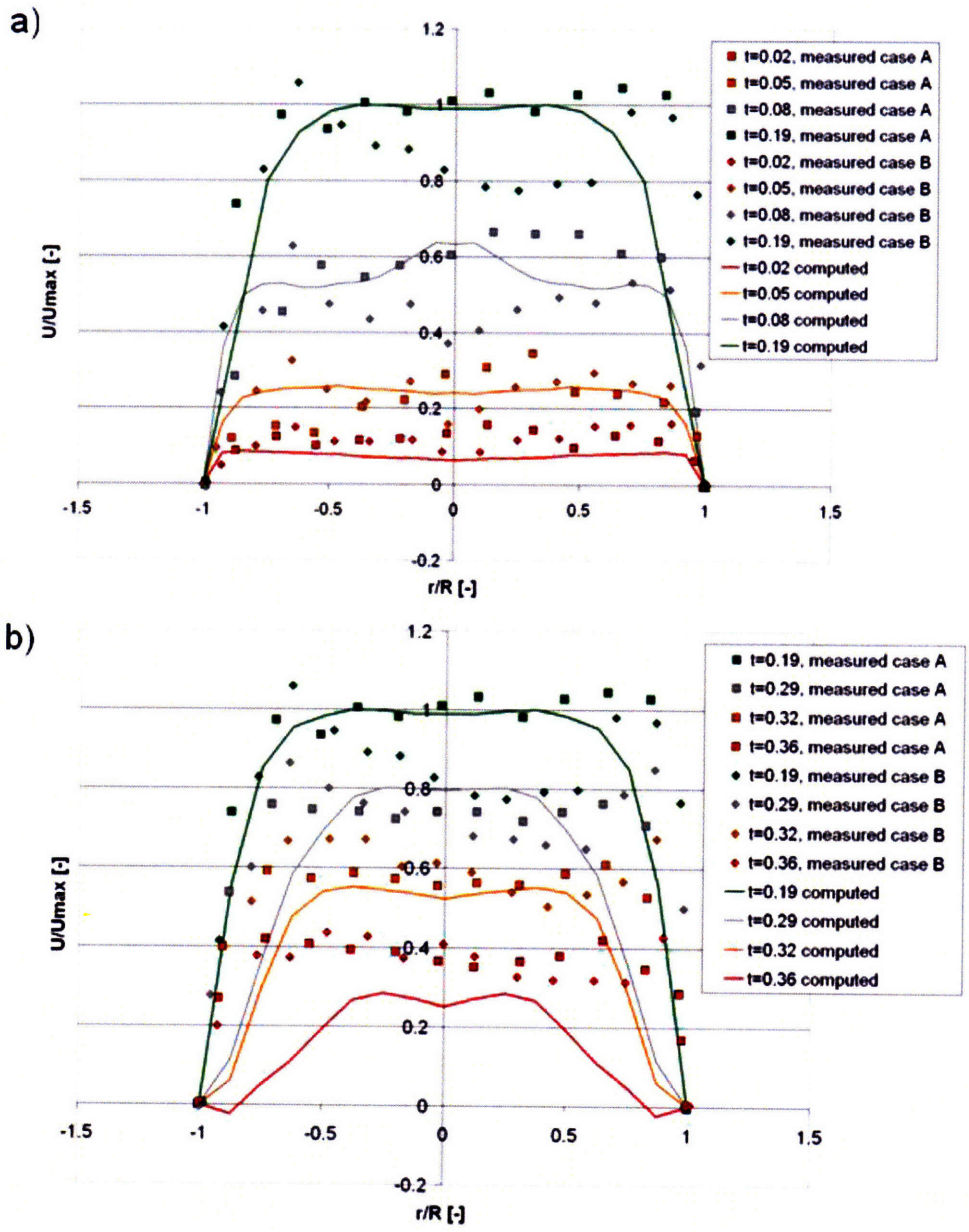


**Figure 2.11.** Predicted and measured velocity profiles at AV exit. a) shows profiles while the fluid is accelerating flow and b) during deceleration

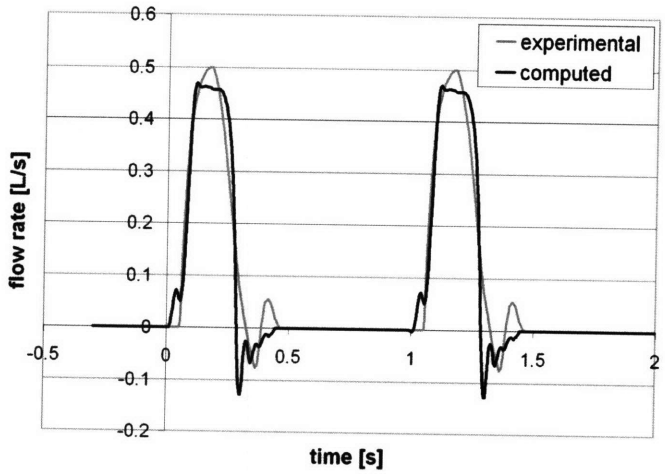


**Figure 2.12.** Predicted and measured flow rates through AV

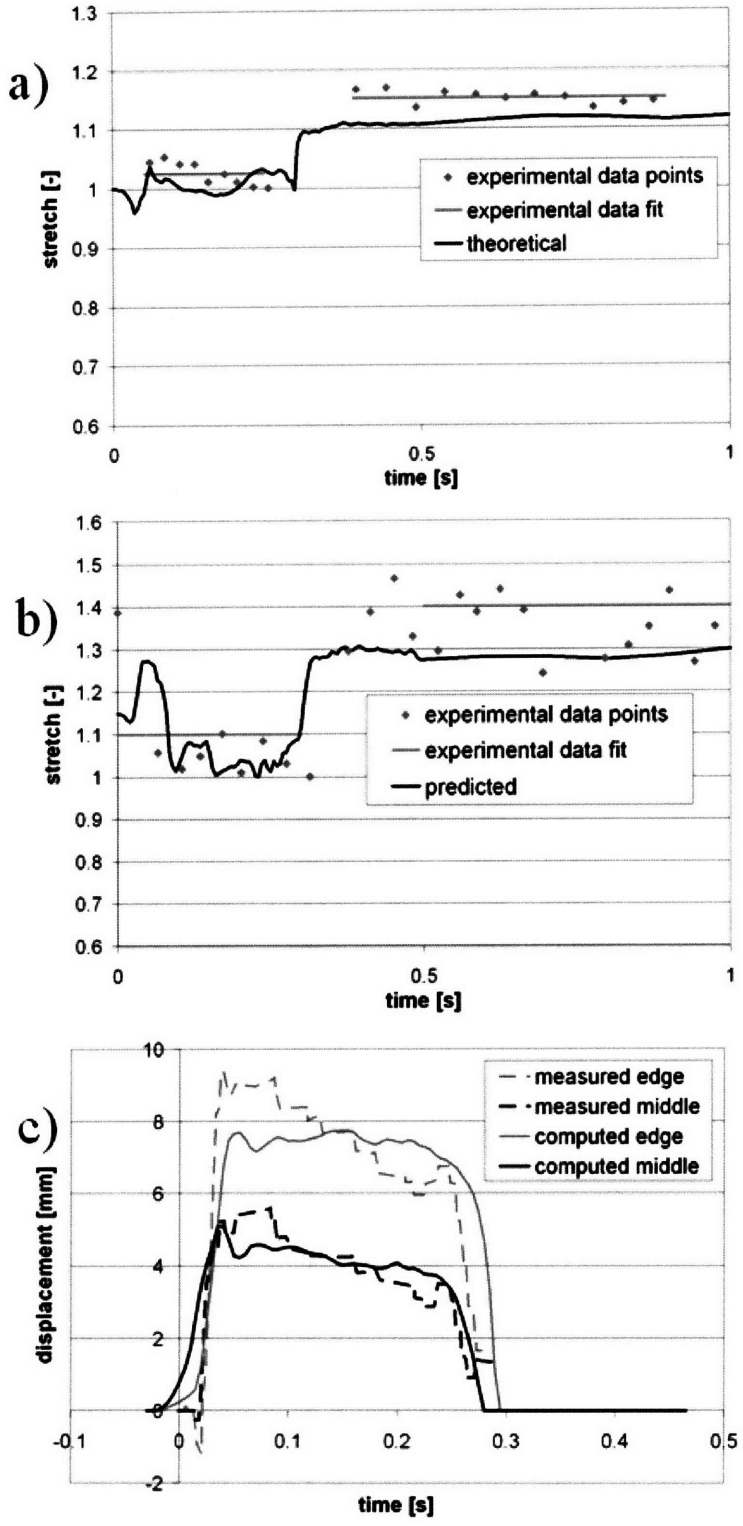


**Figure 2.13.** Predicted and measured[179] motion of valve leaflets: a) circumferential leaflet stretch b) radial leaflet stretch c) displacement of points at edge and middle of leaflet

Element stretches averaged over the locations illustrated in Figure 2.6 for the static case are shown in Figure 2.14. Deformations recorded in the dynamic case for location B shown in Figure 2.6 in the dynamic case are plotted versus time in Figure 2.15. Stretches for $t<0$ represent the unknown stretches between reference configurations $\Omega_2$ and $\Omega_3$ discussed earlier in this chapter. The dominant deformations were the tensile stretches in the radial and circumferential directions and the bending in the radial direction. In the tracked locations, shears in and out of the plane of the tissue as well as bending in the circumferential direction tended to be small and were not mapped to the tissue-level model.

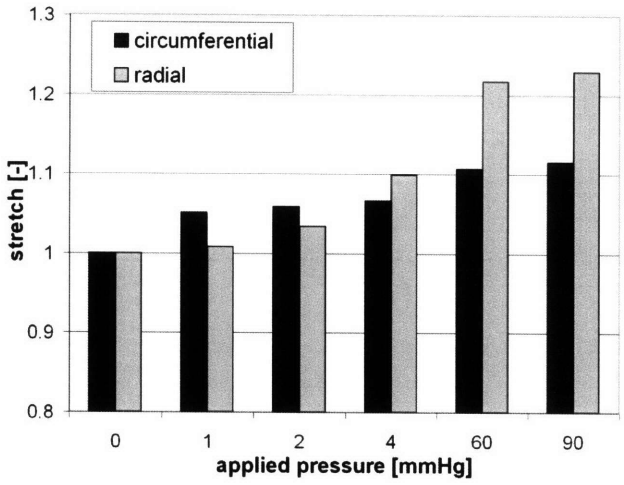


**Figure 2.14.** Element stretches predicted in static case

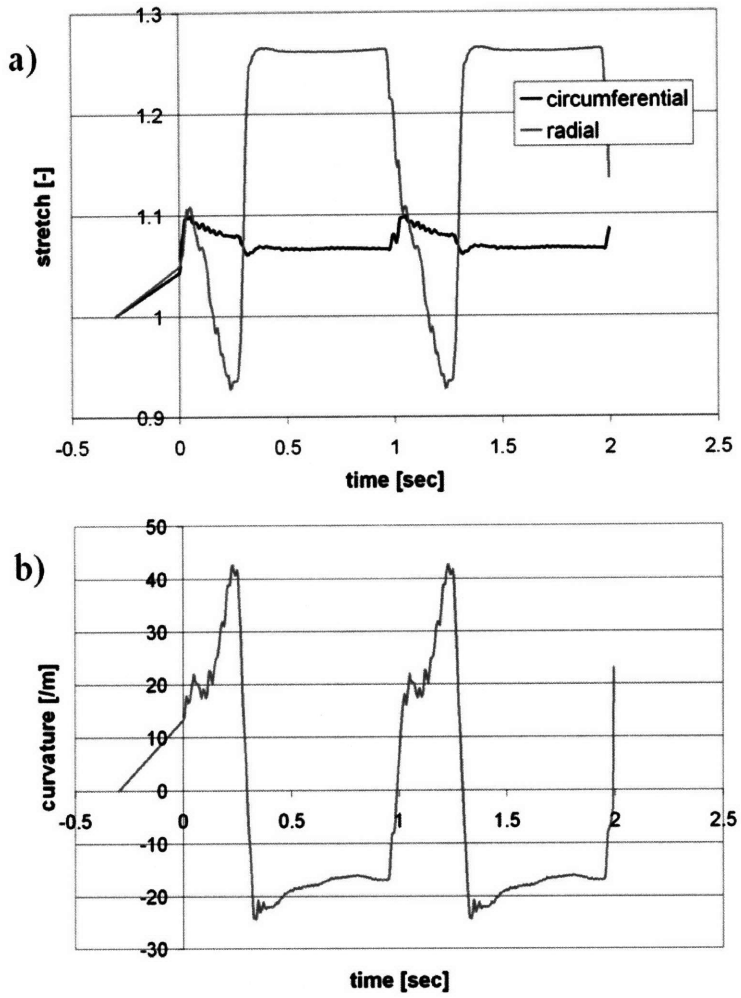


**Figure 2.15.** Element deformations predicted in dynamic case versus time: a) planar stretches b) curvature

*Tissue-level simulation*

All tissue-level simulations ran to convergence over a range of strains larger than is expected to be seen physiologically. Contour plots of the strain-energy surfaces for the fibrosa and ventricularis models are shown in Figure 2.16. For visualization of the wide variation in energies of these exponential functions, we have plotted $\log(W)$. Convexity was maintained in all tested cases. The responses of the fibrosa and ventricularis model to biaxial tension are plotted in

Figure 2.17. The predicted biaxial and bending behaviors of the complete tissue model compared to experimental[154, 160] are shown in Figure 2.18. We note a discrepancy in the experimental data for the circumferential direction between the individual layers (Figure 2.17)[160] and the assembled tissue (Figure 2.18)[13]: the assembled tissue is more extensible than the fibrosa in this direction. Hence, our model matches the data for individual layers well and underestimates the extensibility of the assembled tissue compared to this data set. The smaller value of the extensibility is consistent with stretches observed in the functioning valve[29, 30, 182].

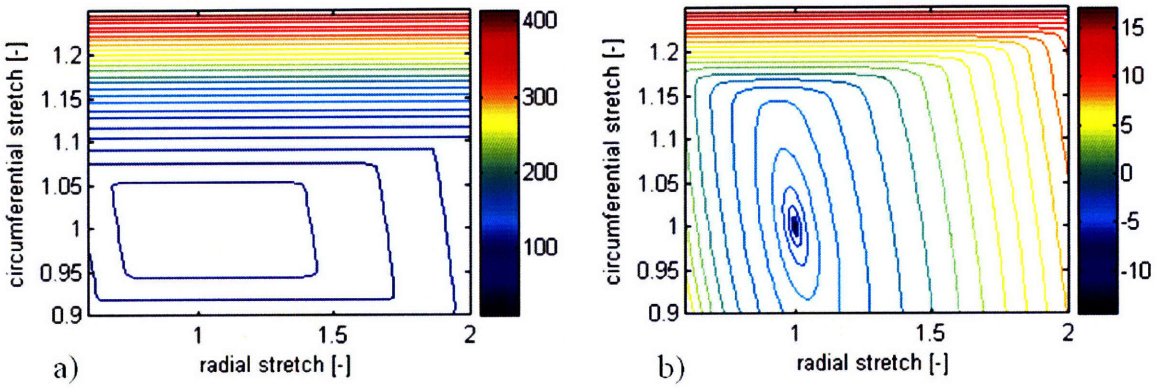


**Figure 2.16.** Contour plots of log($W$) for continuum model subjected to biaxial loading conditions: a) fibrosa model b) ventricularis model

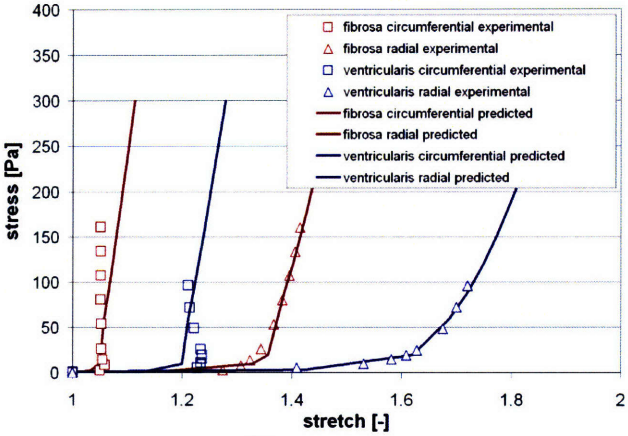


**Figure 2.17.** Predictions and experimental[160] data for biaxial tension of individual layers, referred to configuration $\Omega_0$

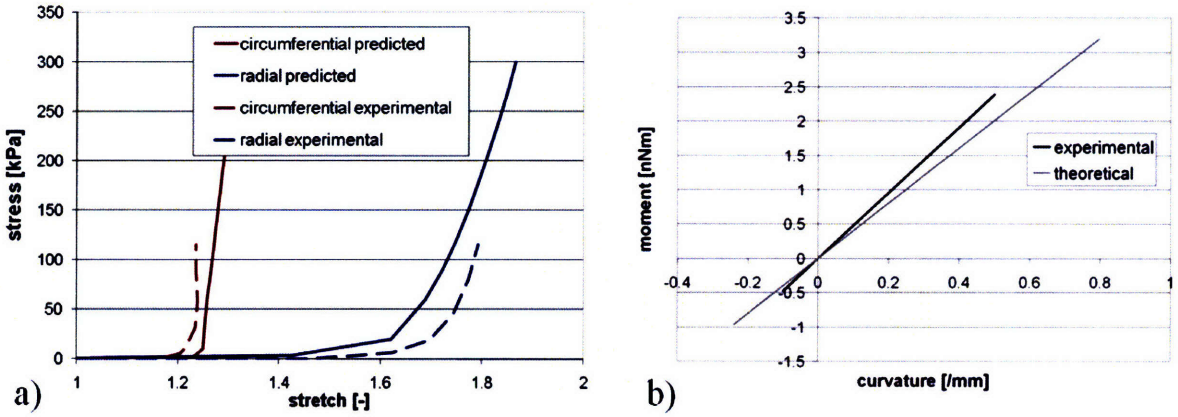


**Figure 2.18.** Continuum model predictions for the assembled tissue, referred to configuration $\Omega_1$, compared to experimental results[13, 154]: a) biaxial b) bending

Radial stretches due to assembly of the layers into a complete tissue (deforming from $\Omega_0$ to $\Omega_1$) are shown in Figure 2.19. Deformation states for the tissue model subject to strains measured in the organ-level model are shown at various times in Figure 2.10.B. Stretch magnitudes predicted in the static case are plotted in Figure 2.20. Stretches recorded in the tissue model for the dynamic case are plotted versus time in Figure 2.21.

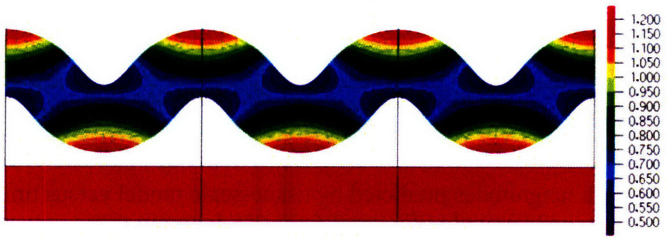

**Figure 2.19.** Radial stretches due to assembling layers into complete tissue.

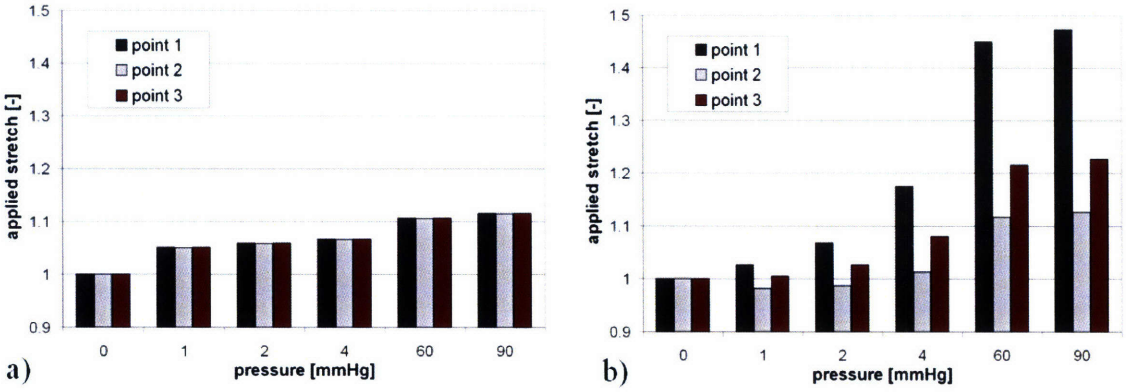


**Figure 2.20.** Stretch magnitudes predicted by tissue-scale model for static case: a) circumferential b) radial

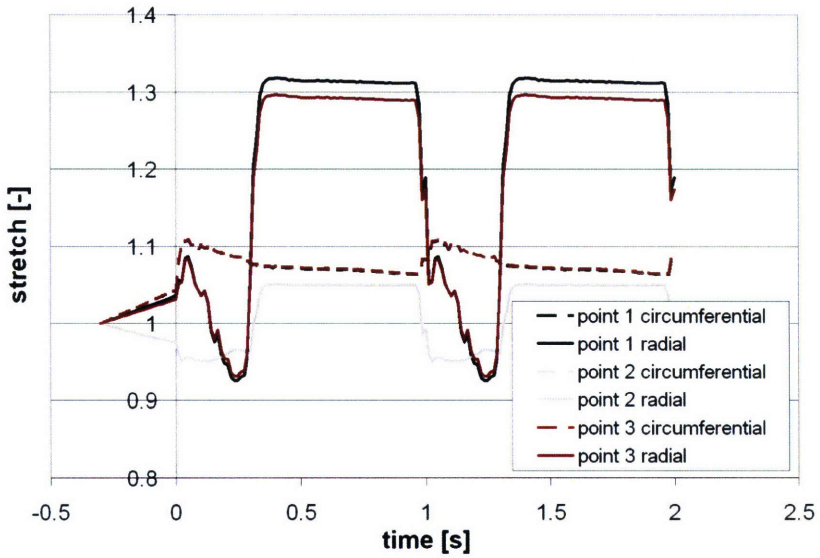


**Figure 2.21.** Stretch magnitudes predicted by tissue-scale model versus time at location B illustrated in Figure 2.6 for the dynamic case

*Cell-level simulation*

All cell-level simulations ran to convergence. Deformation states for selected locations at various times in the cycle are illustrated in Figure 2.10.C. In Figure 2.22, cellular aspect ratios predicted

for the static case are compared to measurements[93] made under static pressure. Values at points 1, 2, and 3 are plotted. The experimental data is an average over the leaflet, so we have also plotted the average over points 1, 2, and 3. The variation in CAR through the leaflet thickness and with varying pressure is compared to experimental data[93] in Figure 2.23. In both comparisons, the predictions closely match the experimental data. In the dynamic case, we have computed the time-varying aspect ratios for the three points tracked in the tissue-scale simulation at the three locations tracked in the organ-scale simulation for a total of 9 points. To give a typical response, we have averaged together the cellular aspect ratios for point 1 (see

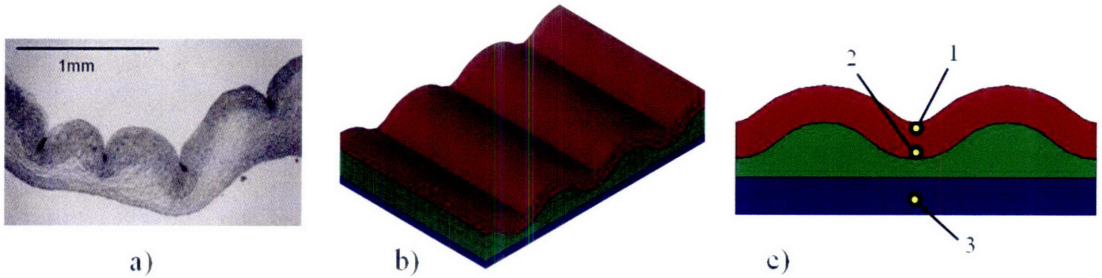


Figure **2.7**.C) of locations A, B, and C (see Figure 2.6). We have done the same for points 2 and 3. The results are plotted in Figure 2.24.

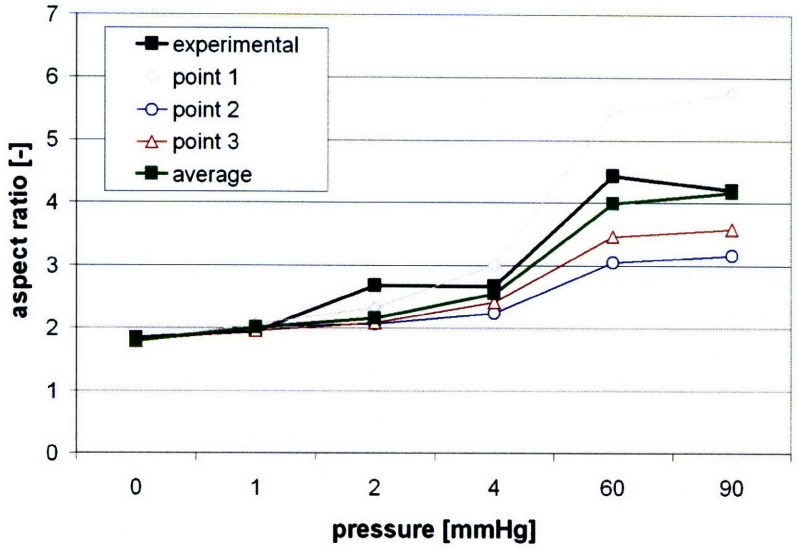


**Figure 2.22.** Predicted cellular aspect ratios compared to experimental measurements[93] for the static case

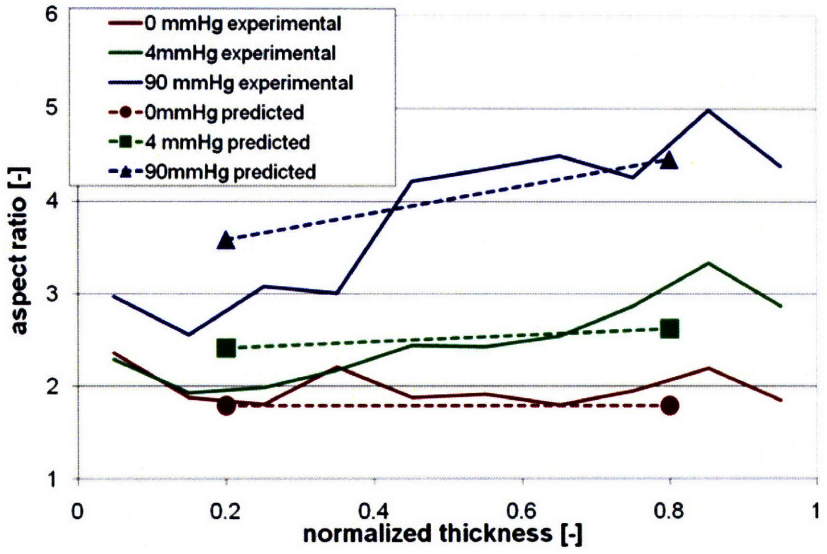


**Figure 2.23.** Predicted distribution of cellular aspect ratios through leaflet thickness compared to experimental measurements[93] for the static case. Normalized thickness varies from the ventricularis surface at 0 to the fibrosa surface at 1.

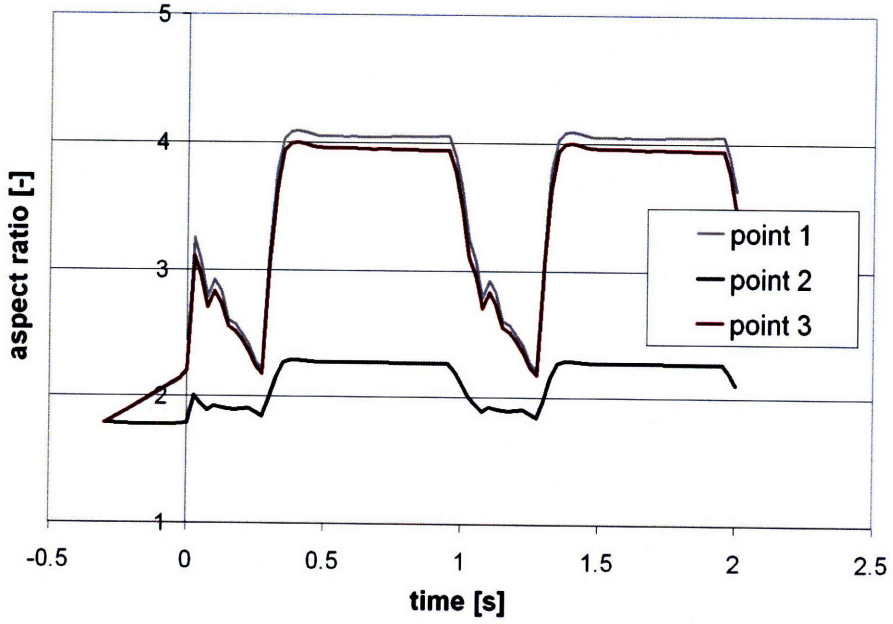


**Figure 2.24.** Predicted cellular aspect ratios for the dynamic case, averaged over organ-scale locations A, B, and C

## Discussion

*Organ-level simulation*

A number of assumptions were made to simplify analysis of the valve motion. First, a 1/6 symmetry was assumed for the valve. In reality, there is at least a difference between the coronary and non-coronary sinuses and cusps. It has been shown that the asymmetry does create different strain states in leaflets of the same valve[81]. However, these differences are small relative to the large displacements and strains that take place in the valve. The experiments to which we have compared our predictions generally do not note a difference between leaflets[179], hence the effects of asymmetry are finer than the current work can resolve. A coarse mesh was

used, particularly in the fluid phase, to decrease computation time. Prediction of finer features of the fluid and shears within thin boundary layers would require a refined mesh.

Equally important simplifications were made in the choice of material model used. We assumed that both the leaflet and wall materials are homogenous and that the leaflet fiber directions can be represented simply by two fiber families. Both the leaflet[158] and wall[110] have been shown to be in inhomogeneous, and the leaflet fiber distribution varies throughout the leaflet and changes as the tissue deforms[158]. There does not currently exist, however, a complete map of material properties to the valve geometry. For example, the leaflet material properties have been accurately measured in-vitro[13], but the effects of physical preloads and cellular contraction[122] in-vivo are undetermined. The discrete-fiber model simulates the main features that we currently understand to be important to the tissue bulk deformation.

Other simplifications include our smooth CAD representation of a complex biological geometry, representation of the ventricular contraction as a simple displacement condition, and lack of tissue surrounding the aortic root. The organ-scale model is clearly an idealization of the physical case. Comparison of the model to experimental data for both the fluid and solid domains shows that the model capably represents the valve motion in both domains.

*Tissue-level simulation*

The purpose of the tissue-level simulation is to translate deformations from the organ scale to the cell scale. Since the AV cusp tissue is multilayered and undulated, the tissue model must also

have those characteristics in order to accurately predict the cell-level deformations. While the bulk properties of the tissue have been widely reported, the details of the interplay between layers and motion of the undulations in the fibrosa as the tissue deforms are not known. Our tissue model simulates the major bulk behaviors of each layer and of the complete tissue but the local behaviors are, at this time, speculative. Experimental investigation into the local deformations of the AV tissue could be used to verify this work. Currently, the tissue model accurately represents bulk tissue behavior and approximates local behavior to the highest resolution possible given available knowledge.

*Cell-level simulation*

Our model of the mechanics of ICs in the leaflets is highly simplified. Both the matrix and cell are modeled as homogenous solids. Actually, the fibrous nature of the matrix is evident at the cell scale and the cell has multiple solid and fluid components. The features of the matrix and cell have not been determined beyond what we have included in our model, though. Given the series of assumptions made across the simulations, the predictive ability of the cell-level simulation demonstrated in the static case is remarkable. Our model predicts both the trend and magnitude of change in CAR with pressure as well as the variation across the leaflet thickness. These results give a high degree of confidence in the predictions for the dynamic case.

## Conclusions

We have created three models for AV mechanics, one at each of the cell, tissue, and organ length scales. The individual models capture the major known mechanical aspects at their respective scales. We have demonstrated that each model is numerically functional and satisfactorily matches experimental data. Each model represents a significantly simplified version of the physical AV, and they all can be refined by coordinating with further experimental work.

We have introduced a coherent set of reference configurations to link the three models so as to create one multiscale simulation of the complete mechanics and motion of the AV. We have verified our multiscale model in the static case, which simulates a multiscale experiment that has been previously performed. In this case, the input to the model is made at the organ scale (pressure boundary conditions). Deformations pass through the length scales and the output is observed at the cell scale (cell aspect ratios). We have demonstrated the ability of our approach to accurately handle the multiscale behavior in the static case, providing confidence in the predictions for the dynamic case.

Our multiscale model has application in studying both the healthy and diseased AV. In particular, the disease calcific aortic stenosis has a multiscale mechanical pathology. One of the causes of CAS is understood to be abnormal tissue strains giving rise to abnormal IC responses, leading to calcification. This process can be examined using the multiscale model we have presented. The effect of the disease is a stiffening of the matrix material, and our model can simulate stiffening at all three length scales. We expect that multiscale simulation of the AV will be a valuable tool to be used alongside experimental work to better understand AV health and disease.

# Chapter 3. A computational model of aging and calcification in the aortic heart valve

## Introduction

The aortic valve (AV) physically changes over time in all patients. Normally, this aging is restricted to a thickening[161] and loss of extensibility[39], which lead to slightly impaired valve function as the patient ages. In addition to the normal changes, the valve may change due to pathological processes. The most common disease of the AV is calcific aortic stenosis (CAS), found in 2% of individuals over 65 years and 4% over 85[42]. Early atherosclerosis-like lesions are found in almost all adults[108]. In CAS, these lesions develop first into small calcified nodes. The nodes grow over time, radically stiffening the valve leaflets. Stiffening hampers both the AV's ability to open in systole and close in diastole. CAS is the leading cause of valve replacement, accounting for a majority of the approximately 300,000 valve replacement surgeries worldwide each year[197].

Overall valve function is driven by changes of at the tissue level: stiffer, thicker tissue causes the valve to be less efficient. Beyond increasing the general understanding of valve function, there are two ways in which a model that describes the connection between tissue properties and valve function will be clinically useful. First, such a model can be used in conjunction with existing imaging techniques to improve diagnostic criteria and to aid in making decisions regarding timing of existing surgical therapies. Second, a model can be used to quantify the effects and aid

in the design of treatments aimed at preventing CAS onset and delaying valve failure once CAS is present.

Currently, the most common treatment for CAS is to replace the entire natural valve with a transplanted, mechanical, or bioprosthetic valve. Timing of this procedure is critical[1, 196]. A diseased valve must be replaced before full failure, but replacement valves have their own drawbacks and should not be implanted too early[1, 133, 135, 136]. Main drawbacks are that tissue valves can wear out and require re-surgery, and mechanical valves require the patient to be on anti-coagulation therapy[1, 136, 165]. Methods presently used in decision-making for valve surgery involve examination both of the valve function and the state of the tissue. Valve function is evaluated by using chest imaging to measure various properties of blood flow[4, 5, 60, 69] and various geometric parameters of the valve[11, 21, 183]. Calcification is examined by cardiac catheter[21, 141] or , more recently, chest imaging[104]. A model that incorporates both valve function and tissue health could aid in predicting the course of disease and in deciding when to intervene.

In addition to aiding decision-making regarding existing procedures, a model of calcific disease can be useful in examining and designing emerging methods. Since the loss of valve function is due to tissue dysfunction, treatments to prevent or slow disease progression must target the tissue. Current options are for preventing the onset of CAS or valve failure are limited. Pharmaceutical approaches do show promise in slowing the progression of CAS: in particular, statins have been shown to do so in patient studies[150]. Balloon valvuloplasty is a surgical option, where a balloon catheter is used to break up mild calcification, relieving stenosis. The valve normally becomes restenosed, however, within a year, and balloon valvuloplasty is not generally

recommended[21]. A better understanding of the tissue-based nature of CAS progression will enhance our ability to develop new pharmaceutical and surgical treatments.

In this chapter, we create a model for valve aging which describes the impact of changes to tissue properties on valve function. In the previous chapter, we described a simulation of the healthy aortic valve spanning the cell, tissue, and organ length scales[193], where we modeled the valve at one adult age. In the present chapter, we extend the simulation to model the effects of aging over the range of ages from 0 to 80. This collection of simulations yields a model of aging in the aortic valve multiscale in both length and time, including calcification, over an individual's entire lifetime.

**Methods**

We have previously described methods for using finite-element simulations to model the mechanical behavior of the normal aortic valve[193] and bicuspid aortic valve[190] over the cell, tissue, and organ length scales. These simulations have modeled the valve at one age in adulthood. In this paper, we extend our model of AV organ-scale mechanics to describe the transient effects of aging on the valve.

Here we briefly describe the method for modeling a healthy adult valve. Details on the development and validation of this model can be found in[193]. Valve geometry was created in SolidWorks (SolidWorks, Concord, MA). Dimensions of the overall valve structure[179] and thicknesses at various locations[79] were taken from literature. The geometry was meshed with brick elements using TrueGrid (XYZ Scientific Applications, Inc., Livermore, CA) and

modified, including the addition of cable elements, using HyperMesh (Altair Engineering, Troy, MI). The cable elements are part of the discrete fiber model we developed[193] to model the highly nonlinear, anisotropic material behavior of the leaflets in a computationally efficient manner. Sinuses were modeled as isotropic and rubber-like, and blood was modeled as a simple Newtonian fluid. Dynamic pressure boundary conditions, representing the pressures in the left ventricle and aorta entrance, were applied to the blood at the valve orifices. A dynamic displacement boundary condition was applied to the ventricular orifice to represent ventricular contraction. The simulation was run in LS-DYNA (LSTC, Livermore, CA), which readily accepts large displacements of the solid through the fluid utilizing an operator-splitting algorithm[84]. Models were post-processed in HyperView (Altair Engineering, Troy, MI).

To simulate normal aging of the AV, individual simulations were created representing the valve at ages between 20 and 80 years at 10 year intervals. We are modeling the effects of aging on the adult valve, and have not included the ages from 0 to 20 where the young valve grows and remodels appreciably. Thicknesses were varied according to experimental data[161]. Thickening versus age data is shown in Figure 3.1.A and resulting CAD geometries of the valve at age 20 and 60 years are shown in Figure 3.1.B.

a)

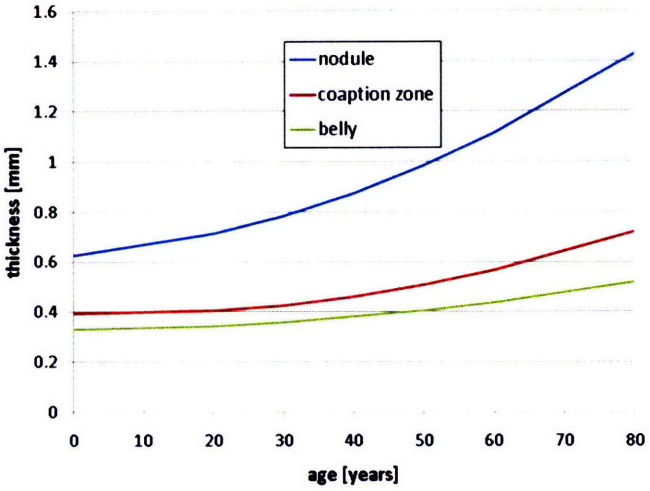


b)

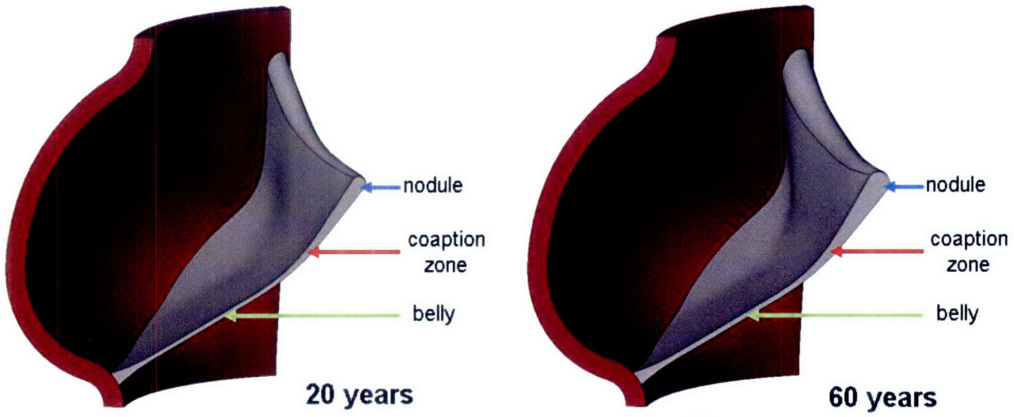


**Figure 3.1.** Changes in valve geometry with age. a) Measured thickness[161] and b) CAD geometry at ages 20 and 60 years

Material properties were also varied following experimental data. The only known data for leaflet stiffening versus age is that measured by Sahasakul[161], plotted in Figure 3.1.A. We have previously discussed at length the choice of extensibilities in our model for the healthy AV[193]. Here, we consider that model to represent age 20. For all other ages, we scale the extensibilities proportionally following the linear fit illustrated in Figure 3.2.A. In Figure 3.2.B, we plot the resulting radial and circumferential stress-strain curves at ages 20 and 60.

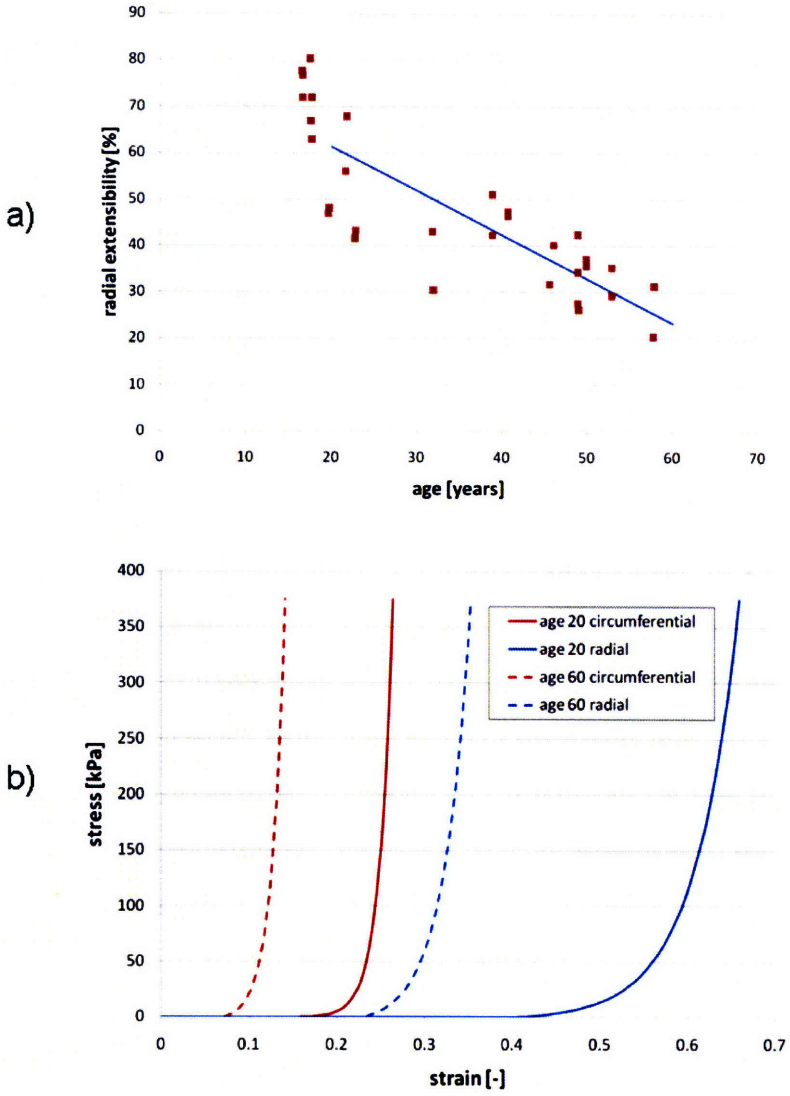


**Figure 3.2.** Changes in leaflet extensibility with age[39] a) Measured radial extensibility versus age and b) Circumferential and radial extensibilities used in model at ages 20 and 60

Progression of CAS in the AV was modeled by adding calcified zones to the valve. Initiation sites for calcification were defined at the regions of high flexure according to observations of explanted specimens, along the lines where the leaflet attaches to the sinus and where the free section of the leaflet meets the coapted section[182]. These initial locations are shown in Figure 3.3.

In the model, these calcified zones were modeled with stiff shell elements on the aortic-facing surface of the valve. Our current disease progression model depends on two parameters. The first is the age of onset, at which calcified zones are first added to the model. Second, we assume a simple growth law for the nodes: the boundary is allowed to spread outward at a constant speed. This speed, the growth rate, is the other parameter. We ran our model with onset ages from 40 to 70 years and growth rates from 0.25 mm/year to 1.0 mm/year.

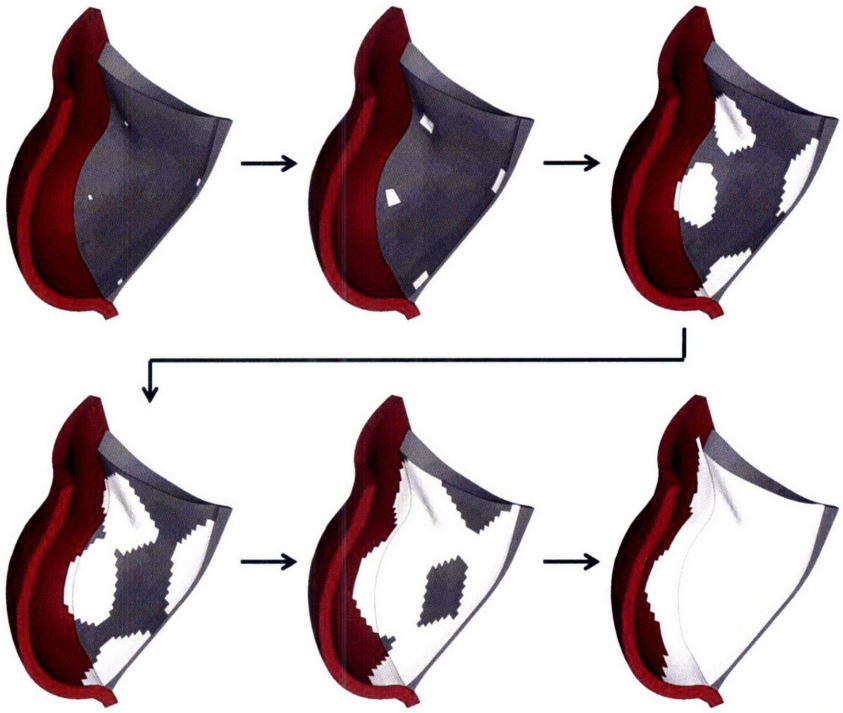

**Figure 3.3.** Simulated growth of calcified nodes

The percentage of the total leaflet area that is covered by calcification is plotted versus time in Figure 3.4 given a constant growth rate of 1 mm/year. With the boundary moving at a constant speed, the calcified area increases quadratically before saturating when the whole leaflet is covered. For each age of onset, the valve was simulated with each rate once for every year until the model valve was entirely calcified.

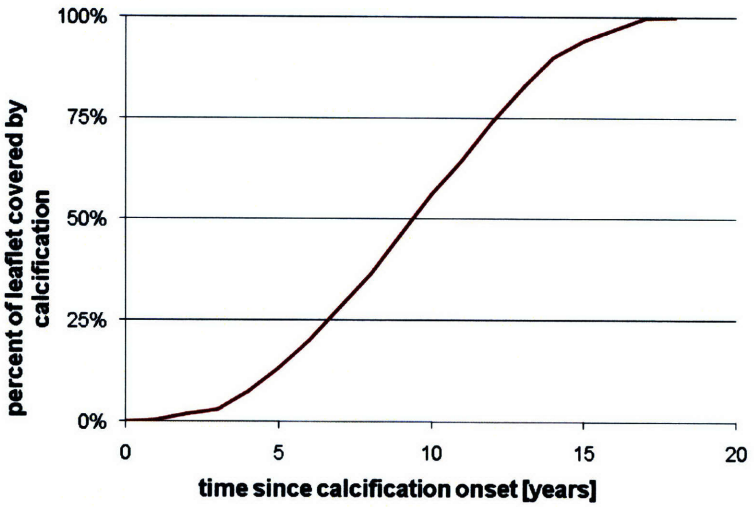


**Figure 3.4.** Percent of leaflet covered by calcification versus time

A number of measures of overall valve function and progression of valvular disease have been suggested, including peak fluid velocity, pressure drop across valve, effective orifice area, valve resistance[5, 17, 69], energy loss[75], rate of change in valve area[112], and others[11, 183]. To track the overall valve function over time in our simulations, we calculate the peak fluid velocity and aortic valve opening area (AVA) at each age. These measures were chosen because they are recognized clinically and straightforward to measure both in the clinic and simulation. Additionally, the area is an intrinsic measure of valve function, relatively insensitive to varying boundary conditions[17]. The peak velocity for each simulation is simply the maximum fluid velocity in the simulated cardiac cycle. AVA for each simulation is the maximum value of the area calculated throughout the cardiac cycle using the Gorlin formula[77]. Simulation results were compared to experimental data for a typical case of valve aging with CAS. Piper *et al*, 2004 gives experimentally-derived functions for AVA versus age given the calcification state of the valve at one point in time[141]. We compared our predicted AVA to the experimentally-determined curve for a valve which is unobstructed until onset of calcification at age 50[141]. We also

compared our predicted peak velocities to a curve calculated from the experimental AVA by the Gorlin formula.

**Results**

All simulations ran to convergence with no instabilities. Computation time was approximately 3 hours per each cardiac cycle on a workstation with four Xeon 5160 3.00 GHz processors.

In both normal aging and calcification, overall valve function, measured by fluid peak velocity and valve orifice area, degraded over time. Results are shown graphically in Figure 3.5, where the computed geometries are shown at mid-diastole for a range of ages. At each age, a section view overlaid with fluid velocity vectors is shown and a view of the whole valve seen from the aortic orifice. These plots show qualitatively the valve orifice narrowing both in normal aging and CAS.

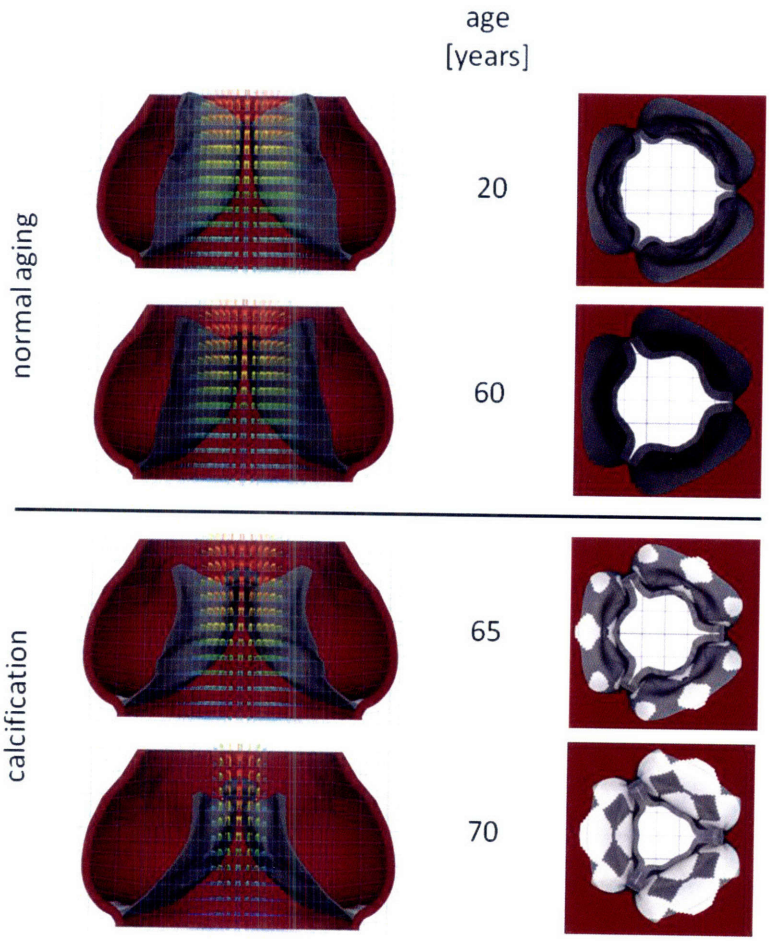


**Figure 3.5.** Computed geometries and flow velocities at mid-systole at various ages. Assumptions for calcification model are onset at age 50 and a growth rate of 1mm/year.

Computed peak velocities and areas for are compared to experimental data in Figure 3.6 and Figure 3.7, respectively. The theoretical curve in those figures has onset at 50 years and a range of growth rates. The experimental data is the typical curve for a patient where calcification appears at 50 years in a previously unobstructed valve[141]. The plots are overlaid with clinically accepted values for grading the severity of valve disease[135]. In both plots, the theoretical model tracks the experimental data best with lower growth rate in the years immediately after onset of calcification and with higher growth rate in the years after that.

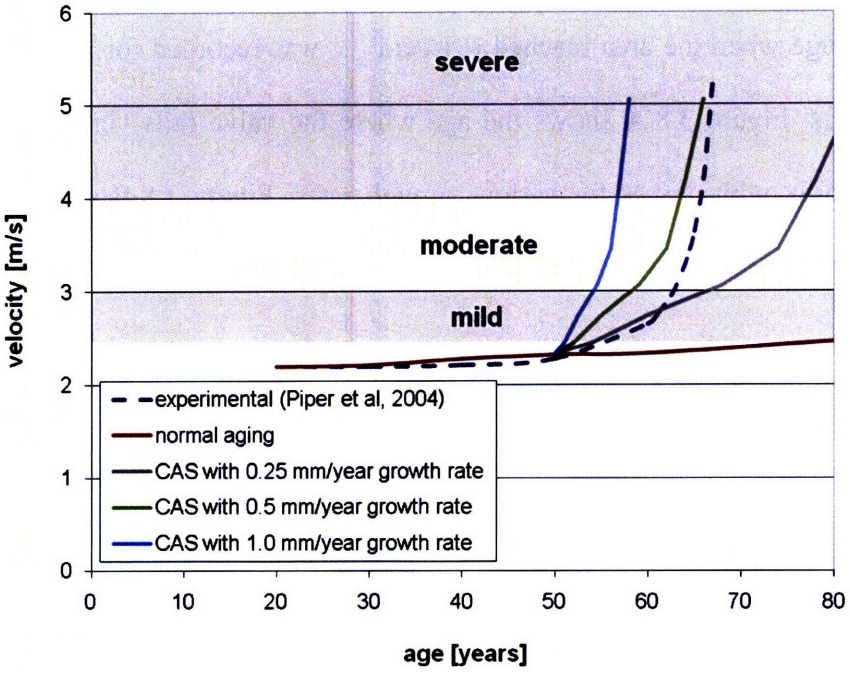


**Figure 3.6.** Peak velocity versus time for normal aging and with calcification

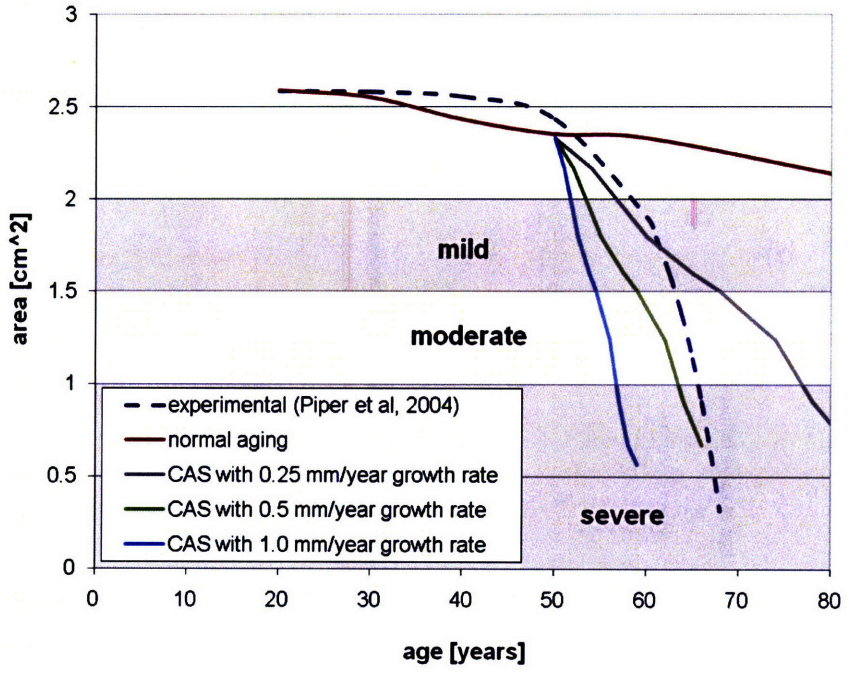


**Figure 3.7.** Valve effective area versus time for normal aging and with calcification

Sensitivity of the model to the two input parameters was analyzed. The age of valve failure, defined as the age when the area reached < 1.0cm$^2$ [21], was recorded for all combinations of the input parameters. Figure 3.8.A shows the age where the valve fails versus the defined age of calcification onset, with curves for various growth rates. Figure 3.8.B shows the age at valve failure versus growth rate, with various ages of onset.

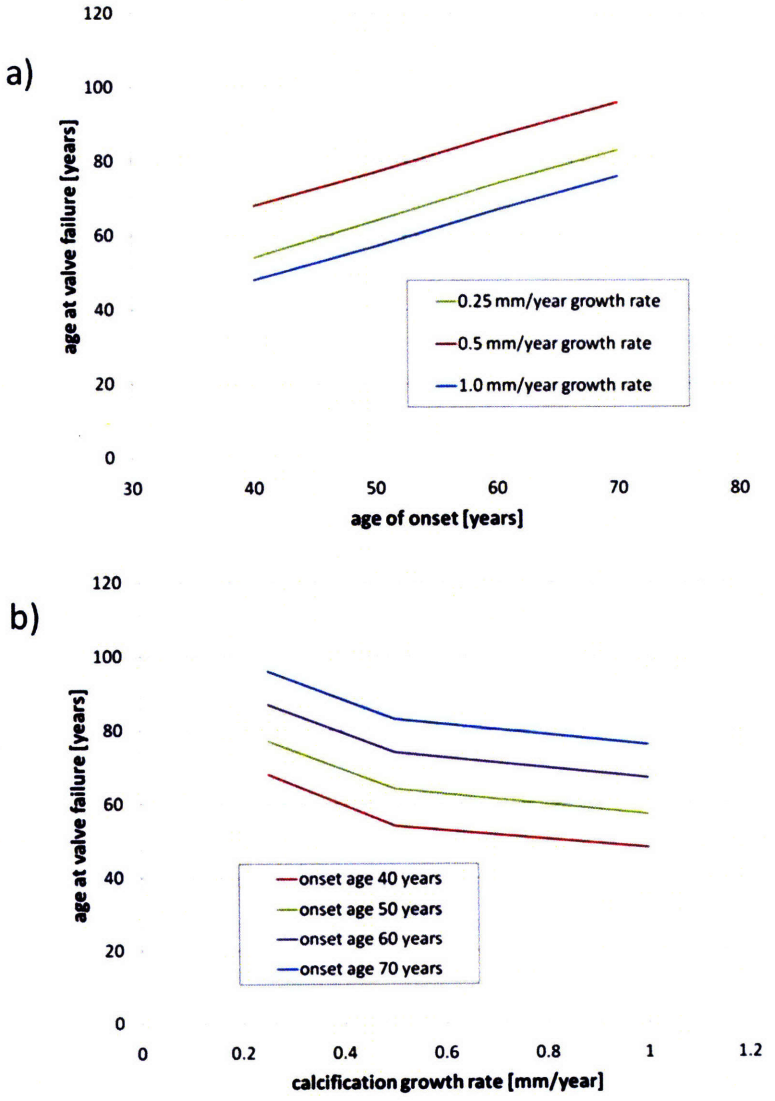

**Figure 3.8.** Sensitivity of model to input parameters: a) age where valve fails versus onset age, with various growth rates and b) age where valve fails versus growth rate, with various ages of onset

## Discussion

We have introduced a model for the mechanical effects of aging in the AV, including normal stiffening and thickening as well as progressive calcification. There are many approximations made in this model. First, a number of assumptions are made to construct a model of the valve at any point in time. These assumptions, which we have previously discussed in detail[193], include simplified representation of the geometry, modeling the interaction of the valve with its environment through pressure and displacement boundary conditions, and assumptions inherent to the material models: a discrete fiber model for the leaflet mechanics, simple Mooney-Rivlin for the sinus wall, and Newtonian flood for the blood.

Further assumptions were made to model the changes in the valve over time. In normal aging, the most significant source of error is our scaling of the leaflet extensibilities. Our model was extrapolated from the known data[39], which provides only the change in radial extensibility, and does not give reference to a no-stress state. Changes to the valve other than leaflet thickening and stiffening were not included in the model.

Calcification was modeled simply as the addition of stiff shell elements on the aortic surface. Calcification sites were assumed to appear simultaneously at different locations in the valve, where physiologically they arise at different times. The nodes were modeled as thin shells, though in CAS the calcifications are known to develop significant thickness.

Our current model assumes two input parameters, the age of calcification onset and the calcification growth rate. Sensitivity analysis shows that the model's ability to predict overall valve function, measured by when the model predicts valve failure will occur, is sensitive to both parameters.

Our model provides a framework for linking overall valve function to valve mechanical properties and geometry. This model qualitatively captures the valve narrowing and increase in fluid velocity seen in patients. With proper choice of input parameters, the model can approximate experimental data for disease progression. Determination of the values for those parameters, however, will require significant experimental work. If the age of onset and growth behavior, which likely does not follow the constant-rate model we have assumed, can be measured, then our model can be clinically useful. A model that can take patient inputs and predict the course of disease will be useful in deciding timing of valve replacement, and a model that can describe the effects of pharmaceutical and surgical interventions can aid in the development of those treatments. The model we have presented gives a theoretical basis for understanding the link between therapy and valve function in CAS, and being able to understand and predict the course of CAS has the potential for significant clinical impact.

# Chapter 4. A Multiscale Computational Comparison of the Bicuspid and Tricuspid Aortic Valves in Relation to Calcific Aortic Stenosis

## Introduction

The aortic valve opens to allow flow from the left ventricle to the aorta and closes to seal against backflow. This valve commonly has three cusps and three sinuses. In 1-2% of the population, however, the aortic valve has two cusps[65], a condition known as a bicuspid aortic valve (BAV). Illustrations of tricuspid and bicuspid valve geometries are shown in Figure 4.1.

Serious complications develop in at least 33% of patients with BAV[187]. The aortic valve is generally susceptible to stenosis, regurgitation, and infection while the aorta is susceptible to medial degeneration, dilation and aneurysm, and dissection[65]. Of these, regurgitation is clearly a product of the malformed geometry of the BAV. The cause of the other complications is unclear at this time. It is conceivable that any of these diseases is more likely in patients with BAV due simply to the geometric difference between having two cusps and sinuses instead of three. For example, studies have examined whether creasing of the BAV leaflets gives rise to calcific aortic stenosis (CAS)[149] and whether disrupted flow patterns in the BAV lead to aortic dilation[8, 147]. Alternatively, the valves may have different mechanical properties that cause a difference in function that eventually leads the BAV to be more susceptible to disease than the TAV. Another

possibility is that the structural differences between the TAV and BAV are not relevant to whether the BAV is more likely to develop disease. Instead, BAV may be caused by a genetic defect, and this same defect independently gives rise to the other diseases. Fibrillin-1 deficiency has been notably implicated[64].

Much progress has been made in creating numerical simulations of heart valves over a range of length scales. Fluid-structure interaction models for organ-scale heart valve motion have been developed[47, 57, 131, 193], allowing simultaneous prediction of the solid and fluid phases in the valve. At the tissue scale, many efforts have been made recently to formulate and implement appropriate experimentally-derived material constitutive models[160, 170, 191, 192]. Cell-scale simulations have also been created with linkage to experimental data[93]. In Chapter 2, we described a method for simulating mechanical behavior of the aortic valve across the range of length scales including cell, tissue, organ, and we verified the approach against experimental data for the normal tricuspid valve[193].

CAS progression is a multiscale process. Organ-scale stretches are translated to the tissue and cell scales, where dynamic deformations are imposed on the valvular interstitial cells (ICs). The ICs are thought to mediate the disease in response to these cellular deformations[117]. Our multiscale simulation tools allow us to examine the multiscale disease mechanisms. In this study, we perform a multiscale analysis of the TAV and BAV in order to determine whether the increased incidence of CAS in the BAV may be linked to a mechanical difference between the two types of valve.

## Methods

We described a method for multiscale simulation of the tricuspid aortic valve in Chapter 2[193]. Here, we briefly outline the multiscale simulation methods we employ to compare the BAV and TAV. For further details including verification of the model versus experimental data, see Chapter 2[193].

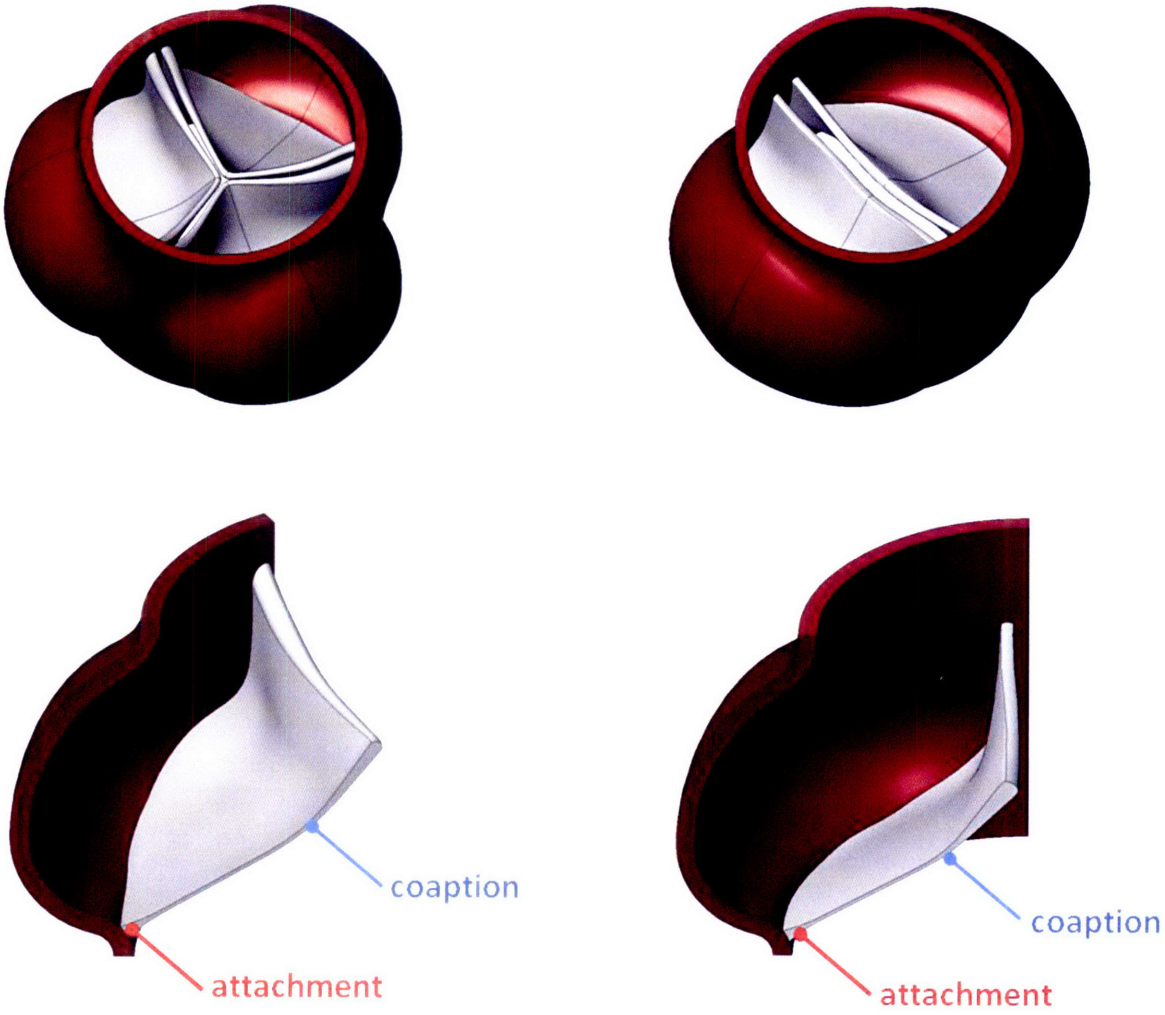

**Figure 4.1.** Organ-scale valve geometries, tricuspid on left and bicuspid on right. Top: full geometry of valve. Bottom: cutaways showing tracking locations.

An overall schematic of this approach is shown in Figure 4.2. Computed local deformations of the organ-scale model are projected as boundary conditions to the tissue-scale model. Similarly, local deformations of the tissue-scale model are mapped as boundary conditions to the cell-scale model.

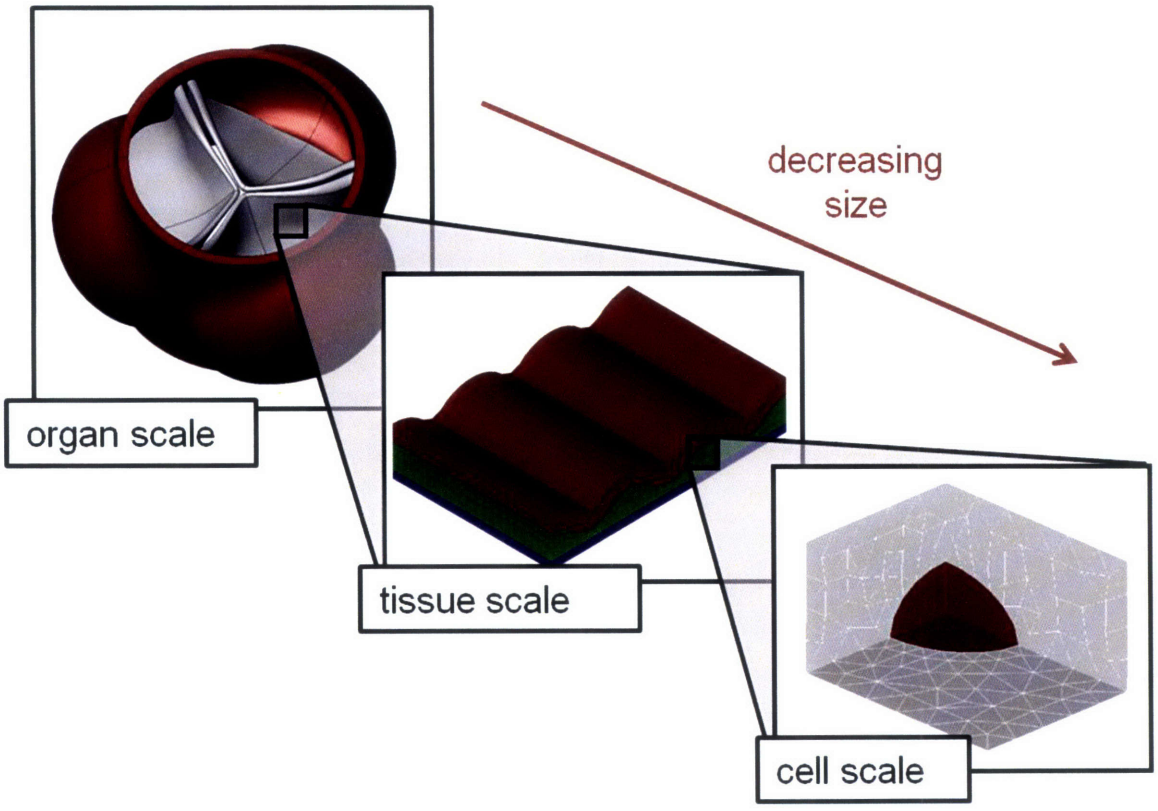


**Figure 4.2.** Schematic of multiscale simulation approach. Deformations are mapped from largest scale to smallest.

First, we defined a system of reference configurations to describe the valve tissue deformations. Our system extends that of Stella[170]. In $\Omega_0$, the ventricularis and fibrosa are unattached and stress-free. The layers are connected to form the assembled tissue $\Omega_1$. In $\Omega_2$, the tissue is in

position in a valve to which no pressure has been applied. When the valve is pressurized to its resting physiological state, the tissue is in $\Omega_3$. We denote the time-varying state of the tissue in the functioning valve as $\Omega_t$. Detailed illustration of these reference configurations can be found in[193].

The organ-scale simulation considers deformations from $\Omega_2$ through $\Omega_t$. The organ-level simulation was performed in LS-DYNA (LSTC, Livermore CA). This software was chosen because its operator-splitting method for fluid-structure interaction has been demonstrated to readily handle the motion of a solid through fluid typical of a functioning heart valve[84]. LS-DYNA is an explicit solver, which means it may require excessive computation times in modeling relatively low-speed physical systems such as the aortic valves. We addressed this issue in our formulation of the constitutive model used to describe the cusp tissue mechanics.

To simulate the cusp mechanics, we have developed a constitutive model that describes the bulk material behavior and is particularly computationally efficient in explicit finite element codes. Like many tissue constitutive models[14, 91, 173], our model treats the tissue as an isotropic solid with embedded aligned fibers. Instead of using a continuum model, though, we took a discrete approach. The solid mesh elements were modeled with an isotropic material. One-dimensional cable elements were then used to connect the nodes of the solid element. LS-DYNA allows assignment of arbitrary stress-strain curves to the cable elements, and fiber rotations follow nodal displacements. This approach achieves enormous computational gains over a continuum approach; for further details see Chapter 2[193].

The constitutive model was constructed referring to the tissue configuration $\Omega_2$. The isotropic solid was modeled as a single-term Mooney-Rivlin with the value $C_1$= 2.0e4 chosen to fit

bending data for the leaflet[93, 155]. The stress-strain curves in the radial and circumferential directions measured experimentally for configuration $\Omega_2$[160] were discretized and applied to the fiber elements. The aortic root was assumed to be isotropic and modeled with a single-term Mooney-Rivlin material. A value of $C_1$=1.0e5 was fit to experimental pressure-versus-dilation data for the root[110]. Further details on the development and validation of these models are outlined in Chapter 2[193].

Organ-scale geometry of the tricuspid and bicuspid valves were generated in SolidWorks (SolidWorks, Concord, MA). These solid geometries are shown in Figure 4.1. This figure also illustrates the locations where local deformations were monitored for translation to the tissue-scale model. The tracking locations were chosen at two regions expected to show the highest degree of flexure: where the leaflet attaches to the wall (labeled "attachment"), and the hinge point where the coapted surface of the leaflet meets the free portion (labeled "coaption"). The overall geometry of the leaflets and sinuses (heights, lengths, angles, and diameters) for explanted valves have been measured and described in literature[179]. Finer geometric features, including the thickness distribution at different locations on the leaflet, have also been measured[79]. Based on this collection of measurements, we created the valve geometry in SolidWorks in terms of two solid features: one loft for the sinus and one loft for the leaflet. In this way, the complete valve geometry is described by a small number of geometric variables and can readily be modified. Our CAD geometry represents the valve in the unstressed, unpressurized explanted state according to observations in our lab. For simplicity and to minimize computation time, the tricuspid valve is assumed to have 1/6 symmetry and the bicuspid is assumed to have 1/4 symmetry. The solid domain is embedded in a fluid domain

having the same symmetry. Entry regions were added at both ends of the valve to allow the sinus to move radially, and fluid source domains were added at the orifices of the entry regions. Parametric 8-node brick meshes of both the solid and fluid domains were created in TrueGrid (XYZ Scientific Applications, Inc., Livermore CA). Cable elements representing circumferential and radial fiber families were overlaid on the solid mesh using HyperMesh (Altair Engineering, Troy MI), following observed fiber directions[158].

Fixities and boundary conditions were applied to the mesh. Mirror conditions were applied to fluid and solid nodes on the two symmetry planes. The unattached ends of the entry regions were fixed while the nodes at the junction of the entry regions and the aortic root were constrained from moving axially. Outer faces of the fluid domain were not constrained. The same boundary conditions were applied to both the tricuspid and bicuspid models: experimentally-derived, time-varying pressure curves for the ventricle and aorta were applied to the appropriate fluid source domains[179]. An experimentally-derived radial displacement condition representing ventricular contraction was applied to the base of the valve. Pressures were slowly applied to bring the valve from its unpressurized state to its in-vivo resting position before the transient pressures were applied.

Post-processing was performed using HyperView (Altair Engineering, Troy MI). For both simulations, we recorded velocity profiles in the fluid phase and mechanical strains, displacements, and flexures in the solid phase throughout the solution.

Deformations from each organ-scale model were mapped as dynamic boundary conditions to tissue-scale models. Multilayered, undulated leaflet geometry was created in SolidWorks and meshed in ADINA (ADINA R&D, Watertown, MA). The geometry is illustrated in Figure 4.3.

An exponential, anisotropic constitutive model was developed and fit to experimental data[170] for each layer. The region of interest, where calcification is observed to develop[108, 135], in the tissue-scale simulation is the layer closest to the aortic-facing leaflet surface, the fibrosa. To examine cellular deformations in this region, we recorded stretches in two locations of tissue-scale model, noted in Figure 4.3. One location is on the outer edge of a curve in the fibrosa (labeled "outer"), and one location is on the opposing inner edge (labeled "inner").

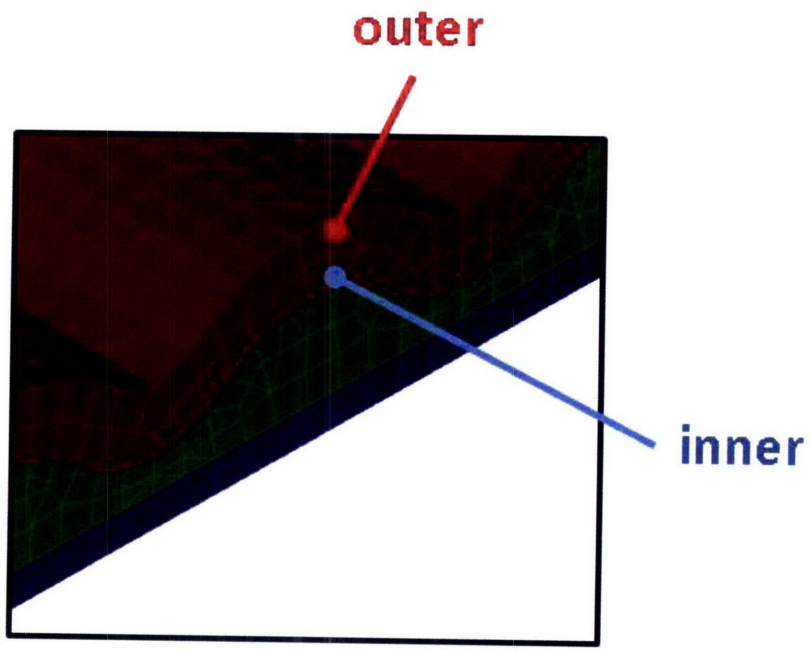


**Figure 4.3.** Locations to track in tissue-scale simulation

Stretch data recorded in the tissue-scale models were mapped as boundary conditions to the cell-scale models. The cell-scale model is comprised of a cell in matrix. Geometry, shown in the cell-scale portion of Figure 4.1, was created and meshed in ADINA. The cell was modeled by a single-term Mooney-Rivlin[93] and the matrix was modeled using the constitutive model

developed for the fibrosa in the tissue-scale model[193]. Cell aspect ratio (CAR) was recorded versus time for the tricuspid and bicuspid valve, and the results compared to each other.

**Results**

Multiscale simulations linking cell-, tissue-, and organ-scale models were run to convergence with no instabilities. Computation time for the organ scale models was approximately 3 hours for each cycle of opening and closing on a workstation with four Xeon 5160 3.00 GHz processors. Computation time for the cell and tissue models was a few minutes per cardiac cycle.

For the organ-scale model, deformed configurations of the TAV and BAV valves are illustrated at different times in Figure 4.4 and flow fields at mid-systole are shown in Figure 4.5. Overall dynamics of the tricuspid and bicuspid valves are similar. Since we defined the material properties, especially the extensibilities, to be the same in the leaflets and wall of the two valves, the leaflet strains and wall displacements had similar magnitudes and temporal trends.

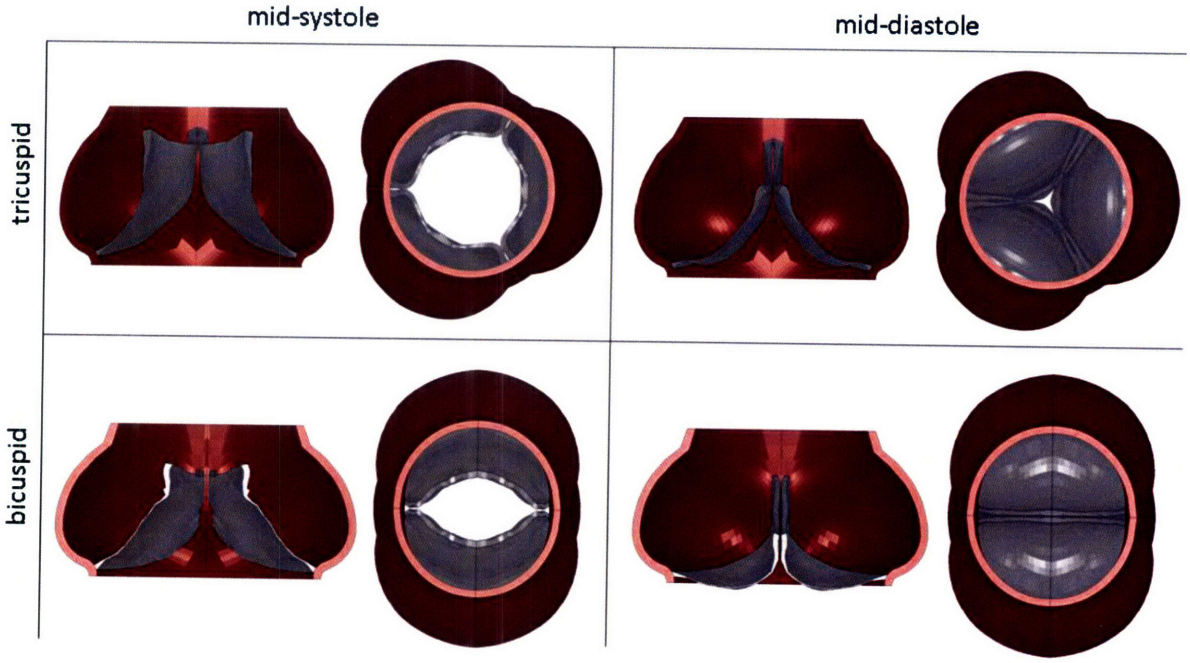


**Figure 4.4.** Predicted geometries of TAV and BAV at mid-systole and mid-diastole

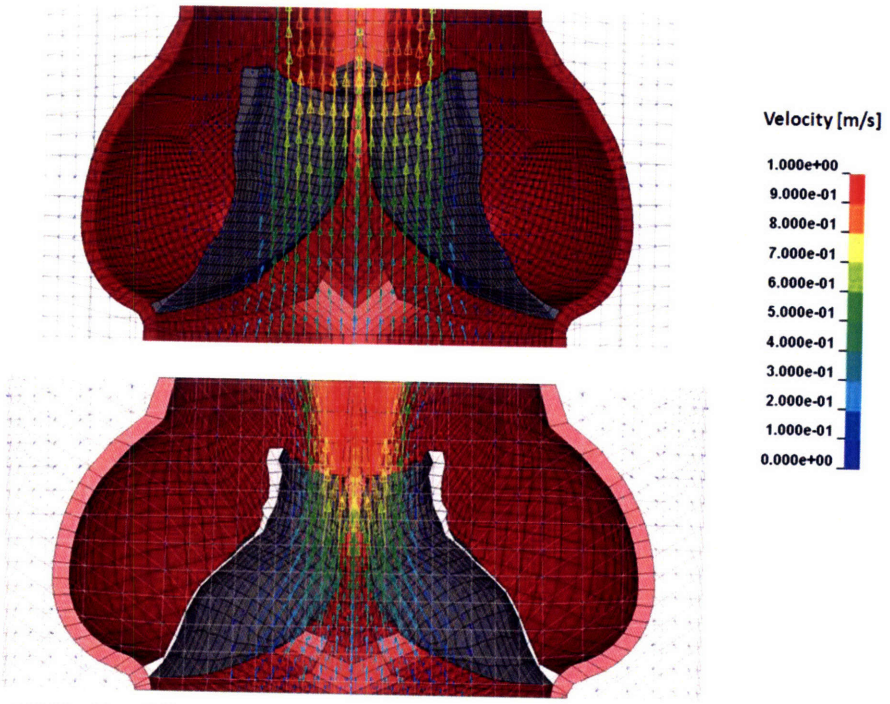


**Figure 4.5.** Predicted flow fields in tricuspid (top) and bicuspid (bottom) valves at mid-systole

Two main differences were observed between the tricuspid and bicuspid valves. First, the bicuspid valve did not open fully, creating a jet in the fluid not seen in the tricuspid valve. Comparative velocity profiles at the aorta entrance are plotted in Figure 4.6. Second, kinks formed in the bicuspid valve leaflet when open, whereas the tricuspid valve leaflets opened in smooth curves. This effect is reflected in Figure 4.7. In that figure, we have plotted the time-varying leaflet flexures in each valve measured at two points: where the leaflet attaches to the wall and where the coaption region begins. At each position, the bicuspid valve undergoes flexures of significantly greater magnitude than the tricuspid valve.

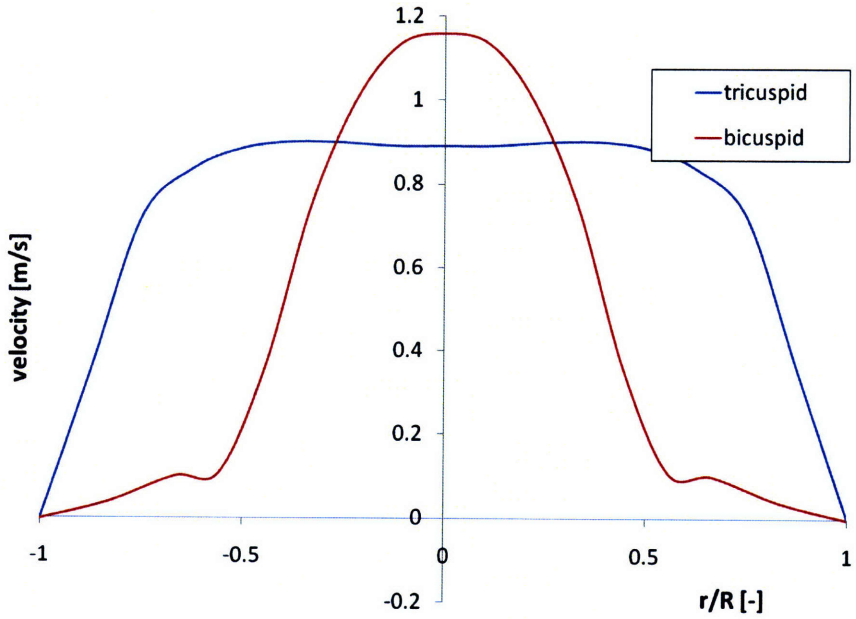


**Figure 4.6.** Fluid velocity profiles at entrance to aorta in tricuspid and bicuspid valves

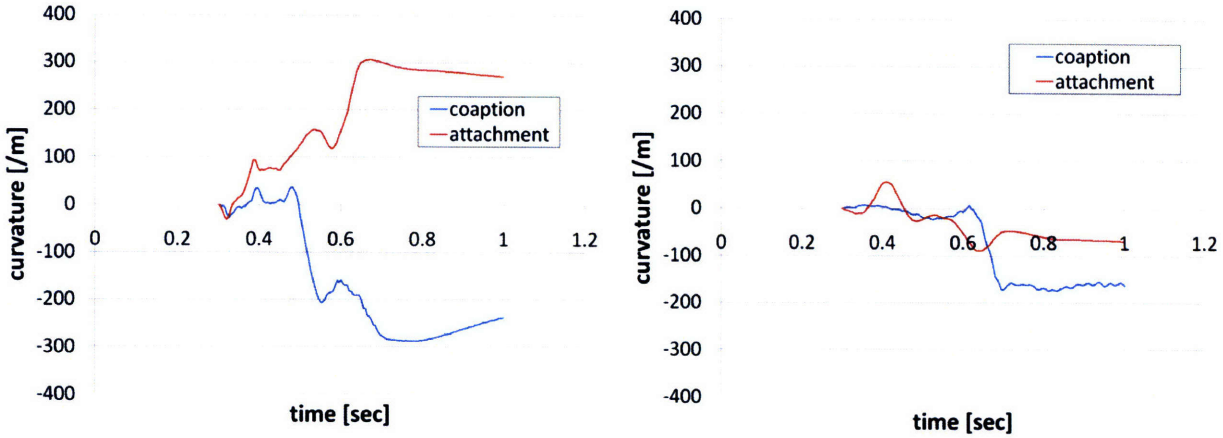


**Figure 4.7.** Dynamic flexures in bicuspid (left) and tricuspid (right) valves

Deformations occurring at the cell level associated with the organ-scale deformations described above are plotted in Figure 4.8. In the region of interest (points marked in Figure 4.3) dynamic CARs are very similar between the BAV and TAV.

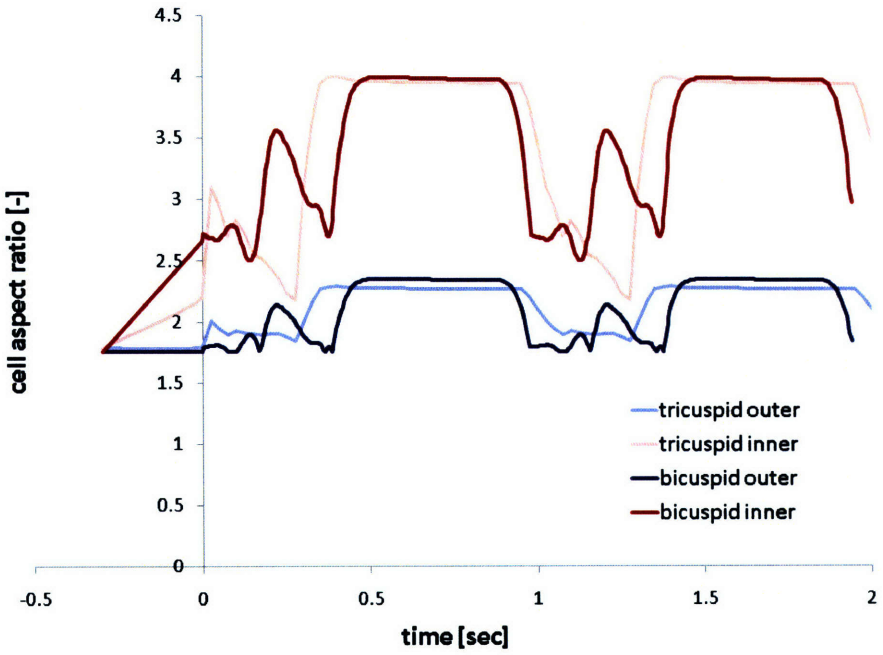


**Figure 4.8.** Dynamic cell aspect ratios for TAV and BAV

## Discussion

We have created multiscale simulations of the TAV and BAV, where the only difference between the two simulations is the number of cusps. At the organ-scale, this geometric variation causes two major differences in function. Firstly, the leaflets of the bicuspid valve do not open as smoothly and undergo more flexure relative to the normal tricuspid valve. Secondly, the bicuspid valve does not open as widely and the blood passing through the valve at systole forms a jet. Both differences in organ-scale behavior agree with experimental observations[113, 148].

For both the TAV and BAV, deformations were mapped to the tissue and cell length scales. At the cell scale, we examined cellular deformations in the region associated with CAS. Interestingly, no appreciable differences were found in cellular deformations at the CAS-relevant regions. We observed that the wrinkled structure of the fibrosa serves to shield the cells within from strain. Thus, while greater deformations were seen in the bicuspid valve at the organ scale, we found that these differences did not translate down to the cell level.

Since valvular interstitial cells can only sense the cell-scale deformations, our model predicts that these cells experience similar mechanical stimuli in the TAV and BAV regardless of organ-scale differences. Thus, our results suggest that the observed difference in calcification between the TAV and BAV is not due to a difference in mechanical deformation. The difference in calcification may instead be due a genetic difference which both determines the number of leaflets and the calcification risk. Evidence is mounting for a genetic cause of BAV[43, 59], and that this genetic difference gives rise to a difference in the matrix constituents throughout the valve

[64]. The fact that the BAV is more prone to a number of tissue diseases, including aortic dilation and aortic dissection, further suggests that the BAV is accompanied by dysfunctional tissue structure[52, 113, 134]. There remains the possibility that this difference in biochemical tissue structure between the BAV and TAV causes a difference in mechanical behavior, which then leads to deformations of the BAV that in turn lead to increased incidence of CAS. This effect could be investigated using our model if data on the mechanical properties of BAV were available. Currently they are not. Unless the BAV fibrosa structure is greatly different from that of the TAV, we would still expect to observe the strain-shielding effect on the cellular deformations in the region of interest that we found in the current study.

In this paper, we analyzed the mechanical differences between the tricuspid and bicuspid aortic valves over a range of length scales. We showed that cellular deformations in the region associated with CAS are not significantly different between the two valves. This result suggests that the difference in calcification risk between the two valves is not due to differences in deformation, and may instead be due to the genetic difference in matrix components.

# Chapter 5. Hemodynamic environments from opposing sides of human aortic valve leaflets evoke distinct endothelial phenotypes

## Introduction

Calcific aortic stenosis (CAS) is the most common heart valve disease in the western world[42]. Early lesions are prevalent in adults of all age groups[108], with early calcific sclerosis present in 20-30% of individuals over 65 years and 48% of those over 85 years[42, 132]. In CAS, these lesions form large calcific nodules which can severely impair valve function. Clinically significant stenosis affects 2% of individuals over 65 years and 4% over 85[42]. The first stage of CAS, aortic valve sclerosis, is characterized by the appearance of lesions similar in some respects to those of atherosclerosis[108, 138]. Both the initial lesions and calcified nodules develop predominantly in the fibrosa, the collagenous layer of the valve leaflet below the aortic-facing surface[108, 135, 179]. The initial calcific lesions are nucleated in the valvular interstitial cells (IC)[102, 103]. CAS is likely potentiated by the effects of biomechanical forces acting on the valvular endothelial cells (EC) and/or the IC, but it remains unknown how each cell type is affected and whether the key disease-inducing forces are solid deformations[149], hemodynamic shear forces[24], or a combination of the two. Our recent efforts have used computational models to demonstrate the uncertainty of linking cell-scale deformations to CAS processes[190]. In that work, we investigated the multiscale mechanical deformations in the normal (tricuspid) aortic valve and the bicuspid aortic valve. We showed that, while organ-scale deformations were different between the tricuspid and bicuspid valve, differences in cell-scale deformations were small and could not

explain the difference in calcification between the two valves. In this chapter, we use numerical models, in combination with *in vitro* cellular approaches and *in vivo* gene expression, to generate side-specific aortic valve hemodynamic waveforms and investigate the link between these specific waveforms and the endothelial phenotypes they evoke.

It is well established that hemodynamic forces acting along the endothelium differ between the two sides of the aortic valve leaflet[55, 194], leading some to hypothesize that the side-specific nature of CAS may arise from flow-mediated differences in aortic valve endothelial cell phenotypes. In support of this hypothesis, studies from explanted porcine aortic valves and cultured porcine aortic valve endothelial cells have demonstrated that the two sides of the leaflet display marked differences in expression of genes specific to vasorelaxation, inflammation, and bone-deposition processes, including C-natriuretic peptide (CNP) and bone morphogenic protein 4 (BMP-4)[25, 167]. The goal of the study reported in this paper is to investigate the effect of aortic valve side-specific hemodynamic waveforms on EC phenotype using physiologically relevant waveforms. We hypothesize that the different pattern of shear stress on the two sides of the aortic valve cusp generates a CAS-vulnerable EC phenotype on the distal/outflow side and a CAS-protective EC phenotype on the proximal/inflow side. Generating a reliable experimental measurement of the dynamic shear profiles in the valve, however, has proven difficult to-date. Different researchers have reported a wide range of peak shear stresses, ranging from 29-1200 dynes/cm$^2$ [55, 194]. We created a computational model to calculate the transient shear stress waveforms that act on each side of the aortic valve. We then applied the computed shear stress waveforms from both the aorta and ventricle-facing leaflet surfaces to cultured human endothelial cells and measured differences in endothelial genes that have previously been

correlated with vascular inflammation and atherogenesis. Among these genes, we assessed the expression of the endothelial transcription factor Kruppel-like factor 2 (KLF2), a gene that we and others have shown act as an integrator of the endothelial atheroprotective phenotype[45, 50, 74, 140]. In addition, the expression of KLF2 was documented in tissue using *in situ* hybridization in mouse aortic valve tissue. Our results describe a connection between the shear stress experienced by aortic valve endothelium and endothelial gene expression and function that may play a role in the mechanism of aortic stenosis.

## Materials and Methods

### *Computational Model*

To accurately calculate the shear waveforms applied to each side of the aortic valve leaflet, we created a 2-dimensional fluid-structure numerical simulation of the human aortic valve. This model is a simplified version of the 3-dimensional simulation we have described in previous chapters[193], but with high resolution on the fluid boundary to accurately resolve the wall shear stress patterns. Our previous model uses the operator-split method to handle fluid-structure interactions, where the deforming solid passes through a stationary fluid mesh. With operator-split, accurate calculation of the momentum boundary layers requires high resolution throughout the fluid mesh, and thus high computational cost. In order to resolve the momentum boundary layers and accurately compute the shear stress applied to the valve surfaces, we modified the previous model by employing the Arbitrary Lagrangian-Eulerian (ALE) method. With ALE, a

fine fluid mesh remains attached to the solid boundaries while mesh in the bulk can be coarser. Geometries of the solid and fluid were created in SolidWorks (SolidWorks, Concord, MA) based on experimental measurements of overall valve geometry[179] and of thickness at various locations on the cusp[79]. The full 3-dimensional geometry is shown in Figure 5.1.A, with a cutaway showing a plane of symmetry along the center of a leaflet. The solid and fluid geometry in that plane are the 2-dimensional geometries for the current model. Geometry was meshed in ADINA (ADINA R&D, Watertown, MA).

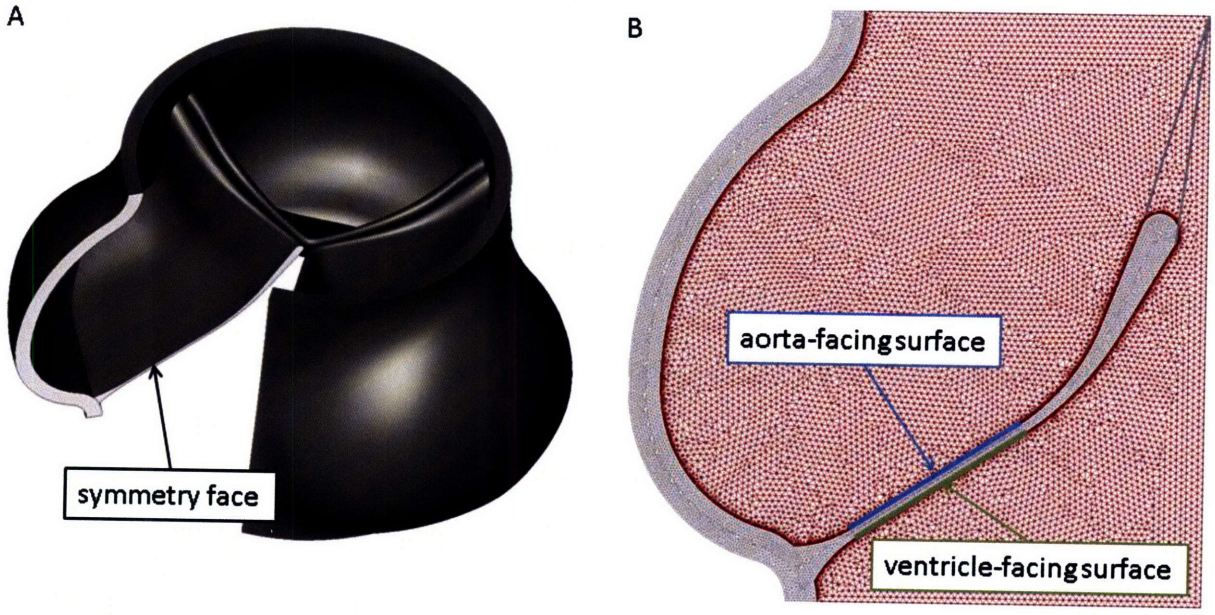


**Figure 5.1.** Aortic valve geometries. A) Full 3-d geometry, created in CAD software based on experimental measurements, showing symmetry plane and B) Meshed 2-dimensional simulation geometry. Aortic-facing and ventricular-facing surfaces are illustrated.

Both the solid and fluid phases were meshed with 3-node triangular elements. To permit large displacements of the solid, the Arbitrary Lagrangian-Eulerian (ALE) method with remeshing of the fluid was used. The solid phase was modeled with an exponential Mooney-Rivlin material

model with constants fit to experimental data[13, 14, 193] ($D_1$=1000 Pa, $D_2$= 30) and blood modeled as a Newtonian fluid ($\mu$=0.003 Pa s). Spring elements with a locking stretch of $\lambda$=1.25 were added to represent the effect of the connection of tissue between the center of the leaflet and the commissures. Simulation geometry, including the solid phase, fluid phase, and added spring elements, is illustrated in Figure 5.1.B. The simulation was run in ADINA, subject to dynamic pressure boundary conditions[193]. Shear profiles applied to the aorta-facing and ventricle-facing surfaces were recorded versus time for one cardiac cycle and averaged over the locations shown in Figure 5.1.B.

*Shear Stress Application*

The two computed shear waveforms were applied to cultured endothelial cells using a cone-and-plate dynamic flow system (DFS), as previously described[45]. Briefly, the DFS rotates a modified cone over a plate seeded with a confluent monolayer of endothelial cells. The cone is driven by a computer-controlled stepper motor (Zeta6104, Axis New England). The design parameters (e.g., cone angle, plate diameter, and medium viscosity) had been evaluated to ensure that the flow is laminar, and that the shear stress is directly proportional to the angular velocity of the cone. Precise control of the cone rotation therefore allows the device to simulate various shear stress waveforms. For each set of experiments, two identical flow devices were used simultaneously. One of them was programmed to simulate the aorta-facing waveform, whereas the other was used for the ventricle-facing waveform (Figure 5.2).

*Human Endothelial Cell Culture*

Human umbilical vein endothelial cells (HUVEC) were isolated and maintained as previously described[45]. Briefly, HUVEC (passage 1) were plated on 0.1% gelatin (Difco)-coated polystyrene circular plates (Plaskolite) at a density of 60,000 cells/cm$^2$ and maintained at 37 C and 5% $CO_2$ in Medium-199 (BioWhittaker) supplemented with 50 μg/ml endothelial cell growth supplement (Collaborative Research) 100 μg/ml heparin (Sigma), 100 units/ml penicillin plus 100 μg/ml streptomycin (BioWhittaker), 2 mM L-Glutamine (Gibco), and 20% FBS (BioWhittaker). After 24 hours, the plate was assembled in the DFS and the HUVEC monolayers were exposed to the aortic-facing and ventricular-facing waveforms using the medium described above with an additional 2% wt/v dextran (Invitrogen) in order to achieve a fluid viscosity of 2.15 cP. The waveforms were applied for 24 hours, over which interval the medium was exchanged at a rate of 0.05 ml/minute. The 24-hour time point was selected for comparison between waveforms to allow transient changes in transcription that primarily reflect the step-like transition from the static condition to a fluid dynamic culture condition to subside, which has previously been used as a steady-state approximation for characterizing flow-dependent endothelial phenotypes[74].

*RNA Isolation and Gene Expression Measurement*

Total RNA was isolated using Lysis Buffer (Applied Biosystems) and purified using the Prism Nucleic Acid Prep-Station (Applied Biosystems) according to the manufacturer's instructions.

RNA quantity was measured by spectrophotometic analysis at 260 nm and quality was verified by Agilent's 2100 Bioanalyzer with RNA 6000 Nano LabChip Kit. Purified, DNase-treated RNA (0.5 μg) was reverse-transcribed using a MultiScribe-based 25 μl reaction (Applied Biosystems). The cDNA was diluted in 50 μl DNAse-free water and subjected to a 20 μl real-time TaqMan quantitative PCR (Applied Biosystems 7900). Expression of Kruppel-like Factor 2 (KLF2, TaqMan probe Hs00360439_g1), Nephroblastoma Overexpressed (NOV, TaqMan probe Hs00159631_m1), Monocyte Chemoattractant Protein 1 (MCP-1/CCL2, TaqMan probe Hs00234140_m1), and VE-Cadherin (CDH5, TaqMan probe Hs00174344_m1) were reported relative to GAPDH (TaqMan probe Hs99999905_m1) and normalized to aorta-facing expression levels. The data reported represents the mean of three independent experiments with the error bars representing standard error. Differences were considered statistically significant for $P < 0.01$, as determined by one-way ANOVA (Primer of Statistics).

*In Situ Hybridization (ISH)*

14.5 day mouse embryos were fixed in 4% paraformaldehyde and embedded in paraffin. 10 μm sections were then taken and ISH carried out using digoxigenin (DIG)-labeled mouse PECAM and KLF2 riboprobes. A PCR amplified fragment of mouse PECAM cDNA (Primer F: 5'-CCAACAGAGCCAGCAGTATGAGGACCAG-3' and Primer R: 5'-CACCCCCCGAAACACAAGGAAGATAGG-3') as well as a PCR amplified fragment of mouse KLF2 cDNA (Primer F: 5'-TACCGAAAGCACACAGGTCA-3' and Primer R: 5'-CCTCCAAAGATCCAAAACTTTA-3') were used as templates for synthesis of the riboprobes. In situ hybridizations were carried out as described by Brent *et al.* 2003[22].

## Results

Numerical simulations of the biomechanical forces acting on the aortic valve were run to convergence for one full cardiac cycle, yielding deformed geometries and fluid velocity profiles

(

A)

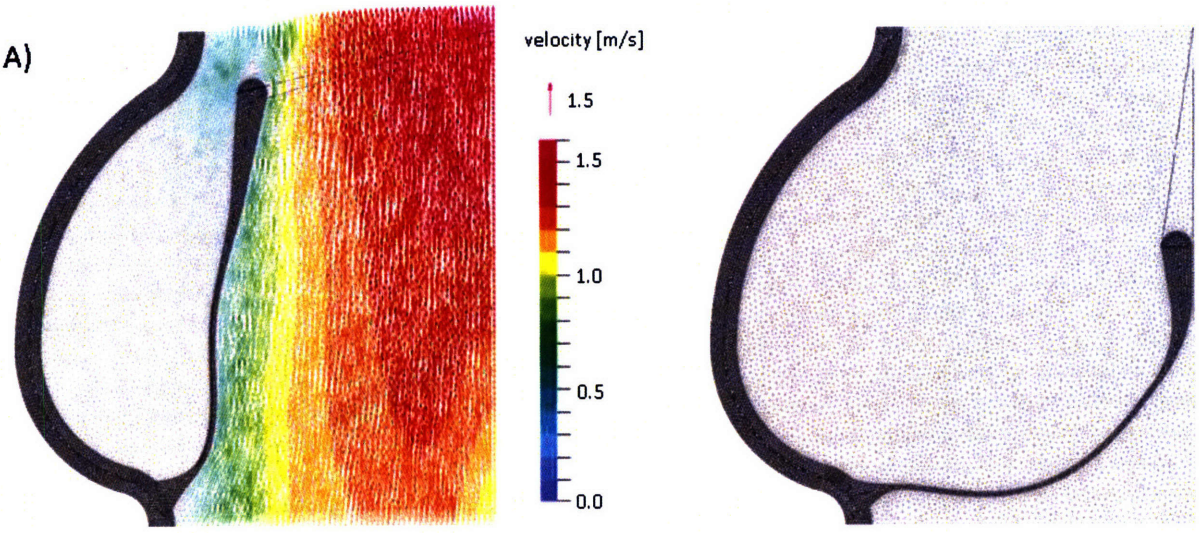


B)

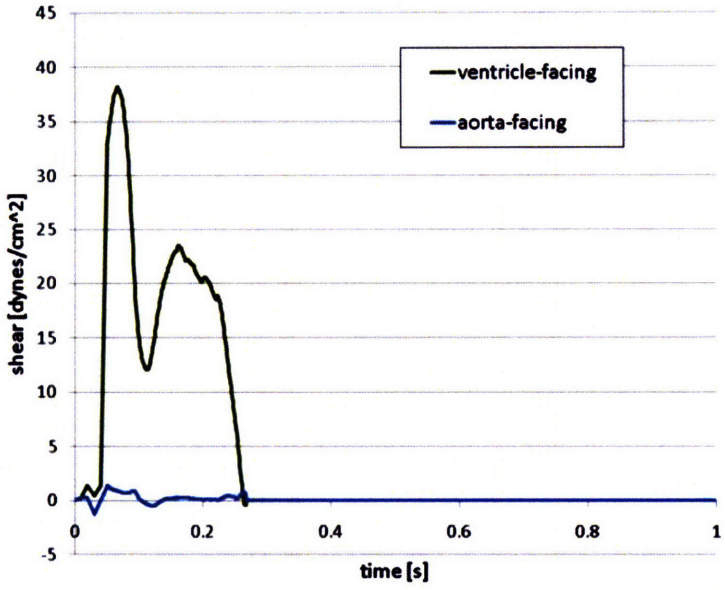


Figure 5.2.A). Bulk velocity profiles match those of our previous models and experimental data[179, 193], and finely resolved velocities at the fluid boundaries were used to extract time-varying shear waveforms for each face of the valve (Figure 5.2.B).

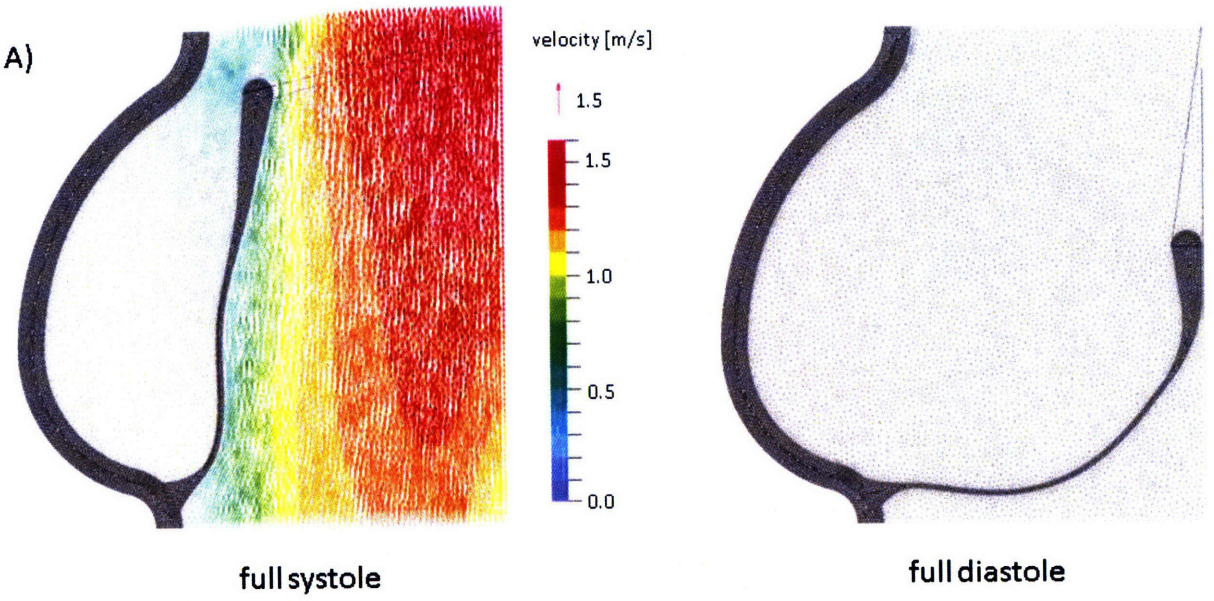


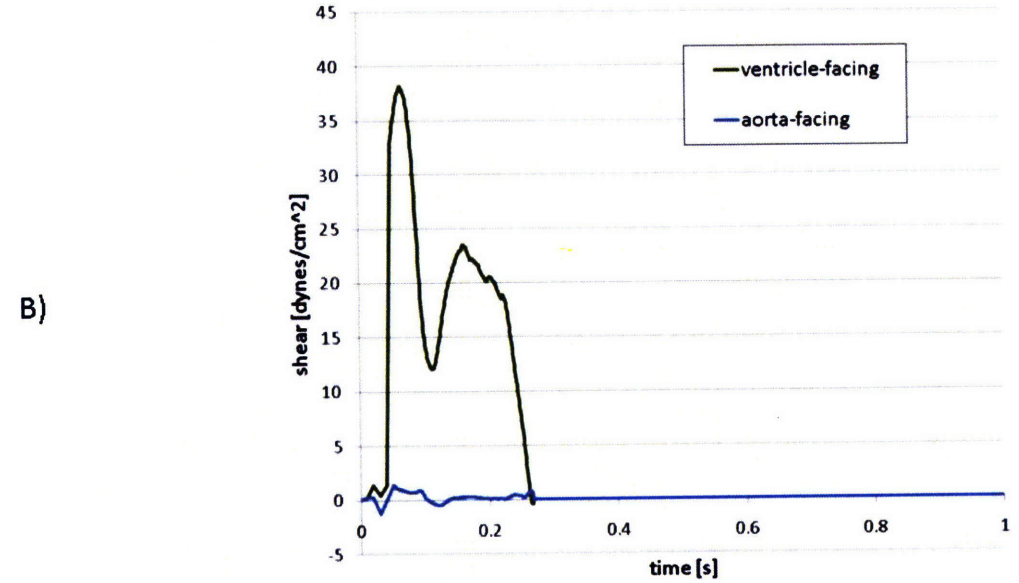


**Figure 5.2.** Results of numerical simulation. A) Deformed geometries and fluid velocity profiles in systole and diastole and B) shears recorded for typical locations on aortic-facing and ventricular-facing surfaces.

The ventricle-facing waveform reached higher magnitudes (40 dynes/cm$^2$ maximum, an average of 4.7 dynes/cm$^2$ over the cardiac cycle), and does not exhibit flow-reversal, while the aortic-facing waveform contains significantly lower magnitudes (3 dynes/cm$^2$ maximum, an average of

0.07 dynes/cm$^2$ over the cardiac cycle) with flow-reversal. The computed hemodynamic waveforms, however, are notably different from others that have been used to investigate the effect of shear forces on endothelial phenotype[45]. In the systemic vasculature, arterial shear forces have a time-varying component, but typically remain non-zero throughout the cardiac cycle. In contrast, the aortic valve experiences a spike in shear during systole when the valve is open and blood is being ejected from the left ventricle and zero shear during diastole when the valve is closed, as reflected in the simulated valve waveforms (see Figure 5.2).

Application of the simulated aortic valve waveforms to cultured HUVEC, a human endothelial cell that has been previously shown to display significant plasticity when exposed to shear stress in culture for 24 hours[34, 45, 74, 120] resulted in the differential expression of endothelial genes that regulate vascular homeostasis and may be important for the initiation and progression of CAS. In particular, exposure of HUVEC to the ventricle-facing valve waveform resulted in increased expression of the vasoprotective transcription factor KLF2 and the matricellular protein NOV, as well as decreased expression of pro-inflammatory molecule MCP-1. There was no change in the pan-endothelial marker VE-Cadherin in cells exposed to the ventricle-facing valve waveform compared to the aorta-facing waveform (see Figure 5.3.A). Moreover, in order to verify KLF2 expression *in vivo*, *in situ* hybridization was performed on mouse embryos at a developmental stage when circulation is fully established (E14.5). In these embryos, we did observe a marked *in vivo* side-dependence expression of KLF2 with higher levels in the ventricle-facing endothelium (see Figure 5.3.B), the side of the developing valve exposed to high flow. It is not known, however, what the specific characteristics of the waveforms generated by flow in these regions of the mouse valves are and how they compared with the human ones simulated in this study.

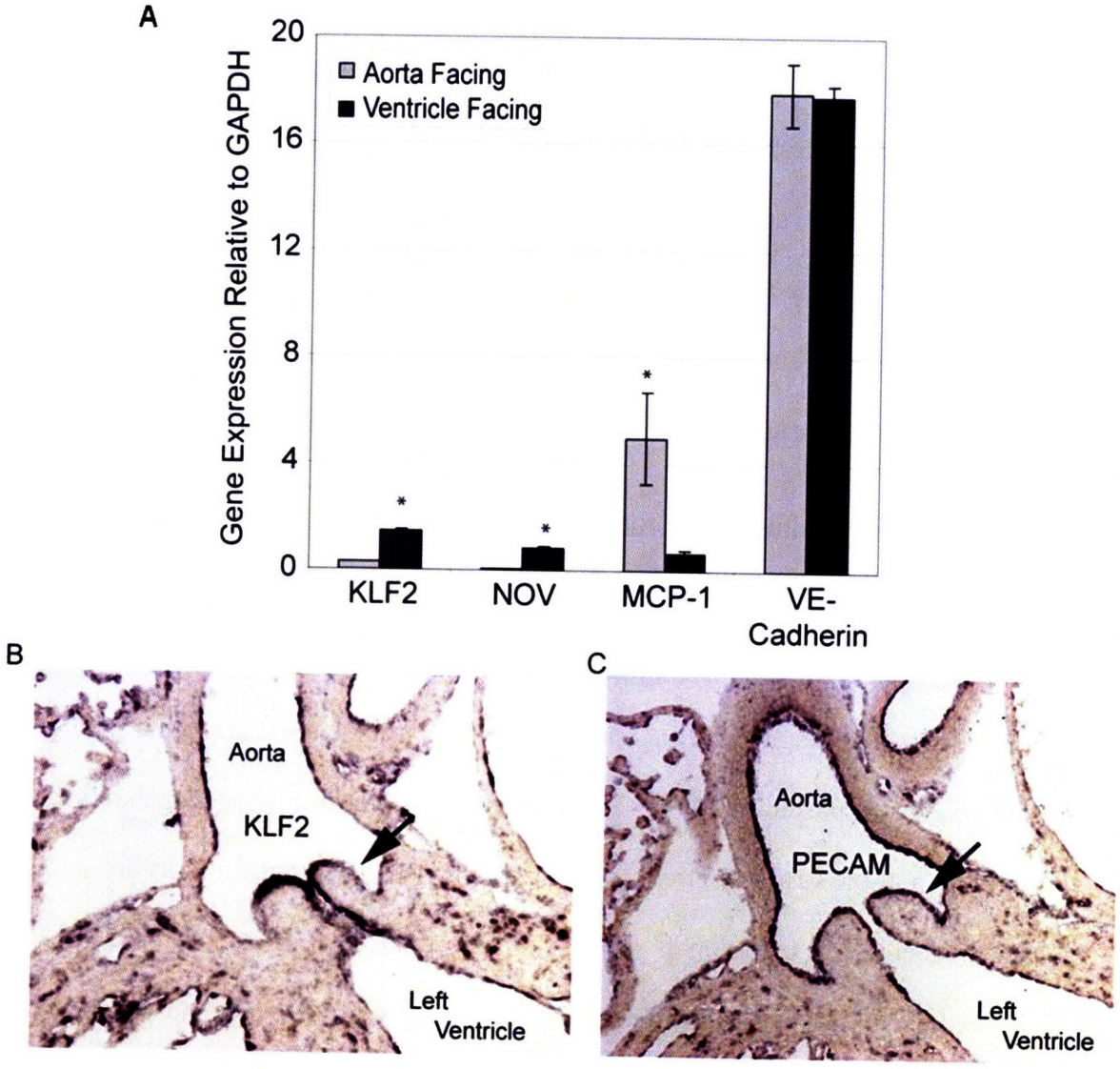


**Figure 5.3.** A) Ventricle-facing aortic valve waveforms evoke an anti-inflammatory endothelial phenotype, as assessed by KLF2, NOV, and MCP-1 gene expression. VE-Cadherin expression, a pan-endothelial marker, showed no difference in expression between the two flow patterns. Data is the average of 3 independent experiments with the error bars representing +/- the standard error. * $P < 0.01$, as determined by one-way ANOVA. KLF2 = Kruppel-like Factor 2; NOV = Nephroblastoma Overexpressed; MCP-1 = Monocyte Chemoattractant Protein 1. *In Situ* hybridization validating the side-dependent KLF2 expression B) E14.5 mouse embryo aortic valves and C) PECAM control staining of the endothelium. Arrow heads indicate the aorta facing surface and lack of KLF2 expression.

## Discussion

CAS represents an important pathological state of cardiac valves in which individual valvular interstitial cells develop calcific deposits, which eventually coalesce, leading to macroscopic calcified nodules, some lesions evolve in the context of an inflammatory focus that resembles the lesions of atherosclerosis. However, the cellular and molecular mechanisms leading to this pathogenesis remain unknown. In particular, the effect the hemodynamic environment has on valvular cells, as well as the valve structure and function, has gained recent attention[167]. In this chapter, we developed a finite element fluid-structure simulation of the aortic valve motion, with high resolution at the fluid boundary, in order to generate physiologically-relevant hemodynamic waveforms acting along the aorta and ventricle-facing valve endothelium. The simulated waveforms (Figure 5.2.B) were applied to cultured human endothelial cells and we documented that the cells exposed to the ventricle-facing waveform display an anti-inflammatory phenotype, as determined by the increased expression of KLF2 and NOV, as well as the suppression of MCP-1, compared to cells exposed to the waveform from the aortic-facing side of the leaflet. It is important to note that endothelial cells derived from the umbilical vein do not represent the ideal cell type to use in the study of endothelial responses to valvular hemodynamic forces. Nevertheless, endothelial cells derived from human cardiac valves are not routinely isolated and grown; however, HUVEC represent a cell with proven phenotypic plasticity and in the context of specific hemodynamic environments may recapitulate several critical aspects of the endothelial cells lining cardiac valves. Furthermore, we have confirmed here the side-specific expression of KLF2 in the mouse aortic valve endothelium using *in situ* hybridization, a result that has also been recently reported by others[111].

Previous studies have shown that endothelial KLF2 mutes the expression of genes associated with vascular inflammation, thrombosis, and calcification in the context of pro-inflammatory stimuli. These two pathophysiological processes are linked to atherogenesis, and may also be relevant to the pathogenesis of CAS[140]. One of the factors suppressed by KLF2 is bone morphogenic protein 4 (BMP4), a gene shown by others to display valve leaflet side-dependent expression[24, 25, 167]. Endothelial KLF2 is highly regulated by hemodynamic forces present in large arteries[50, 51, 140], but in addition Statins, a widely prescribed cholesterol-lowering class of drugs, have also been shown to increase the expression of this transcription factor in the vascular endothelium[140], and this expression is necessary for the Statin-mediated expression of several vasoprotective genes. Importantly, recent clinical data have suggested that Statins may exert a protective effect against the progression of aortic valve calcification[128, 129]. Taken together, these data suggest that KLF2 expression may be a clinically relevant for the valvular endothelial cell phenotype and that sustained expression of KLF2, as is seen on the ventricle-facing side of the valve leaflet, may protect against CAS initiation and progression.

This work constitutes additional evidence supporting the hypothesis that hemodynamic forces may act as important determinants in the development of CAS. Thus, it is possible that the difference in hemodynamic waveforms acting on the leaflets of valves are critical for the establishment and maintenance of different endothelial phenotypes between the two sides of the leaflet, with the ventricular-facing surface displaying an anti-inflammatory phenotype. This difference in phenotype may subsequently drive the side-specific nature of lesion formation in CAS. Recognizing these specific molecular determinants, in combination with improved abilities

to model the valve mechanics, may ultimately enable further understanding of the disease and design of therapies and prevention for CAS.

# Chapter 6. Conclusion

## Thesis Accomplishments

This thesis makes two main contributions to the field of heart valve research. First, it presents a multiscale model of human aortic heart valve mechanical behavior. This model allows, for the first time, prediction of mechanical behavior at the cell, tissue, and organ length scale. Since biological processes in the valve span multiple length scales in both health and disease, the model is useful to investigate many facets of valvular function. The second major contribution of this thesis is one such investigation. The multiscale model was employed in a three-part investigation into the mechanisms of the disease calcific aortic stenosis. Each part of this study provides useful insight into CAS.

Chapter 2 described the formulation of a three-dimensional, dynamic, multiscale model of aortic valve mechanical behavior. This model is depended on a number of enabling contributions. A system of reference configurations was introduced to allow communication between the various length scales. Within that framework, models of the cell and tissue mechanics were created. Both models include accurate and rigorous constitutive material models, and are fully three-dimensional. A computationally efficient discrete-fiber material model was introduced for use in the organ-scale model. The model described in Chapter 2 allows, for the first time, theoretical modeling of the mechanical function in the aortic heart valve across the cell, tissue, and organ length scales. Since biological processes in health and disease span these scales, our model has

wide utility in further investigations of valve biology. The rest of this thesis describes one such investigation.

Chapters 3, 4, and 5 each took a separate approach at investigating mechanisms of CAS. In Chapter 3, the multiscale model of the aortic valve was extended to model aging in the valve. This model linked the mechanical effects of aging at the tissue scale, both normal and due to CAS, to changes in organ scale valve function over an individual's lifetime. As such, this model is useful in further investigations of processes that involve valve aging. These include further study of CAS and other degenerative diseases, development of clinical indices for valve function, and evaluation of treatments for valve disease.

In Chapter 4, we performed a multiscale analysis of the solid deformations related to CAS in the tricuspid and bicuspid valve. These deformations are translated from the organ scale, through the tissue scale, to the cell scale. We showed that, while deformations were considerably different between the two valves at the organ level, the differences were slight at the cell level. Since the deformations important in mechanotransduction are those observed on the cell scale, this work contributes evidence that the difference in likelihood of calcification between the tricuspid and bicuspid valves is not to due to the difference in solid deformations.

Chapter 5 describes an experimental and theoretical inquiry into the role of fluid shear in CAS. We first developed fluid-structure organ scale simulation of valve motion with high resolution in the fluid. This model makes the significant contribution of accurately predicting the transient shear waveforms in the valve, where previously there was a wide range of experimental and theoretical error. Experimental evidence showed that the predicted shear waveforms evoked specific EC phenotypes that correlated well with spatial arrangement of phenotypes and

calcification in natural valves. This work contributes significant evidence that fluid shear has an important, mediating role in the disease CAS.

## Future Directions and Applications

One future direction for the work presented in this thesis is to continue developing and refining the theoretical models. Our model spanning the cell, tissue, and organ scales can be extended downwards to the molecular scale. Such a model would be useful in investigating the molecular signaling cascade related to solid deformations in the valve. Alternatively, our model of the valve could be extended to larger scales, incorporating the valve function into a model of the heart and cardiovascular system. That model would have application in examining the effect of valvular disease on overall cardiovascular health.

The directions that hold promise for making the most significant contributions involve coupling the theoretical models presented in this thesis with experimental work. There are two major directions where combined theoretical and experimental work will be useful. First, the theoretical model enables many investigations into biological processes in the valve, either in health or disease. Chapter 5 is the first example of this sort of effort. We have provided some evidence for theories about CAS, but the complete mechanism of this disease and others are far from clear. The second application of theoretical valve models is in improving clinical care. Theoretical models provide the previously unavailable ability to describe the multiscale function of the valve, which will allow better understanding of current surgeries, pharmaceutical treatments, and

clinical indices for disease. The predictive power of these models will enable development of improved methods of clinical care of patients with valvular disease.

# References


1. Aikawa K, Otto CM, 2001, "Timing of surgery in aortic stenosis," Progress in Cardiovascular Diseases, 43 (6), 477-93.

2. Alkadhi H, Bettex D, Wildermuth S, Baumert B, Plass A, et al, 2005, "Dynamic cine imaging of the mitral valve with 16-mdct: A feasibility study," American Journal of Roentgenology, 185 (3), 636-46.

3. Almeida ES, Spilker RL, 1998, "Finite element formulations for hyperelastic transversely isotropic biphasic soft tissues," Computer Methods in Applied Mechanics and Engineering, 151 (3-4), 513-38.

4. Antonini-Canterin F, Erlicher A, Cervesato E, Piazza R, Faggiano P, et al, 2002, "The rate of hemodynamic progression is strongly predictive of clinical outcome mostly in mild and moderate aortic stenosis," Journal of the American College of Cardiology, 39 (5), 419A-20A.

5. Antonini-Canterin F, Faggiano P, Zanuttini D, Ribichini F, 1999, "Is aortic valve resistance more clinically meaningful than valve area in aortic stenosis?" Heart, 82 (1), 9-10.

6. Basar Y, Kintzel O, 2003, "Finite rotations and large strains in finite element shell analysis," Cmes-Computer Modeling in Engineering & Sciences, 4 (2), 217-30.

7. Bathe KJ. 1996. *Finite element procedures, 2nd edition.* Upper Saddle River, NJ: Prentice Hall

8. Bauer M, Siniawski H, Pasic M, Schaumann B, Hetzer R, 2006, "Different hemodynamic stress of the ascending aorta wall in patients with bicuspid and tricuspid aortic valve," Journal of Cardiac Surgery, 21 (3), 218-20.

9. Baumert B, Plass A, Bettex D, Alkadhi H, Desbiolles L, et al, 2005, "Dynamic cine mode imaging of the normal aortic valve using 16-channel multidetector row computed tomography," Investigative Radiology, 40 (10), 637-47.

10. Beck A, Thubrikar MJ, Robicsek F, 2001, "Stress analysis of the aortic valve with and without the sinuses of valsalva," Journal of Heart Valve Disease, 10 (1), 1-11.

11. Bermejo J, Odreman R, Feijoo J, Moreno MM, Gomez-Moreno P, Garcia-Fernandez MA, 2003, "Clinical efficacy of doppler-echocardiographic indices of aortic valve stenosis: A comparative test-based analysis of outcome," Journal of the American College of Cardiology, 41 (1), 142-51.

12. Betsch P, Gruttmann F, Stein E, 1996, "A 4-node finite shell element for the implementation of general hyperelastic 3d-elasticity at finite strains," Computer Methods in Applied Mechanics and Engineering, 130 (1-2), 57-79.

13. Billiar K, Sacks MS, 2000, "Biaxial mechanical properties of the natural and glutaraldehyde treated aortic valve cusp- part i: Experimental results," Journal of Biomechanical Engineering, 122 23-30.

14. Billiar K, Sacks MS, 2000, "Biaxial mechanical properties of the natural and glutaraldehyde treated aortic valve cusp- part ii: A structural constitutive model," Journal of Biomechanical Engineering, 122 327-35.

15. Bischoff JE, Arruda EM, Grosh K, 2002, "Finite element simulations of orthotropic hyperelasticity," Finite elements in analysis and design, 38 (10), 983-98.

16. Black MM, Howard IC, Huang X, Patterson EA, 1991, "A 3-dimensional analysis of a bioprosthetic heart valve," Journal of Biomechanics, 24 (9), 793-&.

17. Blais C, Pibarot P, Dumesnil JG, Garcia D, Chen DM, Durand LG, 2001, "Comparison of valve resistance with effective orifice area regarding flow dependence," American Journal of Cardiology, 88 (1), 45-52.

18. Bluestein D, Rambod E, Gharib M, 2000, "Vortex shedding as a mechanism for free emboli formation in mechanical heart valves," Journal of Biomechanical Engineering-Transactions of the Asme, 122 (2), 125-34.

19. Bluestein D, Yin W, Affeld K, Jesty J, 2004, "Flow-induced platelet activation in mechanical heart valves," Journal of Heart Valve Disease, 13 (3), 501-8.

20. Boehm T, Husmann L, Leschka S, Desbiolles L, Marincek B, Alkadhi H, 2007, "Image quality of the aortic and mitral valve with ct: Relative versus absolute delay reconstruction," Academic Radiology, 14 (5), 613-24.

21. Bonow RO, Carabello BA, Chatterjee K, de Leon AC, Faxon DP, et al, 2006, "Acc/aha 2006 guidelines for the management of patients with valvular heart disease," Circulation, 114 (5), E84-E231.

22. Brent A, Schweitzer R, Tabin C, 2003, "A somitic compartment of tendon progenitors," Cell, 113 (2), 235-48.

23. Brewer RJ, Mentzer RM, Deck JD, Ritter RC, Trefil JS, Nolan SP, 1977, "Invivo study of dimensional changes of aortic-valve leaflets during cardiac cycle," Journal of Thoracic and Cardiovascular Surgery, 74 (4), 645-50.

24. Butcher J, Nerem RM, 2007, "Valvular endothelial cells and the mechanoregulation of valvular pathology," Phil. Trans. R. Soc. B, 362 (1484), 1445-57.

25. Butcher J, Tressel S, Johnson T, Turner D, Sorescu G, et al, 2006, "Transcriptional profiles of valvular and vascular endothelial cells reveal phenotypic differences - influence of shear stress," Arteriosclerosis Thrombosis and Vascular Biology, 26 (1), 69-77.

26. Butcher JT, Nerem RM, 2007, "Valvular endothelial cells and the mechanoregulation of valvular pathology," Philosophical Transactions of the Royal Society B-Biological Sciences, 362 (1484), 1445-57.

27. Carmody C, Burriesci G, Howard I, Patterson E, 2004, "An approach to the simulation of fluid-structure interaction in the aortic valve," Journal of Biomechanics, 39 158-69.

28. Carmody CJ, Burriesci G, Howard IC, Patterson EA, 2006, "An approach to the simulation of fluid-structure interaction in the aortic valve," Journal of Biomechanics, 39 (1), 158-69.

29. Cataloglu A, Clark R, Gould P, 1977, "Stress analysis of aortic valve leaflets with smoothed geometrical data," Journal of Biomechanics, 10 153.

30. Cataloglu A, Gould P, Clark R, 1976, "Refined stress analysis of human aortic heart valves," J. Eng. Mech. Div. Proc. Am. Soc. Civil Eng., 102 (135),

31. Chandran KB, Fatemi R, Schoephoerster R, Wurzel D, Hansen G, et al, 1989, "Invitro comparison of velocity profiles and turbulent shear distal to polyurethane trileaflet and pericardial prosthetic valves," Artificial Organs, 13 (2), 148-54.

32. Chandran PL, Barocas VH, 2007, "Deterministic material-based averaging theory model of collagen gel micromechanics," Journal of Biomechanical Engineering-Transactions of the Asme, 129 (2), 137-47.

33. Chapelle D, Ferent A, Bathe KJ, 2004, "3d-shell elements and their underlying mathematical model," Mathematical Models & Methods in Applied Sciences, 14 (1), 105-42.

34. Chen B, Li Y, Zhao Y, Chen K, Li S, et al, 2001, "DNA microarray analysis of gene expression in endothelial cells in response to 24-h shear stress," Physiol Genomics, 7 (1), 55-63.

35. Cheng R, Lai YG, Chandran KB, 2003, "Two-dimensional fluid-structure interaction simulation of bileaflet mechanical heart valve flow dynamics," Journal of Heart Valve Disease, 12 (6), 772-80.

36. Cheng R, Lai YG, Chandran KB, 2004, "Three-dimensional fluid-structure interaction simulation of bileaflet mechanical heart valve flow dynamics," Annals of Biomedical Engineering, 32 (11), 1471-83.

37. Chester AH, Taylor PM, 2007, "Molecular and functional characteristics of heart-valve interstitial cells," Philosophical Transactions of the Royal Society B-Biological Sciences, 362 (1484), 1437-43.

38. Chong M, Missirlis Y, 1978, "Aortic valve mechanics part ii: A stress analysis of the porcine aortic valve leaflets in diastole," Biomat. Med. Dev. Art. Org., 6 (3), 225-44.

39. Christie GW, Barrattboyes BG, 1995, "Age-dependent changes in the radial stretch of human aortic-valve leaflets determined by biaxial testing," Annals of Thoracic Surgery, 60 (2), S156-S9.

40. Clark R, 1973, "Stress-strain characteristics of fresh and frozen human aortic and mitral leaflets and chordae tendinae: Implications for clinical use," J Thorac Cardiovasc Surg, 66 202.

41. Clark RE, Karara SM, Catalogl.A, Gould PL, 1974, "Determination of diastolic stresses in human aortic-valve through close range stereophotogrammetry," Circulation, 50 (4), 165-.

42. Cowell SJ, Newby DE, Boon NA, Elder AT, 2004, "Calcific aortic stenosis: Same old story?" Age and Ageing, 33 (6), 538-44.

43. Cripe L, Andelfinger G, Martin LJ, Shooner K, Benson DW, 2004, "Bicuspid aortic valve is heritable," Journal of the American College of Cardiology, 44 (1), 138-43.

44. Dagenais F, Bauset R, Mathieu P, 2005, "Aortic valve-sparing procedure with cusp elongation and free edge reinforcement for bicuspid aortic valve," Annals of Thoracic Surgery, 79 1393-5.

45. Dai G, Kaazempur-Mofrad M, S N, 2004, "Distinct endothelial phenotypes evoked by arterial waveforms derived from atherosclerosis-susceptible and -resistant regions of human vasculature," PNAS, 101 (41), 14871-6.

46. De Hart J, Baaijens FPT, Peters GWM, Schreurs PJG, 2003, "A computational fluid-structure interaction analysis of a fiber-reinforced stentless aortic valve," Journal of Biomechanics, 36 (5), 699-712.

47. De Hart J, Peters GWM, Schreurs PJG, Baaijens FPT, 2003, "A three-dimensional computational analysis of fluid-structure interaction in the aortic valve," Journal of Biomechanics, 36 (1), 103-12.

48. De Hart J, Peters GWM, Schreurs PJG, Baaijens FPT, 2004, "Collagen fibers reduce stresses and stabilize motion of aortic valve leaflets during systole," Journal of Biomechanics, 37 (3), 303-11.

49. Deck JD, Thubrikar MJ, Schneider PJ, Nolan SP, 1988, "Structure, stress, and tissue-repair in aortic-valve leaflets," Cardiovascular Research, 22 (1), 7-16.

50. Dekker R, Boon R, Rondaij M, Kragt A, Volger O, et al, 2006, "Klf2 provokes a gene expression pattern that establishes functional quiescent differentiation of the endothelium," Blood, 107 (11), 4354-63.

51. Dekker R, van Soest S, Fontijn R, Salamanca S, de Groot P, et al, 2002, "Prolonged fluid shear stress induces a distinct set of endothelial cell genes, most specifically lung kruppel-like factor (klf2)," Blood, 100 (5), 1689-98.

52. Della Corte A, Bancone C, Quarto C, Dialetto G, Covino FE, et al, 2007, "Predictors of ascending aortic dilatation with bicuspid aortic valve: A wide spectrum of disease expression," European Journal of Cardio-Thoracic Surgery, 31 (3), 397-404.

53. Dumont K, Vierendeels J, Kaminsky R, Van Nooten G, Verdonck P, Bluestein D, 2007, "Comparison of the hemodynamic and thrombogenic performance of two bileaflet mechanical heart valves using a cfd/fsi model," Journal of Biomechanical Engineering-Transactions of the Asme, 129 (4), 558-65.

54. Dvorkin EN, Pantuso D, Repetto EA, 1995, "A formulation of the mitc4 shell element for finite strain elastoplastic analysis," Computer Methods in Applied Mechanics and Engineering, 125 (1-4), 17-40.

55. Einav S, Stolero D, Avidor J, Elad D, Talbot L, 1989, "Wall shear stress distribution along the cusp of a tri-leaflet prosthetic valve," Journal of Biomedical Engineering, 12 13-8.

56. Einstein DR, Kunzelman KS, Reinhall PG, Nicosia MA, Cochran RP, 2004, "Haemodynamic determinants of the mitral valve closure sound: A finite element study," Medical & Biological Engineering & Computing, 42 (6), 832-46.

57. Einstein DR, Kunzelman KS, Reinhall PG, Nicosia MA, Cochran RP, 2005, "Non-linear fluid-coupled computational model of the mitral valve," Journal of Heart Valve Disease, 14 (3), 376-85.

58. Einstein DR, Kunzelman KS, Reinhall PG, Nicosia MA, Cochran RP, 2005, "The relationship of normal and abnormal microstructural proliferation to the mitral valve closure sound," Journal of Biomechanical Engineering-Transactions of the Asme, 127 (1), 134-47.

59. Ellison JW, Yagubyan M, Majumdar R, Sarkar G, Bolander ME, et al, 2007, "Evidence of genetic locus heterogeneity for familial bicuspid aortic valve," Journal of Surgical Research, 142 (1), 28-31.

60. Faggiano P, Ghizzoni G, Sorgato A, Sabatini T, Simoncelli U, et al, 1992, "Rate of progression of valvular aortic-stenosis in adults," American Journal of Cardiology, 70 (2), 229-33.

61. Fallon AM, Shah N, Marzec UM, Warnock JN, Yoganathan AP, Hanson SR, 2006, "Flow and thrombosis at orifices simulating mechanical heart valve leakage regions," Journal of Biomechanical Engineering-Transactions of the Asme, 128 (1), 30-9.

62. Falsetti H, Kiser K, Francis G, Belmore E, 1972, "Sequential velocity development in the ascending and descending aorta of the dog," Circulation Research, 31 328.

63. Fastenrath S. 1995. *Fasertextur der aorten- and pulmonalkappe des menschen. Kiel: Thesis.*

64. Fedak PWM, de Sa MP, Verma S, Nili N, Kazemian P, et al, 2003, "Vascular matrix remodeling in patients with bicuspid aortic valve malformations: Implications for aortic dilatation," Journal of Thoracic and Cardiovascular Surgery, 126 (3), 797-806.

65. Fedak PWM, Verma S, David TE, Leask RL, Weisel RD, et al, 2002, "Clinical and pathophysiological implications of a bicuspid aortic valve," Circulation, 106 (8), 900-4.

66. Fenner JW, Mackay TG, Martin W, Wheatley DJ, 1995, "Laser profiling- a technique for the study of prosthetic heart valve leaflet motion," Physiological Measurement, 16 (3), 181-93.

67. Feuchtner GM, Dichtl W, Friedrich GJ, Frick M, Alber H, et al, 2006, "Multislice computed tomography for detection of patients with aortic valve stenosis and quantification of severity," Journal of the American College of Cardiology, 47 (7), 1410-7.

68. Feuchtner GM, Dichtl W, Schachner T, Muller S, Mallouhi A, et al, 2006, "Diagnostic performance of mdct for detecting aortic valve regurgitation," American Journal of Roentgenology, 186 (6), 1676-81.

69. Ford LE, Feldman T, Chiu YC, Carroll JD, 1990, "Hemodynamic resistances as a measure of functional impairment in aortic valvular stenosis," Circulation Research, 66 (1), 1-7.

70. Freeman RV, Otto CM, 2005, "Spectrum of calcific aortic valve disease: Pathogenesis, disease progression, and treatment strategies," Circulation, 111 3316-26.

71. Fung Y, 1967, "Elasticity of soft tissues in simple elongation," American Journal of Physiology, 213 1532-44.

72. Fung Y. 1993. *Biomechanics: Mechanical properties of living tissues.* New York: Springer

73. Gao ZB, Pandya S, Hosein N, Sacks MS, Hwang NHC, 2000, "Bioprosthetic heart valve leaflet motion monitored by dual camera stereo photogrammetry," Journal of Biomechanics, 33 (2), 199-207.

74. Garcia-Cardena G, Comander J, Anderson K, Blackman B, MA G, 2001, "Biomechanical activation of vascular endothelium as a determinant of its functional phenotype," PNAS, 98 (8), 4478-85.

75. Garcia D, Pibarot P, Dumesnil JG, Sakr F, Durand LG, 2000, "Assessment of aortic valve stenosis severity - a new index based on the energy loss concept," Circulation, 101 (7), 765-71.

76. Gnyaneshwar R, Kumar RK, Balakrishnan KR, 2002, "Dynamic analysis of the aortic valve using a finite element model," Annals of Thoracic Surgery, (73), 1122-9.

77. Gorlin R, 1987, "Calculations of cardiac-valve stenosis - restoring an old concept for advanced applications," Journal of the American College of Cardiology, 10 (4), 920-2.

78. Gould P, Cataloglu A, Dhatt G, Cattopadhyay A, Clark R, 1973, "Stress analysis of the human aortic valve," Computers & Structures, 3 377.

79. Grande-Allen K, Cochran R, Reinhall P, Kunzelman K, 2001, "Finite-element analysis of aortic valve sparing: Influence of graft shape and stiffness," IEEE Transactions on Biomedical Engineering, 48 (6), 647-59.

80. Grande K, Cochran R, Reinhall P, Kunzelman K, 1999, "Mechanisms of aortic valve incompetence in aging: A finite element model," Journal of Heart Valve Disease, 8 (2), 149-56.

81. Grande KJ, Cochran RP, Reinhall PG, Kunzelman KS, 1998, "Stress variations in the human aortic root and valve: The role of anatomic asymmetry," Annals of Biomedical Engineering, 26 (4), 534-45.

82. Grashow JS, Sacks MS, Liao J, Yoganathan AP, 2006, "Planar biaxial creep and stress relaxation of the mitral valve anterior leaflet," Annals of Biomedical Engineering, 34 (10), 1509-18.

83. Gupta V, Werdenberg J, Mendez J, Grande-Allen K, 2008, "Influence of strain on proteoglycan synthesis by valvular interstitial cells in three-dimensional culture," Acta Biomaterialia, 4 88-96.

84. Hallquist J. 2006. *Ls-dyna theory manual.* Livermore

85. Hamid MS, Sabbah HN, Stein PD, 1985, "Comparison of finite-element stress-analysis of aortic valve leaflet using either membrane elements or solid elements," Computers & Structures, 20 (6), 955-61.

86. Hamid MS, Sabbah HN, Stein PD, 1985, "Large-deformation analysis of aortic-valve leaflets during diastole," Engineering Fracture Mechanics, 22 (5), 773-85.

87. Handke M, Heinrichs G, Beyersdorf F, Olschewski M, Bode C, Geibel A, 2003, "In vivo analysis of aortic valve dynamics by transesophageal 3-dimensional echocardiography with high temporal resolution," Journal of Thoracic and Cardiovascular Surgery, 125 (6), 1412-9.

88. He ZM, Ritchie J, Grashow JS, Sacks MS, Yoganathan AP, 2005, "In vitro dynamic strain behavior of the mitral valve posterior leaflet," Journal of Biomechanical Engineering-Transactions of the Asme, 127 (3), 504-11.

89. Holzapfel GA. 2000. *Nonlinear solid mechanics: A continuum approach for engineering.* New York: Wiley

90. Holzapfel GA, Eberlein R, Wriggers P, Weizsacker HW, 1996, "Large strain analysis of soft biological membranes: Formulation and finite element analysis," Computer Methods in Applied Mechanics and Engineering, 132 (1-2), 45-61.

91. Holzapfel GA, Gasser TC, Ogden RW, 2000, "A new constitutive framework for arterial wall mechanics and a comparative study of material models," Journal of Elasticity, 61 (1-3), 1-48.

92. Howard I, Patterson EA, Yoxall A, 2003, "On the opneing mechanism of the aortic valve: Some observations from simulations," Journal of medical engineering & technology, 27 (6), 259-66.

93. Huang H-YS. 2004. *Micromechanical simulations of heart valve tissues*. University of Pittsburgh

94. Huang HVS, Liao J, Sacks MS, 2007, "In-situ deformation of the aortic valve interstitial cell nucleus under diastolic loading," Journal of Biomechanical Engineering-Transactions of the Asme, 129 (6), 880-9.

95. Humphrey JD, 2003, "Continuum biomechanics of soft biological tissues," Proceedings of the Royal Society of London Series a-Mathematical Physical and Engineering Sciences, 459 (2029), 3-46.

96. Iyengar AKS, Sugimoto H, Smith DB, Sacks MS, 2001, "Dynamic in vitro quantification of bioprosthetic heart valve leaflet motion using structured light projection," Annals of Biomedical Engineering, 29 (11), 963-73.

97. John AS, Dill T, Brandt RR, Rau M, Ricken W, et al, 2003, "Magnetic resonance to assess the aortic valve area in aortic stenosis - how does it compare to current diagnostic standards?" Journal of the American College of Cardiology, 42 (3), 519-26.

98. Katz J, Misra A, Spencer P, Wang Y, Bumrerraj S, et al, 2007, "Multiscale mechanics of hierarchical structure/property relationships in calcified tissues and tissue/material interfaces," Mater Sci Eng A Struct Mater, 27 (3), 450-68.

99. Kim H, Chandran KB, Sacks MS, Lu J, 2007, "An experimentally derived stress resultant shell model for heart valve dynamic simulations," Annals of Biomedical Engineering, 35 (1), 30-44.

100. Kim H, Lu J, Sacks MS, Chandran KB, 2006, "Dynamic simulation pericardial bioprosthetic heart valve function," Journal of Biomechanical Engineering-Transactions of the Asme, 128 (5), 717-24.

101. Kim HG, Lu J, Sacks MS, Chandran KB, 2008, "Dynamic simulation of bioprosthetic heart valves using a stress resultant shell model," Annals of Biomedical Engineering, 36 (2), 262-75.

102. Kim KM, Huang SN, 1971, "Ultrastructural study of calcification of human aortic valve," Lab Invest, 25 (5), 357-66.

103. Kim KM, Valigorsky JM, Mergner WJ, Jones RT, Pendergrass RF, Trump BF, 1976, "Aging changes in the human aortic valve in relation to dystrophic calcification," Hum Pathol, 7 (1), 47-60.

104. Kizer J, Gefter W, deLemos A, 2001, "Electron beam computed tomography for quantification of aortic valvular calcification," Journal of Heart Valve Disease, 2001 (218), 548-55.

105. Klinkel S, Govindjee S, 2002, "Using finite strain 3d-material models in beam and shell elements," Engineering Computations, 19 (7-8), 902-21.

106. Kunzelman KS, Cochran RP, Chuong C, Ring W, Verrier E, Eberhart R, 1993, "Finite element analysis of the mitral valve," Journal of Heart Valve Disease, 3 326-40.

107. Kunzelman KS, Einstein DR, Cochran RP, 2007, "Fluid-structure interaction models of the mitral valve: Function in normal and pathological states," Philosophical Transactions of the Royal Society B-Biological Sciences, 362 (1484), 1393-406.

108. Kuusisto J, Rasanen K, Sarkioja T, Alarakkola E, Kosma V, 2005, "Atherosclerosis-like lesions of the arotic valve are common in adults of all ages: A necropsy study," Heart, 91 576-82.

109. Lacefield JC, Weaver J, Spence JR, Dunmore-Buyze J, Boughner DR, 2004, "Three-dimensional visualization and thickness estimation of aortic valve cusps using high-frequency ultrasound," Physiological Measurement, 25 (1), 27-36.

110. Lansac E, Lim HS, Shomura Y, Lim KH, Rice NT, et al, 2002, "A four-dimensional study of the aortic root dynamics," European Journal of Cardio-Thoracic Surgery, 22 (4), 497-503.

111. Lee J, Yu C, Shin J, Sebzda E, Bertozzi C, et al, 2006, "Klf2 is an essential regulator of vascular heomdynamics in vivo," Developmental Cell, 11 (6), 845-57.

112. Lester SJ, McElhinney DB, Miller JP, Lutz JT, Otto CM, Redberg RF, 2000, "Rate of change in aortic valve area during a cardiac cycle can predict the rate of hemodynamic progression of aortic stenosis," Circulation, 101 (16), 1947-52.

113. Lewin MB, Otto CB, 2005, "The bicuspid aortic valve: Adverse outcomes from infancy to old age," Circulation, 111 832-4.

114. Li J, Luo X, Kuang Z, 2001, "A nonlinear anisotropic model for porcine aortic heart valves," Journal of Biomechanics, 34 (10), 1279-89.

115. Lilly L, ed. 2003. *Pathophysiology of heart valve disease, third edition.* Philadelphia: Lippincott Williams & Wilkins

116. Lim C, Zhou E, Quek S, 2006, "Mechanical models for living cells- a review," Journal of Biomechanics, 39 195-216.

117. Liu AC, Joag VR, Gotlieb AI, 2007, "The emerging role of valve interstitial cell phenotypes in regulating heart valve pathobiology," The American Journal of Pathology, 171 (5), 1407-18.

118. Luo ZP, Bolander ME, An KN, 1997, "A method for determination of stiffness of collagen molecules," Biochemical and Biophysical Research Communications, 232 (1), 251-4.

119. May-Newman K, Yin F, 1998, "A constitutive law for mitral valve tissue," Journal of Biomechanical Engineering, 120 (1), 38-47.

120. McCormick S, Eskin S, McIntire L, Teng C, Lu C, et al, 2001, "DNA microarray reveals changes in gene expression of shear stressed human umbilical vein endothelial cells," PNAS, 98 (16), 8955-60.

121. Mendelson K, Schoen F, 2006, "Heart valve tissue engineering: Concepts, approaches, progress, and challenges," Annals of Biomedical Engineering, 34 (12), 1799-819.

122. Merryman WD, Huang H-YS, Schoen FJ, Sacks MS, 2006, "The effects of cellular contraction on aortic valve leaflet flexural stiffness," Journal of Biomechanics, 39 88-96.

123. Merryman WD, Youn I, Lukoff HD, Krueger PM, Guilak F, et al, 2006, "Correlation between heart valve instertitial cell stiffness and transvalvular pressure: Implications for collagen biosynthesis," Heart and Circulatory Physiology, 290 H224-H31.

124. Migliavacca F, Balossino R, Pennati G, Dubini G, Hsia TY, et al, 2006, "Multiscale modelling in biofluidynamics: Application to reconstructive paediatric cardiac surgery," Journal of Biomechanics, 39 (6), 1010-20.

125. Misfeld M, Sievers HH, 2007, "Heart valve macro- and microstructure," Philosophical Transactions of the Royal Society B-Biological Sciences, 362 (1484), 1421-36.

126. Missirlis Y, Chong M, 1978, "Aortic valve mechanics i. Material properties of natural porcine aortic valves," J Bioengineering, 2 287.

127. Mofrad MK, Kamm R, eds. 2006. *Cytoskeletal mechanics: Models and measurements*. New York: Cambridge University Press

128. Mohler ER, Wang H, Medenilla E, Scott C, 2007, "Effect of statin treatment on aortic valve and coronary artery calcification," Journal of Heart Valve Disease, 16 (4), 378-86.

129. Moura LM, Ramos SF, Zamorano JL, Barros IM, Azevedo LF, et al, 2007, "Rosuvastatin affecting aortic valve endothelium to slow the progression of aortic stenosis," Journal of the American College of Cardiology, 49 (5), 554-61.

130. Nichols W, O'Rourke M. 1998. *Mcdonald's blood flow in arteries, 5th ed.* London: Arnold

131. Nicosia MA, Cochran RP, Einstein DR, Rutland CJ, Kunzelman KS, 2003, "A coupled fluid-structure finite element modle of the aortic valve and root," The Journal of Heart Valve Disease, 12 (781-9),

132. Otto C, Lind B, Kitzman D, Gersh B, Siscovick D, 1999, "Association of aortic-valve sclerosis with cardiovascular mortality and morbidity in the elderly," New England Journal of Medicine, 341 (3), 142-7.

133. Otto CM, 2000, "Timing of aortic valve surgery," Heart, 84 (2), 211-8.

134. Otto CM, 2002, "Calcification of bicuspid aortic valves," Heart, 88 321-2.

135. Otto CM. 2003. *Valvular heart disease, edition 2*. Philadelphia, PA: Saunders

136. Otto CM, 2006, "Valvular aortic stenosis - disease severity and timing of intervention," Journal of the American College of Cardiology, 47 (11), 2141-51.

137. Otto CM, 2007, "Statins for aortic stenosis? Still waiting for answers," Nature Clinical Practice Cardiovascular Medicine, 4 (7), 358-9.

138. Otto CM, Kuusisto J, Reichenbach D, Gown A, Obrien K, 1994, "Characterization of the early lesion of degenerative valvular aortic-stenosis - histological and immunohistochemical studies," Circulation, 90 (2), 844-53.

139. Park S, Klein TE, Pande VS, 2007, "Folding and misfolding of the collagen triple helix: Markov analysis of molecular dynamics simulations," Biophysical Journal, 93 (12), 4108-15.

140. Parmar K, Larman H, Dai G, Zhang Y, Wang E, et al, 2006, "Integration of flow-dependent endothelial phenotypes by kruppel-like factor 2," Journal of Clinical Investigation, 116 (1), 49-58.

141. Piper C, Bergemann R, Schulte HD, Koerfer R, Horstkotte D, 2003, "Can progression of valvar aortic stenosis be predicted accurately?" Annals of Thoracic Surgery, 76 (3), 676-80.

142. Prot V, Skallerud B, Flolzapfel GA, 2007, "Transversely isotropic membrane shells with application to mitral valve mechanics. Constitutive modelling and finite element implementation," International Journal for Numerical Methods in Engineering, 71 (8), 987-1008.

143. Rabkin-Aikawa E, Farber M, Aikawa M, Schoen F, 2004, "Dynamic and reversible changes of interstitial cell phenotype during remodeling of cardiac valves," Journal of Heart Valve Disease, 13 (5), 841-7.

144. Raman SS, Parthasarathi R, Subramanian V, Ramasami T, 2006, "Role of aspartic acid in collagen structure and stability: A molecular dynamics investigation," Journal of Physical Chemistry B, 110 (41), 20678-85.

145. Raman SS, Parthasarathi R, Subramanian V, Ramasami T, 2008, "Role of length-dependent stability of collagen-like peptides," Journal of Physical Chemistry B, 112 (5), 1533-9.

146. Raman SS, Vijayaraj R, Parthasarathi R, Subramanian V, Ramasami T, 2008, "A molecular dynamics analysis of ion pairs formed by lysine in collagen: Implication for collagen function and stability," Journal of Molecular Structure-Theochem, 851 (1-3), 299-312.

147. Robicsek F, 2003, "Editorial: Bicuspid versus tricuspid aortic valves," Journal of Heart Valve Disease, 12 (1), 52-3.

148. Robicsek F, Thubrikar MJ, Cook JW, Fowler B, 2004, "The congenitally bicuspid aortic valve: How does it function? Why does it fail?" Annals of Thoracic Surgery, 77 177-85.

149. Robicsek F, Thubrikar MJ, Cook JW, Reames MK, Fowler BL, Nw, 2004, "Creases and folds: Why does the bicuspid aortic valve fail so early?" Journal of the American College of Cardiology, 43 (5), 436A-A.

150. Rosenhek R, Rader F, Loho N, Gabriel H, Heger M, et al, 2004, "Statins but not ace-inhibitors delay aortic stenosis progression," European Heart Journal, 25 250-.

151. Rousseau EPM, Sauren A, Vanhout MC, Vansteenhoven AA, 1983, "Elastic and viscoelastic material behavior of fresh and glutaraldehyde-treated porcine aortic-valve tissue," Journal of Biomechanics, 16 (5), 339-&.

152. Roy A, Brand N, Yacoub M, 2000, "Molecular characterization of interstitial cells isolated from human heart valves," Journal of Heart Valve Disease, 3 (9), 459-64.

153. Ruter M, Stein E, 2000, "Analysis, finite element computation and error estimation in transversely isotropic nearly incompressible finite elasticity," Computer Methods in Applied Mechanics and Engineering, 190 (5-7), 519-41.

154. Sacks M, Gloeckner D, N V, 2002, "Alterations in the flexural behavior of porcine bioprosthetic heart valves with fatigue," Journal of Heart Valve Disease,

155. Sacks MS, 2001, "The biomechanical effects of fatigue on the porcine bioprosthetic heart valves," Journal of Long Term Effects of Medical Implants, 11 (3-4), 231-47.

156. Sacks MS, 2002, "The biomechanical effects of fatigue on the porcine bioprosthetic heart valves," Journal of Biomedical Materials Research,

157. Sacks MS, Mirnajafi A, Sun W, Schmidt P, 2006, "Bioprosthetic heart valve heterograft biomaterials: Structure, mechanical behavior and computational simulation," Expert Review of Medical Devices, 3 (6), 817-34.

158. Sacks MS, Smith DB, Hiester ED, 1998, "The aortic valve microstructure: Effects of transvalvular pressure," Journal of Biomedical Materials Research, 41 (1), 131-41.

159. Sacks MS, Sun W, 2003, "Multiaxial mechanical behavior of biological materials," Annual Review of Biomedical Engineering, 5 251-84.

160. Sacks MS, Yoganathan AP, 2007, "Heart valve function: A biomechanical perspective," Phil. Trans. R. Soc. B, 362 1369-91.

161. Sahasakul Y, Edwards WD, Naessens JM, Tajik AJ, 1988, "Age-related changes in aortic and mitral valve thickness: Implications for two-dimensional echocardiography based on an autopsy study of 200 normal human hearts," American Journal of Cardiology, 62 (7), 424-30.

162. Salsas-Escat R, Stultz C, 2008, "The molecular mechanics of collagen degradation: Implications for human disease," Experimental Mechanics, Published online ahead of print

163. Sauren AAHJ, Hout Mv, Steenhoven Av, Veldpaus F, Janssen J, 1983, "The mechacnical properties of porcine aortic valve tissues," J Biomechanics, 16 327.

164. Schenke-Layland K, Reimann I, Opitz F, Konig K, 2004, "Comparative study of cellular and extracellular matrix composition of native and tissue engineered heart valves," Matrix biology, 23 113-25.

165. Schoen FJ, Levy RJ, 1999, "Tissue heart valves: Current challenges and future research perspectives," Journal of Biomedical Materials Research, 47 439-65.

166. Schwarz F, Baumann P, Manthey J, Hoffmann M, SChuler G, et al, 1982, "The effect of aortic valve replacement on survival," Circulation, 66 (1105-1110),

167. Simmons C, Grant G, Manduchi E, Davies P, 2005, "Spatial heterogeneity of endothelial phenotypes correlates with side-specific vulnerability to calcification in normal porcine aortic valves," Circulation Research, 96 (7), 792-9.

168. Sotomayor M, Schulten K, 2007, "Single-molecule experiments in vitro and in silico," Science, 316 (5828), 1144-8.

169. Starr A, Edwards M, 1961, "Mitral replacement: Clinical experience with a ball-valve prosthesis," Annals of Surgery, 154 (4), 726-40.

170. Stella JA, Sacks MS, 2007, "On the biaxial mechanical properties of the layers of the aortic valve leaflet," Journal of Biomechanical Engineering-Transactions of the Asme, 129 (5), 757-66.

171. Stylianopoulos T, Barocas VH, 2007, "Multiscale, structure-based modeling for the elastic mechanical behavior of arterial walls," Journal of Biomechanical Engineering-Transactions of the Asme, 129 (4), 611-8.

172. Sun W, Abad A, Sacks MS, 2005, "Simulated bioprosthetic heart valve deformation under quasi-static loading," Journal of Biomechanical Engineering-Transactions of the Asme, 127 (6), 905-14.

173. Sun W, Sacks MS, 2005, "Finite element implementation of a generalized fung-elastic constitutive model for planar soft tissues," Biomechanics and Modeling in Mechanobiology, 4 (2-3), 190-9.

174. Sung H-W, Chang Y, Chui C-T, Chen C-N, Liang H-C, 1999, "Mechanical properties of a porcine aortic valve fixed with a naturally occurring croslinking agent," Biomaterials, 20 1759-72.

175. Sussman T, Bathe KJ, 1987, "A finite-element formulation for nonlinear incompressible elastic and inelastic analysis," Computers & Structures, 26 (1-2), 357-409.

176. Sze K, Zheng S, Lo S, 2004, "A stabilized eighteen-node solid element for hyperelastic analysis of shells," Finite elements in analysis and design, 40 (3), 319-40.

177. Taylor P, Batten P, Brand N, Thomas P, Yacoub M, 2003, "The cardiac valve interstitial cell," The International Journal of Biochemistry & Cell Biology, 35 113-8.

178. Taylor PM, 2007, "Biological matrices and bionanotechnology," Philosophical Transactions of the Royal Society B-Biological Sciences, 362 (1484), 1313-20.

179. Thubrikar M. 1990. *The aortic valve*. Boca Raton, FL: CRC Press

180. Thubrikar M, Piepgrass WC, Deck JD, Nolan SP, 1980, "Stresses of natural versus prosthetic aortic-valve leaflets invivo," Annals of Thoracic Surgery, 30 (3), 230-9.

181. Thubrikar MJ, Aouad J, Nolan SP, 1986, "Patterns of calcific deposits in operatively excised stenotic or purely regurgitant aortic valves and their relation to mechanical stress," American Journal of Cardiology, 58 304-8.

182. Thubrikar MJ, Nolan SP, Aouad J, Deck JD, 1986, "Stress sharing between the sinus and leaflets of canine aortic valve," Annals of Thoracic Surgery, 42 (4), 434-40.

183. VanAuker MD, 2006, "Age-related changes in hemodynamics affecting valve performance," American Journal of Geriatric Cardiology, 15 (5), 277-83.

184. Vesely I, 1996, "Reconstruction of loads in the fibrosa and ventricularis of porcine aortic valves," ASAIO Journal, 42 M739-M46.

185. Vesely I, Lozon A, 1993, "Natural preload of aortic valve leaflet components during glutaraldehyde fixation: Effects on tissue mechanics," Journal of Biomechanics, 26 (2), 121-31.

186. Vesely I, Noseworthy R, 1991, "Micromechanics of the fibrosa and the ventricularis in aortic valve leaflets," Journal of Biomechanics, 25 (1), 101-13.

187. Ward C, 2000, "Clinical significance of the bicuspid aortic valve," Heart, 83 (1), 81-5.

188. Weinberg E, Kaazempur Mofrad MR, 2005, "On the constitutive models for heart valve leaflet mechanics," Cardiovascular Engineering, 5 (1), 37-43.

189. Weinberg E, Mack P, Jr. GV, Schoen F, Garcia-Cardena G, Mofrad MK, 2008, "Hemodynamic environments from opposing sides of human aortic valve leaflets evoke distinct endothelial phenotypes," Submitted 4/2008.

190. Weinberg EJ, Kaazempur-Mofrad M, 2008, "A multiscale computational comparison of the bicuspid and tricuspid aortic valves in relation to valcific aortic stenosis,"Journal of Biomechanics, accepted 5/2008.

191. Weinberg EJ, Kaazempur-Mofrad MR, 2005, "A large-strain finite element formulation for biological tissues with application to mitral valve leaflet tissue mechanics," Journal of Biomechanics, 39 (8), 1557-61.

192. Weinberg EJ, Kaazempur-Mofrad MR, 2006, "A finite shell element for heart mitral valve leaflet mechanics, with large deformations and 3d constitutive model," Journal of Biomechanics, 40 (3), 705-11.

193. Weinberg EJ, Kaazempur Mofrad MR, 2007, "Transient, three-dimensional, multiscale simulations of the human aortic valve.," Cardiovascular Engineering, 7 (4), 140-55.

194. Weston M, LaBorde D, Yoganathan AP, 1999, "Estimation of shear stress on the surface of an aortic valve leaflet," Annals of Biomedical Engineering, 27 572-9.

195. Yacoub M, Cohn L, 2004, "Novel approaches to cardiac valve repair. From structure to function: Part i," Circulation, 109 942-50.

196. Yacoub M, Cohn L, 2004, "Novel approaches to cardiac valve repair. From structure to function: Part ii," Circulation, 109 1064-72.

197. Yacoub N, Takkenberg J, 2005, "Will heart valve tissue engineering change the world?" Nature Clinical Practice Cardiovascular Medicine, 2 (2), 60-1.

198. Yang G, Merrifield R, Masood S, Kilner P, 2007, "Flow and myocardial interaction: An imaging perspective," Phil. Trans. R. Soc. B, 362 1329-41.

199. Yin W, Alemu Y, Affeld K, Jesty J, Bluestein D, 2004, "Flow-induced platelet activation in bileaflet and monoleaflet mechanical heart valves," Annals of Biomedical Engineering, 32 (8), 1058-66.